

2006

Static and ultrafast MOKE studies of exchange -biased cobalt systems

Keoki A. Seu

College of William & Mary - Arts & Sciences

Follow this and additional works at: <https://scholarworks.wm.edu/etd>



Part of the [Condensed Matter Physics Commons](#), and the [Optics Commons](#)

Recommended Citation

Seu, Keoki A., "Static and ultrafast MOKE studies of exchange -biased cobalt systems" (2006).

Dissertations, Theses, and Masters Projects. Paper 1539623503.

<https://dx.doi.org/doi:10.21220/s2-5nn0-3402>

This Dissertation is brought to you for free and open access by the Theses, Dissertations, & Master Projects at W&M ScholarWorks. It has been accepted for inclusion in Dissertations, Theses, and Masters Projects by an authorized administrator of W&M ScholarWorks. For more information, please contact scholarworks@wm.edu.

STATIC AND ULTRAFAST MOKE STUDIES OF EXCHANGE-BIASED
COBALT SYSTEMS

A Dissertation

Presented to

The Faculty of the Department of Physics
The College of William and Mary in Virginia

In Partial Fulfillment

Of the Requirements for the Degree of

Doctor of Philosophy

by

Keoki A. Seu

2006

APPROVAL SHEET

This dissertation is submitted in partial fulfillment of
the requirements for the degree of

Doctor of Philosophy

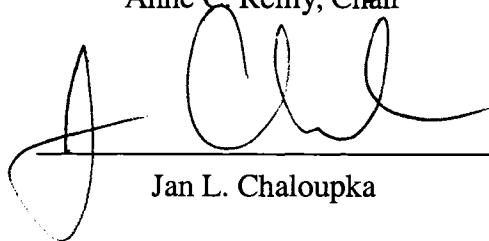


Keoki A. Seu

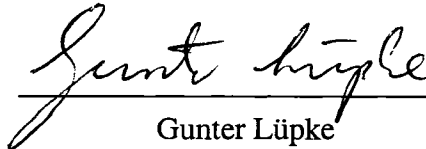
Approved by the Committee, September 2006



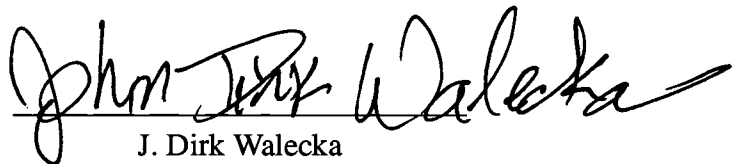
Anne C. Reilly, Chair



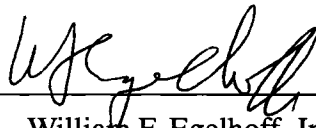
Jan L. Chaloupka



Gunter Lüpke



J. Dirk Walecka



William F. Egelhoff, Jr.

National Institute for Standards and Technology

This work is dedicated to my family.

TABLE OF CONTENTS

	Page
Acknowledgments	viii
List of Tables	ix
List of Figures	x
Abstract	xiii
CHAPTER	
1 Introduction	2
1.1 Review of Current Literature	3
1.2 Dissertation Outline	5
2 Magnetism and Exchange Bias	8
2.1 Ferromagnetism	8
2.1.1 Demagnetization Fields	10
2.1.2 Domains and Domain Walls	13
2.1.3 Magnetic Anisotropy	14
2.2 Antiferromagnetism	15
2.2.1 Grains, Antiferromagnetic Domains, Néel and Blocking Tem- perature	16
2.3 Exchange Bias	17
2.3.1 Compensated and Uncompensated Spins	18
2.3.2 Effects of Interfacial Roughness	19

2.3.3	Effects of Polycrystalline Structures	20
2.4	Models of Exchange Bias	21
2.4.1	Meiklejohn: Coherent Rotation and Rotational Hysteresis	21
2.4.2	Malozemoff: Random Field Model via Defects	22
2.4.3	Spin Flop Models	24
2.4.4	Stiles and McMichael and the Effect of AF Grains	25
2.5	Materials Used in Exchange Biasing	27
2.5.1	Antiferromagnets: Iridium Manganese and Iron Manganese	27
2.5.2	Ferromagnet: Cobalt	29
2.5.3	AF/FM Systems: FeMn/Co and IrMn/Co	29
3	Magneto-Optical Kerr Effect	31
3.1	MOKE Phenomenology	32
3.2	Fresnel Reflection Coefficients	34
4	Ultrafast Magnetization Dynamics	38
4.1	Spin Waves	39
4.2	Spin Dynamics—Magnetic Motion	40
4.3	Landau-Lifshitz and Gilbert Equation	40
4.4	Approximate Solution to the LLG	43
4.5	Ferromagnetic Resonance	43
4.5.1	Free Energy Terms in FMR	47
5	Samples and Experiments	50
5.1	Sample Growth	50
5.2	Sample Characterization	51
5.2.1	Superconducting Quantum Interference Device (SQUID)	52
5.2.2	Magnetic Hysteresis Measurement	52
5.2.3	Ferromagnetic Resonance	53

5.3	Static MOKE	54
5.4	Ultrafast Pump-probe MOKE	56
6	Static MOKE on IrMn/Co and FeMn/Co	59
6.1	Experimental Details	60
6.1.1	Errors and Uncertainties	61
6.2	MOKE curves	62
6.3	Co Thickness Dependence of H_{EB} and H_C	64
6.3.1	FeMn: Effects of Buffer Layers on H_{EB} and H_C	67
6.3.2	Interface Exchange Energy	68
6.4	Switching Field in a Wedge	69
6.5	Angular Dependence of H_{EB} and H_C on FeMn	72
7	Pump-probe MOKE Results	75
7.1	Experimental Details	76
7.2	Ultrafast Oscillations	76
7.3	FMR Analysis of Pump-Probe Data	78
7.4	H_{EB} - H_A Angle Dependence of Spin Wave Frequencies	84
7.5	Damping Coefficient	86
7.6	Pump-probe Hysteresis Loops	87
8	Pump-Induced Exchange Biasing	94
8.1	Background	94
8.2	Model of Pump-Induced Setting of Exchange Biasing	97
8.2.1	Overcoming an Energy Barrier	99
8.3	Evidence for Pump-Induced Pinning	102
8.3.1	Static Laser Repinning	102
8.3.2	Ultrafast Laser Repinning	104
8.4	Comparison of Pump Powers to the Literature	110

9	Conclusions and Outlook	112
9.1	Summary	112
9.2	Future Work	114
APPENDIX A		
	Symbols	115
	Bibliography	117
	Vita	127

ACKNOWLEDGMENTS

I would like to first thank Dr. Anne Reilly, my advisor, for her guidance through my time here. She has always been there to provide enthusiasm and perspective during the research process. This work would not be possible without her support and encouragement. I would also like to thank the committee for their participation, insightful comments, and questions in the review of this dissertation.

My thanks to those who have helped in the completion of this work: Bill Egelhoff Jr. and Li Gan at NIST for growing and characterizing samples, Russel “Buzz” Winchewski at NASA LARC for SQUID measurements, and Jim Rantschler at NIST for FMR measurements.

My gratitude goes to my research-mate Hailong Huang for his assistance with the FMR fits, optical experiments, and inspiring discussions. This would have been very difficult to complete without him. I would also like to thank Haibin Zhao and Yuhang Ren for providing valuable assistance with the experiments and laser work. My thanks to William Cline for feedback on the grammar, readability, and content of this work.

Without the secretaries in this department, nothing would be accomplished. Thanks to Dianne Fannin, Carol Hankins, Paula Perry, and Sylvia Stout for your support, recipes, and lunchtime conversation.

I would like to acknowledge my friends who have treated me like family; you know who you are. All of you have made the journey worthwhile. Thank you.

LIST OF TABLES

Table	Page
2.1 Demagnetization field and Curie temperature for various ferromagnets. . .	10
7.1 Extracted values for H_D and H_{EB} using Eq. (4.23) for various angles between H_{EB} and H_A	81
7.2 Extracted values for H_D and H_{EB} as a function of applied field using Eq. (4.23) for IrMn/25 nm Co.	85
8.1 Comparison of pump powers for various experiments in the literature. . .	110

LIST OF FIGURES

Figure	Page
2.1 Illustration of the demagnetization of a bar magnet.	11
2.2 The general ellipsoid and oblate spheroid used in calculating the demagnetization factor.	12
2.3 Schematic of the two different types of 180° domain walls.	13
2.4 Hysteresis loop of a pure cobalt film.	14
2.5 Origin of exchange bias in a magnetic two-layer film.	18
2.6 The difference between compensated versus uncompensated spins in the AF layer.	19
2.7 Different configurations for partial domain wall in the AF layer.	23
2.8 The CuAu (L1 ₀) structure of IrMn.	28
3.1 Interpretation of the Kerr rotation using rcp and lcp light.	32
3.2 Geometry for a magneto-optical Kerr effect experiment.	33
3.3 Real part of the longitudinal Fresnel reflection coefficient versus angle of incidence of the reflected light for incoming <i>p</i> -polarized light.	36
4.1 Illustration of a spin wave propagating through the lattice with lattice spacing <i>a</i>	39
4.2 Motion of an undamped magnetization <i>M</i> in an applied field <i>H</i>	41

4.3	Directions of the vectors and motion of the magnetism in the Landau Lifshitz Gilbert equation.	42
4.4	Plot of the approximate solution to the LLG equation for different damping parameters α	44
4.5	Coordinates for description of the free energy terms.	48
5.1	Setup for a ferromagnetic resonance experiment.	53
5.2	Magneto-optical Kerr effect experimental setup.	54
5.3	Schematic of the amplified laser system.	56
5.4	Pump-probe MOKE setup.	57
6.1	Sketch of samples used in the MOKE experiments.	61
6.2	Easy axis MOKE curves on wedged-Co samples.	63
6.3	H_{EB} and H_C as a function of inverse Co thickness for a IrMn/Co wedge sample.	65
6.4	H_{EB} and H_C as a function of inverse Co thickness for a FeMn/Co wedge sample with a Ta/Cu buffer layer.	65
6.5	Inverse thickness dependence of H_{EB} (left) and H_C (right) on FeMn/Co with a W/Cu buffer layer.	67
6.6	Comparison of interfacial exchange energies for different wedge systems.	69
6.7	Switching field ($H_{EB} \pm H_C$) as a function of thickness for two wedges of IrMn/Co and FeMn/Co.	70
6.8	Schematic of domain wall motion in a wedged Co sample	71
6.9	H_{EB} and H_C as a function of angle between the applied field and H_{EB} for FeMn/(12 / 35 nm) Co.	73
7.1	Pump-probe MOKE signal as a function of pump-probe delay in various external applied fields.	77

7.2	Extracted oscillation frequency versus external field for IrMn/25 nm Co.	79
7.3	Extracted oscillation frequency versus external field for IrMn/12 nm Co.	80
7.4	SQUID measurement of the perpendicular component of the magnetization on IrMn/12 nm Co.	83
7.5	Angular dependence of the spin-wave frequency for fixed external fields for IrMn/25 nm Co.	85
7.6	Damping parameter α versus applied field.	87
7.7	Easy axis hysteresis loops for various delay times between pump and probe for an IrMn/15 nm Co sample.	88
7.8	Hard axis hysteresis loops for various delay times between pump and probe for an IrMn/15 nm Co sample.	90
7.9	Three dimensional map of the decreasing field for IrMn/15 nm Co along the hard axis.	91
7.10	Theoretical model of Fig. 7.9 using the FMR (Eq. (4.23)) and oscillation fit (Eq. (4.8)) equations.	92
8.1	Sketch of the conditions necessary for oscillations along the easy axis.	96
8.2	Oscillation frequency data for IrMn/(12,25 nm) Co along the easy axis.	98
8.3	Sketch of the thermally activated model for switching.	100
8.4	Sketch of the AF grains during magnetization reversal at different points in the hysteresis loop.	101
8.5	Static MOKE curves taken as a function of the incident pump power for a IrMn/3 nm Co sample.	103
8.6	MOKE, then pump-probe, then MOKE to show that the pump beam induces exchange biasing.	105
8.7	MOKE, then pump-probe, then MOKE on a IrMn/12 nm Co sample along the hard axis.	107

ABSTRACT

We have studied the exchange bias interaction in metal bilayers IrMn/Co and FeMn/Co using the static and ultrafast pump-probe Kerr effects. Experiments conducted on wedged Co samples show that the exchange bias interaction is sensitive to the buffer layers grown beneath it when the antiferromagnetic layer is FeMn. The exchange bias strength, as measured by the shift in the magnetic hysteresis loop, follows a $1/t_{\text{FM}}$ dependence as reported in the literature. The time-domain pump-probe experiments reveal coherent magnetization oscillations, whose frequencies are comparable to those measured by frequency-domain FMR measurements, and they fit well to FMR equations for the frequency. We have also been able to use the pump beam to permanently alter the exchange bias interface which leads to the launching of oscillations along new geometries, particularly along the easy axis where magnetization is aligned with the applied field. This is explained qualitatively by showing that the pump has enough energy to overcome the energy barrier in the AF, allowing it to flip and provide a torque on the magnetization that launches oscillations.

**STATIC AND ULTRAFAST MOKE STUDIES OF EXCHANGE-BIASED COBALT
SYSTEMS**

CHAPTER 1

Introduction

The understanding of switching in magnetic systems has become a critical problem in the physics of magnetic thin films. This issue will determine the ultimate speeds of magnetic devices such as magnetic random access memory devices (MRAM), the non-volatile type of RAM where information is stored either in magnetic tunnel junctions or magnetic spin valves [1]. As opposed to conventional RAM where the information is stored as electric potentials, MRAM stores the information using electron spins that have the advantage that they require no power to hold the state of the magnetization and will remain in a given state until flipped by a magnetic field. This is a crucial step for new systems, especially space-based satellites where power requirements are an important criterion in choosing technologies. In addition to MRAM, magnetic multi-layers are also important for the design of magnetic sensors, often used in computer guidance systems. With both of these applications the switching behavior of magnetic spins becomes important, since it sets the fastest timescale for MRAM speeds and sensor response time [1].

Exchange biasing refers to an interaction between antiferromagnetic (AF) and ferromagnetic (FM) layers grown adjacent to each other in a thin film [2]. These layers, when

cooled from high temperature in an applied field show a shift in the magnetic hysteresis loop and an enhancement in the coercivity due to the interface interaction between the AF and FM. This shift is typically opposite to the direction of the applied field [3], and is known as the exchange bias field H_{EB} or pinning field. Exchange-biased bilayers are used in magnetic spin valves and tunnel junction devices to give control over the magnetization state.

Understanding the dynamic behavior of exchange-biased bilayer systems is also important, as these bilayers are used in magnetic devices to allow for the control of the direction of magnetization, can stabilize the magnetization in nanostructures [4].

The use of exchange-biased layers in computer technology has boomed over the last ten years. Their main use is to provide a strong pinning layer in giant magnetoresistive (GMR) sensors. GMR is an effect discovered in 1986 [5, 6] where the resistance measured from an applied current depends drastically on an applied field. These sensors are built using an exchange-biased bilayer, a non-magnetic layer (typically copper), and another FM layer. They are used to detect the small magnetic fields of a magnetic disk drive as it scans over the platter surface of the media. By applying a current, one can detect if the magnetization of the two FM layers are aligned (low resistance) or anti-aligned (high resistance). These two states are the 1 and 0 in computer memory.

1.1 Review of Current Literature

Exchange biasing is widely studied but still not well understood. The properties of the exchange-biased bilayers are difficult to study, since they depend on several dependent parameters such as crystal structure, interface roughness, blocking temperature, anisotropies, and grain size [7].

The recent discovery of ultrafast optical control of magnetization processes has generated much work aimed at understanding the switching behavior and processes in mag-

netic systems [8, 9, 10, 11, 12, 13, 14]. The basic experiments involve a pump-probe technique: a pump laser pulse creates a modification of the magnetization or magnetic anisotropy, while the delayed probe detects the real-time changes in the magnetization through the magneto-optical Kerr effect (MOKE). In one category of experiments, spin waves are excited by a pulsed magnetic field generated by the pump beam through an ultrafast optical switch [15]. An alternative experiment is all-optical: spin waves are excited directly by a pulsed laser beam incident on the sample [8, 10]. It has been demonstrated that coherent spin waves can be excited in this way in any ferromagnetic thin film with anisotropy, in the proper geometry. The optically induced spin waves have been shown to give analogous information to ferromagnetic resonance (FMR) and Brillouin light scattering (BLS), such as spin wave frequency and damping parameters [10].

The method of probing the switching behavior in exchange-biased systems using all-optical ultrafast techniques was first introduced by Ju *et al.* [8, 9] on the AF/FM system NiO/NiFe. In these experiments, the pump beam was used to directly excite the NiO/NiFe interface. The pump laser pulse leads to electron heating and momentary thermal destruction of the exchange bias interaction. The destruction and recovery of the exchange bias interaction launches spin waves which are modeled using the Landau-Lifshitz and Gilbert (LLG) equation. Subsequent experiments by Weber *et al.* [13, 16] on FeMn/NiFe, IrMn/CoFe, and NiMn/CoFe experimentally verified the exponential recovery of the exchange bias by measuring the hysteresis loops at different pump-probe delay times as well as correlated the magnetic oscillations with shifts of the hysteresis loop.

In both of these experiments, the pump laser intensity was low enough that the recovery of the exchange bias interaction was nearly complete (that is, the exchange bias itself was not permanently modified, as indicated by a recovery of the hysteresis loop). Under these conditions, it was shown that oscillations could be produced only if the applied field was less than the saturation field and the applied field is not along the H_{EB} direction. Once the applied magnetic field was large enough to pull all of the magnetization into

the direction of the applied field the oscillations disappear, as this is the minimum energy state. No torque exists on the magnetization to induce oscillations [9].

This Dissertation reports studies on the quality of exchange biasing for two AF/FM systems, IrMn/Co and FeMn/Co. We report that the exchange biasing and coercivity in FeMn/Co are sensitive to the buffer layers on which they are grown, leading to anomalous magnetic properties.

We also report the excitation and detection of coherent magnetization oscillations in exchange-biased thin films in a new regime: one in which the pump laser intensity is high enough to permanently change the exchange bias interaction at the interface. This pump-induced modification launches long-lived, single-frequency oscillations that can be observed for any applied magnetic field and any in-plane angle. The behavior of the oscillation frequency with field corresponds to that measured by ferromagnetic resonance and may be fit using FMR analysis of the LLG equation. This is explained qualitatively by showing that the pump pulse has enough energy to overcome the energy barrier between aligned and anti-aligned states in the AF. In addition to the magnetization oscillations, we also report that using ultrafast laser pulses we can induce the exchange bias effect, or pinning, in an unpinned sample. This a new way to induce pinning in exchange-biased structures, which uses the laser pulse to heat the electronic temperature while the lattice temperature remains low.

1.2 Dissertation Outline

The Dissertation is separated into three parts. The first part introduces magnetism theory, the Kerr effect, and Landau-Lifshitz and Gilbert theory. The second part introduces the experimental setup and the thin-films used in the experiments. The third part presents the experiments conducted on the thin films with an interpretation of the results using contemporary theories.

Chapter 2 introduces the concepts of magnetism and magnetic materials and effects that are seen in magnetism, such as anisotropy, demagnetization, blocking temperature, and compensation. A special unidirectional anisotropy called exchange biasing is also introduced as well as the consequences of exchange biasing and effects that are unique to exchange-biased structures. Various models to explain exchange biasing are introduced along with a summary of the literature on the magnetic systems that are used in this dissertation, IrMn/Co and FeMn/Co.

Chapter 3 is an introduction to the theory for the magneto-optical Kerr effect. The Kerr effect is the tool that we use to probe the magnetization of ferromagnetic layers. A conceptual description as well as an analysis using Fresnel coefficients is given that lead to a simple method to probe the magnetization of a sample.

Chapter 4 considers the theory of magnetization dynamics under an applied field. The spin wave is introduced along with its associated particle—the magnon. The spin waves can be characterized by the Landau-Lifshitz and Gilbert (LLG) equation which governs the movement under and applied field. Two special cases of the LLG are discussed: small damping and no damping. For small damping, an expression for the damping parameter is derived. For no damping, the expression for the spin-wave frequency is derived. This expression for the spin-wave frequency is commonly used in FMR experiments to extract material parameters.

The sample growth and characterization are explained in Chapter 5. Auxiliary techniques such as the BH looper and FMR are introduced along with the all-optical MOKE and ultrafast pump-probe MOKE experiments are discussed. An overview of the ultrafast laser system and the amplification process of the laser is given.

Chapter 6 presents experimental results from the static MOKE studies on IrMn/Co and FeMn/Co. The systems have Co wedges that allow for accurate control over the exchange bias interaction by varying the Co thickness. The Co thickness dependence of the exchange biasing is shown to be sensitive to the buffer layers grown beneath it. The

wedge structures also exhibit a single domain wall that travels through the FM as the field is increased. The interface exchange energy is calculated for the wedges and is shown to be comparable to the literature. The angular dependence of the exchange bias interaction was also studied and it was shown for FeMn the pinning can be good.

Chapter 7 presents measurements on exchange-biased structures using the ultrafast pump-probe MOKE technique. The oscillations observed are shown to follow the FMR equation, providing us with a time-domain measurement of the same quantities that are observed in the frequency-domain FMR measurement. The rotational dependence of the oscillation frequencies is discussed and the damping parameter are extracted from the decay times. The damping parameter falls within the range of other literature values. The dynamic response of the hysteresis loop is also measured, which shows that for the easy axis there are peaks in the dynamic hysteresis loop which roughly correspond to the switching field of the static hysteresis loops. The dynamic hysteresis loops are modeled using the FMR equation and are shown to have similar features.

Chapter 8 is the final experimental chapter which addresses mechanisms for oscillation including our model of pump-induced exchange biasing. Previous work by other groups has not seen oscillations along the easy axis where the field is large enough to saturate the sample. Our results in Chapter 7 show clearly that oscillations are present at large fields where the magnetization is aligned with the applied field. We show that the pump can induce an exchange-bias shift on a previously unpinned samples. A qualitative model is offered to explain the results in our experiments.

Chapter 9 concludes the dissertation with a summary of the previous chapters. The final part suggests further experiments and improvements that may be made in the current experiments to maximize data collection.

Appendix A lists the mathematical symbols that are repeatedly used in this Dissertation. It should be used as a guide to finding the meaning of a symbol or the section that it is discussed.

CHAPTER 2

Magnetism and Exchange Bias

This Chapter introduces the basic concepts of magnetism and the current theories on exchange biasing. It focuses on the general phenomena that occur in ferromagnets (FM), antiferromagnets (AF) and thin film effects in polycrystalline systems. In general, the focus will be on the FM cobalt and AF IrMn and FeMn, as these are the materials used in the experiments in this thesis.

The nature of exchange biasing is still not understood well enough to allow for a theory that is generalized to all natural systems. Current theories, only applicable to select materials, can account for most of the effects observed [2, 17, 18]. The theories applicable to our IrMn, FeMn, and Co polycrystalline systems shall be discussed in this Chapter.

2.1 Ferromagnetism

Fundamentally, magnetism arises due to the orbital and spin angular momentum of electrons. To approach magnetism in the bulk, one has to first look at the interactions between adjacent electron spins. Different materials exhibit different alignment of

spins, giving rise to either diamagnetism, paramagnetism, ferromagnetism, or antiferromagnetism. Assume that we have a collection of lattice sites, each with a single magnetic spin. For ferromagnetic and antiferromagnetic materials, the magnetic interaction between adjacent spins in a 1-dimensional lattice can be represented quantum mechanically as [19]:

$$\mathcal{H} = -2J_e \hat{S}_i \cdot \hat{S}_j, \quad (2.1)$$

which is similar to the spin interaction Hamiltonian. Here, \hat{S}_i and \hat{S}_j are the total spin on lattice sites i and j respectively, and J_e is the direct exchange integral between the two spins. This exchange integral is difficult to calculate in general and arises from the swapping of electrons among atoms on adjacent lattice sites [20]. Heisenberg first proposed this model as an explanation for ferromagnetism in 1928 [19].

Now if we consider Equation (2.1) and assume that the spins interact with nearest neighbors, the requirement that $J_e > 0$ allows for the spins S_i and S_j to align parallel to each other to minimize the exchange energy, creating ferromagnetic ordering. Few elements exist with $J_e > 0$ at room temperature, namely iron (Fe), cobalt (Co), and nickel (Ni).

Ferromagnetic materials also exhibit a temperature dependence of their magnetic properties. The magnetic susceptibility follows the Curie-Weiss law given by

$$\chi \propto \frac{1}{T - \Theta}, \quad (2.2)$$

where Θ is called the Curie-Weiss temperature. The singularity at $T = \Theta$ is the point where thermal effects in the system affect it to the point where the magnetic susceptibility has a discontinuity and magnetic ordering is no longer possible. Θ is known as the Curie-Weiss temperature or simply the Curie temperature. This can be derived from a molecular mean field theory based on the assumption that the molecular field is proportional to the magnetization [21]. Table 2.1 lists the Curie temperatures of common ferromagnetic

materials. Below the Curie-Weiss temperature, the system orders itself ferromagnetically. The Curie temperature is determined by the competition between thermal effects and the long-range magnetic ordering in the crystal.

Material	H_D @ 293 K (Oe)	T_c (K)
Fe	21580	1043
Co	17900	1404
Ni	6084	631

TABLE 2.1: Demagnetization field and Curie temperature for various ferromagnets. These are taken from Ref. [20].

2.1.1 Demagnetization Fields

Because of the finite size of magnetic materials, a natural demagnetizing field exists in the material. This is due to the uncompensated or unpaired poles at the end of a bar magnet. This is illustrated in Figure 2.1. Suppose a field is applied to a unmagnetized bar along the length of the magnet shown in Fig. 2.1 (a). This causes an alignment of the magnetic poles. Once that external field is removed, the north and south poles generate a magnetic auxiliary field H and magnetic field lines shown in Fig. 2.1 (b). Inside the sample these generated field lines oppose the direction of the initial magnetic field, which leads to a demagnetizing effect on the bar. The B field lines must form a closed loop, shown in Fig. 2.1 (c).

In general, the demagnetization field H_D depends on the magnetization:

$$H_D = N_d M_S, \quad (2.3)$$

where M_S is the saturation magnetization of the sample and N_d is the demagnetizing factor. The demagnetization factor depends on the shape of the magnet and can only be solved exactly for an ellipsoid. The demagnetization term is identical to the term defined

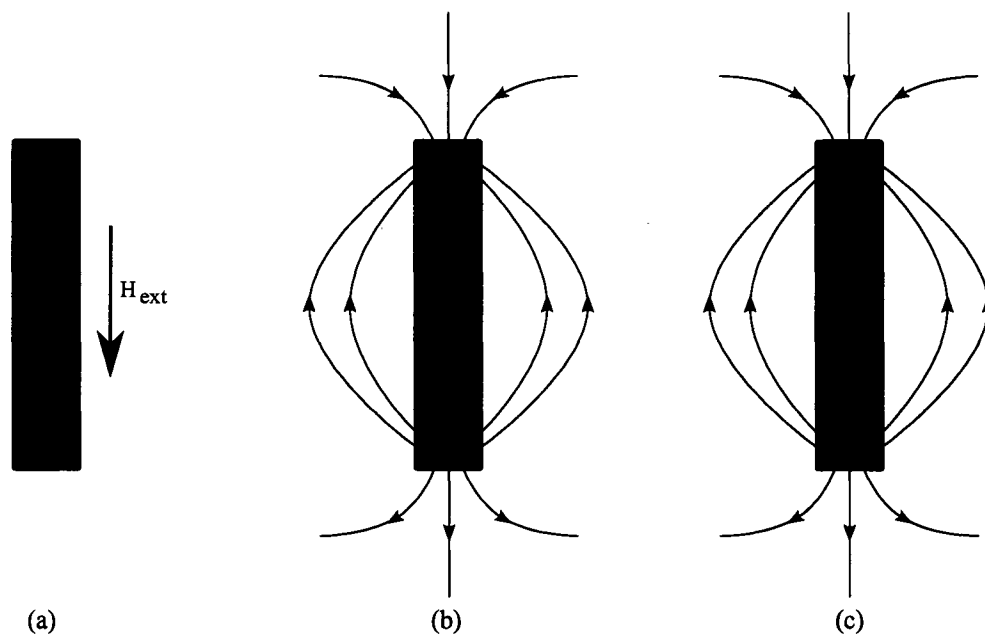


FIG. 2.1: Illustration of the demagnetization of a bar magnet. The material is magnetized by an external magnetic field H_{ext} pointing down. This aligns the north and south poles with H_{ext} and generates field lines shown in (b), given by H . These field lines are opposite to the external field shown in (a), thus each one tends to demagnetize the bar magnet. The field lines in (c) show the closed loops formed from the B field.

in the magnetic field in cgs units ($\mathbf{B} = \mathbf{H} + 4\pi\mathbf{M}$). This leads to the conclusion that the maximum value for the demagnetization factor is $H_D = 4\pi M_S$. The demagnetization factor can further be broken up into independent factors that depend on the direction of the principal axes shown in Figure 2.2 (a). The demagnetization factor may be rewritten such that

$$N_d = N_a + N_b + N_c = 4\pi, \quad (2.4)$$

where the subscripts a, b, c represent the demagnetization factor along that axis.

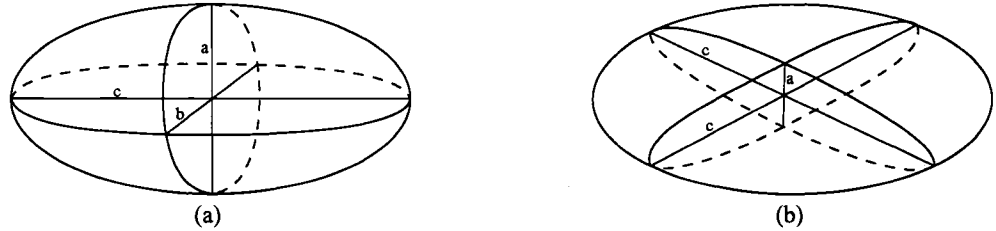


FIG. 2.2: The general ellipsoid and oblate spheroid used in calculating the demagnetization factor. For the general ellipsoid, the demagnetization factors differ depending on the axis being considered. In the oblate spheroid (b), two of the principal axes c are equal and $a < c$. This can be used as a thin film in the limiting case of $c \rightarrow \infty$.

In a special case, the ellipsoid can be extended such that the result may be used for a thin film. The result will be quoted here, but the details on the derivation can be found in Ref. [22]. For an oblate spheroid shown in Figure 2.2 (b), $b = c > a$ and the demagnetization factors are [20]

$$N_a = \frac{4\pi r^2}{r^2 - 1} \left(1 - \sqrt{\frac{1}{r^2 - 1}} \arcsin \left(\frac{\sqrt{r^2 - 1}}{r} \right) \right), \quad (2.5)$$

$$N_b = N_c = \frac{4\pi - N_a}{2}, \quad (2.6)$$

where $r = c/a$ is a ratio of the axes. For a thin disk, $c \rightarrow \infty$, $r \rightarrow \infty$ and

$$N_a = 4\pi, N_b = N_c = 0. \quad (2.7)$$

Therefore, $H_D = 4\pi M_S$ directed out of the plane of the disk. These demagnetization factors can be quite large and will play a role in the models introduced in Chapter 4.

Table 2.1 lists the demagnetization fields for the elemental ferromagnets. The values are significant, with Co and Fe having demagnetizing fields larger than 1 Tesla (10,000 Oe). Physically, this represents the applied field required to pull the magnetization from in the plane of the film to out of the plane of the film.

2.1.2 Domains and Domain Walls

Because the value of the demagnetization field can be large, it is not energetically favorable for a ferromagnetic material to have all of its spins aligned across the material. This is how one can have unmagnetized iron. Unmagnetized iron is fairly common, but should not be possible (below the Curie temperature) since the spontaneous magnetization of FM systems would cause a net magnetization. Weiss provided the answer by suggesting that the Fe aligns into small regions of spontaneously magnetized regions he called domains [20]. The domains point randomly in different directions, filling the requirement that the iron be magnetically saturated but still have a net magnetization of zero.

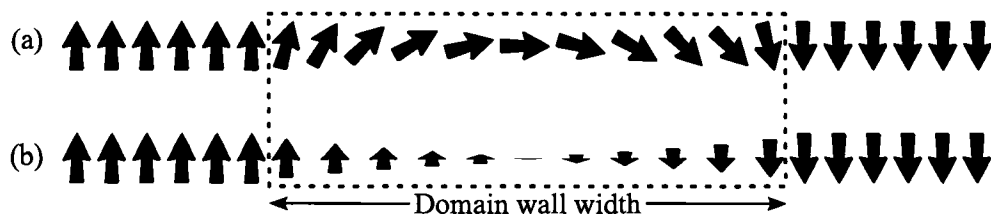


FIG. 2.3: Schematic of the two different types of 180° domain walls. The domain wall region is shown in the dotted box. Above in (a) is a Néel wall where the magnetization rotates in the plane formed by the magnetization on each side of the wall. Below in (b) is a Bloch wall where the magnetization rotates out of the plane formed by the magnetization on each side of the wall.

The region between domains is known as a domain wall. The application of a magnetic field to an unmagnetized ferromagnetic sample moves the domain walls such that the net magnetization is non-zero. Two distinct types of domain walls exist. The Bloch wall (named after Felix Bloch) predominantly occurs in bulk materials with the magnetization rotating perpendicular to the magnetic domain directions. The other type of domain wall

is a Néel wall which occurs in thin films. In the Néel wall the magnetization rotates in the plane of the magnetic domains. Figure 2.3 illustrates the difference between the Néel (above, green) and Bloch (below, blue) walls. Because of the large demagnetization field in thin films (17.9 kOe for Co) that pushes the magnetization in plane, it is energetically favorable for thin film domain walls to be Néel walls. Figure 2.4 shows a plot of the magnetization versus applied field for a Co sample. A cartoon of the stepwise switching of individual domains known as the Barkhausen effect is shown inset of Fig. 2.4.

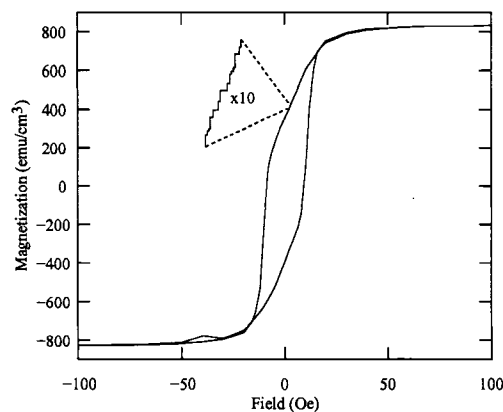


FIG. 2.4: Hysteresis loop of a pure cobalt film. Inset is a zoomed in schematic showing the stepwise switching of FM domains in the film. These are known as Barkhausen jumps or the Barkhausen effect.

Domains are large compared to the thickness of most thin films. For example, the domain size for Co is approximately $4 \mu\text{m}$ [23, 24] whereas film thicknesses are on the order of 5–50 nm.

2.1.3 Magnetic Anisotropy

Experimental hysteresis loops on FM single crystal materials show that the shape of the hysteresis loop changes as the sample is rotated about the applied external field. This implies that materials have preferred magnetic orientations. This is known as magnetic anisotropy. The simplest situation is uniaxial anisotropy, which originates from the

underlying crystal structure.

In a uniaxial system, the magnetization has a preferred direction along the crystal axis. This means that the free energy has two minima separated by 180° . One can write the free energy for a uniaxial system in terms of a power series in $\sin^2 \theta$, where θ is the direction between the magnetization and crystal axis.

$$F_{\text{UA}} = K'_1 \sin^2 \theta + K'_2 \sin^4 \theta + \dots, \quad (2.8)$$

where K'_1 and K'_2 are the first and second order anisotropy constants, respectively. Higher order terms are ignored because they are small compared to first and second order. For Co, $K'_1 = 4.1 \times 10^6$ ergs/cm³ and $K'_2 = 1 \times 10^6$ ergs/cm³ [25].

The free energy is a minimum when the $\theta = 0^\circ, 180^\circ$. This direction is known as the easy axis. When the free energy is a maximum, $\theta = 90^\circ, 270^\circ$, and this orientation is known as a hard axis. The uniaxial anisotropy is an artifact of crystal structure as polycrystalline materials do not exhibit this behavior because their grains are oriented randomly which average the effect out. Although the uniaxial anisotropy does not play a large role in polycrystalline systems, the concept of anisotropy is important and a specific kind of anisotropy will be discussed in Sec. 2.3.

2.2 Antiferromagnetism

In an antiferromagnetic lattice, there are two sets of sublattices which are oriented such that their spins are anti-parallel to each other. At first glance, it may seem that the direct exchange between adjacent lattice sites and Eq. (2.1) applies here with $J_e < 0$, but the exchange interaction falls off rapidly as a function of distance and AF compounds have a much longer atom-to-atom distance than the FM metals [25]. Although the AFs IrMn and FeMn are used in this Dissertation, the mechanism for antiferromagnetism is not necessary to understand this work and will not be discussed here.

Because of the strict requirement that the lattice be constructed of two sublattices of opposite directions, elemental antiferromagnetism is quite rare. The only elements that exhibit antiferromagnetism are chromium (Cr) and manganese (Mn) and their mechanisms for AF ordering are complex. Various AF compounds exist such as metal oxide insulators (NiO, CoO, FeO, Fe₃O₄) or metallic compounds of the elemental antiferromagnets (IrMn, FeMn, PtMn, CrAl) [2].

2.2.1 Grains, Antiferromagnetic Domains, Néel and Blocking Temperature

The samples used in this thesis are polycrystalline, that is, they are made up of regions (called grains) of crystalline order. Most models of magnetism are based on the assumption that for polycrystalline systems the individual grains behave independent of each other. Models that use this assumption will be discussed in Sec. 2.4.4 and Sec. 2.3.3. FM layers may also contain grains, but usually their effect on exchange biasing is ignored.

The concept of domains and domain walls is not restricted to FM systems. Antiferromagnetic domains can exist in materials particularly at an interface between an AF system and another system (for example, an FM system) [26, 27].

Similar to the effect of the Curie temperature in FM materials, AF systems have a temperature at which the heat in the system is larger than the AF ordering and the system magnetically disorders. This is called the Néel temperature. In polycrystalline systems, the Néel temperature and the temperature at which the system magnetically disorders are not the same due to a distribution of grains and their size. This effective temperature where the magnetic state disorders is called the blocking temperature [28]. In polycrystalline films there are a distribution of grain sizes, which leads to a decrease in the blocking temperature because individual grains have different blocking temperatures that depend on their grain size. In films with larger polycrystalline grains, the blocking tem-

perature is on the order of the Néel temperature [29]. Since a single crystal is a single grain, the blocking temperature is about the same as the Néel temperature [30].

2.3 Exchange Bias

Exchange bias is a phenomenon that occurs when a thin (<30 nm) film of FM material is grown adjacent to an AF material. It can be described as an interaction between the AF/FM interface where the interaction causes a unidirectional anisotropy in the FM layer. The energy in the system is minimized when the magnetization is aligned along this preferred direction. The unidirectional anisotropy adds a term to the free energy given by

$$F_{\text{EB}} = -\mathbf{M} \cdot \mathbf{H}_{\text{EB}} = -M_S H_{\text{EB}} \cos \theta, \quad (2.9)$$

where H_{EB} is the exchange bias field and θ is the angle between the exchange bias field and magnetization directions. To create an exchange-biased system, an AF/FM interface is heated near or above the Néel temperature, causing the AF material to become disordered. The interface is then cooled slowly in a magnetic field, causing the system to reorder itself along the magnetic field direction and an anisotropy is formed in the direction of the applied magnetic field, as shown in Figure 2.5a. The cooling in a magnetic field is crucial to obtaining the exchange anisotropy, since this is the cause of the reordering of the AF spins. Once it is cooled, the FM layer is said to be “pinned”, that is, the AF layer exerts a torque on the FM layer at the interface which gives it a preferred direction.

The phenomenon manifests itself as a shift of a hysteresis loop in a M-H trace plot, as seen in Fig. 2.5. The shift of the loop from zero is called the exchange bias field, H_{EB} . The half-width of the loop, known as the coercive field or H_C , is enhanced in the exchange bias interaction as well. At point (b) in Fig. 2.5, the applied field H_A and FM spins are in the same direction. As the field is decreased the FM spins to rotate slightly as seen in (c). When the field is in the opposing direction at (d), the spins have completely

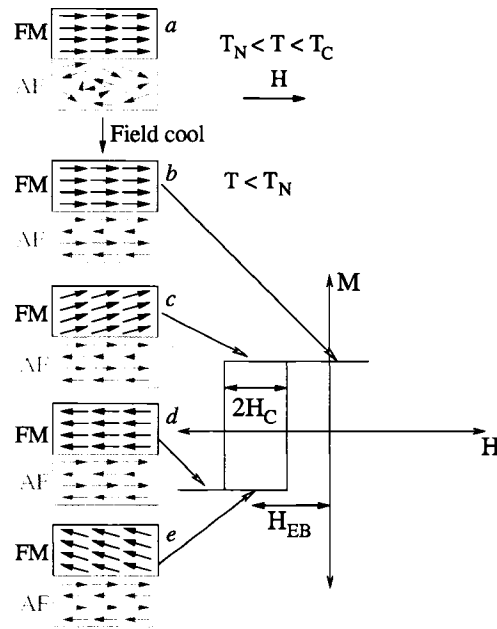


FIG. 2.5: Origin of exchange bias in a magnetic two-layer film. The exchange bias is formed by cooling in a magnetic field from above the Néel temperature to reorder the AF, seen in (a) In (b)–(e), the orientations of the AF and FM spins on a hysteresis loop are shown. From Ref. [2].

flipped. When the field is increased again, the spins slightly rotate at (e) until each one has completely flipped by the increasing field at (b).

In most systems¹, the loop shifts opposite to the applied field during cooling. Since the FM/AF layer has a ground state in positive saturation, for example, it will oppose switching to negative saturation causing loop to be shifted in the negative direction [28].

2.3.1 Compensated and Uncompensated Spins

Since the exchange bias is an interface effect, one expects the spin configuration at the interface to influence the exchange biasing significantly. In particular, the AF spin configuration has been discussed as a contributor to the exchange bias. Two main configurations of the AF lattice at the interface exist: one where the average of the magnetic moment over a macroscopic region is non-zero (uncompensated), and one where the aver-

¹Under special conditions FeF_2/Fe exhibits a loop shift in the same direction as the applied field after cooling [3].

age is zero (compensated). The two configurations are sketched in Figure 2.6. Fig. 2.6 (b) illustrates interface interactions between the AF and FM that are frustrated. Frustration occurs when the AF/FM moments at the interface are anti-aligned, which is energetically unfavorable. These are marked in Fig. 2.6 (b) as red stars. Fig. 2.6 (c) shows an interface where all of the interactions are partially frustrated.

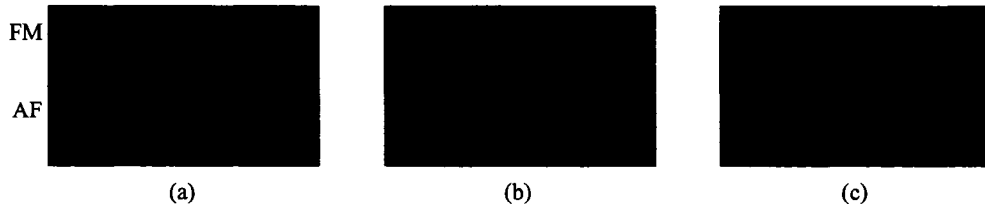


FIG. 2.6: The difference between compensated versus uncompensated spins in the AF layer. At the interface, the AF spins in (a) are all pointing in the same direction. These uncompensated spins lead to a net magnetic moment that the FM can couple to during cooling. None of the interactions across the interface are frustrated. Compensated spins shown in (b) have equal amounts of anti-aligned spins, yielding no magnetic moment at the interface. Also marked is the frustrated interactions across the interface. Shown in (c) is a compensated configuration as in (b) but the coupling to the FM layer is perpendicular and the AF spins are pointing in and out of the paper. This is discussed in Sec. 2.4.3. All of the interactions in (c) are partially frustrated. The first 3 monolayers (ML) of the FM and the first 6 ML for the AF at the interface are shown.

The results from materials systems have shown that exchange biasing can occur in both compensated and uncompensated interfaces. This is puzzling for the compensated interfaces since the total magnetic moment at the interface is zero. Models of compensated systems suggest that the AF spins at the interface rotate slightly [31] or introduce a partial domain wall in the AF [26, 27] in order to achieve coupling. These will be discussed in Section 2.4.

2.3.2 Effects of Interfacial Roughness

Since the exchange bias is an interface effect, it is generally thought that the roughness of the interface will affect the exchange strength and loop shift. In most systems, increasing roughness decreases the magnitude of H_{EB} [32, 33, 34, 35, 36]. This inverse

relationship appears to be independent of the compensation at the interface [37], meaning both compensated and uncompensated surfaces are affected by roughness. In models where there compensated interfaces, roughness is thought to break the compensation locally such that a magnetic moment is created for coupling to the FM layer. In uncompensated models, roughness has been used to reduce the magnitude of the exchange bias predicted to moderate success [26]. The roughness model will be discussed in detail in Sec. 2.4.1.

2.3.3 Effects of Polycrystalline Structures

Because all the samples used in the thesis share a polycrystalline structure, it is important to identify effects of the polycrystalline structure. One of these is the application of the blocking temperature discussed in Sec. 2.2.1 to individual grains in a polycrystalline structure. Because of the distribution of grain sizes in a polycrystalline system, there is a distribution of temperatures where the grains become disordered. The idea of thermally activated reversal was first introduced by Fulcomer and Charap [28]. The basic assumption is that the AF system can be considered to be a group of non-interacting AF grains of varying size with two possible energy states. The grains interact individually with domains in the FM layer. There is a temperature, energy and time dependent probability that a given grain will remain in its state given by [38]

$$P(t) = \exp[-\nu t \exp(-\Delta E/k_B T)], \quad (2.10)$$

where ν is a parameter on the order of 1 GHz, ΔE is the energy difference between the two states, T is the temperature, k_B is the Boltzmann constant and t is time. Because different size AF grains contain different energy, there are different probabilities for reversal. There has been some success [39, 40, 41] with the model, but others [42] have discarded it for mean field models [43].

2.4 Models of Exchange Bias

The coupling at the interface has been studied extensively but is still not well understood. Various models have been proposed to explain experimental results. It may be that the exchange bias effect is material-dependent, but a unified theory has not been developed to describe the behavior for all systems. Various review papers have been published that summarize current models and outlook [2, 17, 18, 44, 7], which indicates the level of confusion in the field.

In this section we attempt to summarize the popular models in the literature and provide some background for the materials studied in this thesis work. Meiklejohn and Bean discovered the effect in 1956 on CoO/Co and proposed the first theory [45, 46]. Not until Malozemoff published his theory in 1987 [26] did work in the field accelerate. Since then there have been numerous articles in the literature attempting to model exchange bias with the eventual goal of understanding the phenomenon completely. This has proven a difficult task, as a large number of factors affect the exchange bias in these thin films. For example, growth method, AF crystalline structure, interfacial roughness, cooling procedure, FM crystalline structure, reversal mode, and training have all been implicated in some of these AF/FM systems [7]. The theories are designed to consider as many of these items as possible. In addition to the original papers, much of this discussion follows the review paper by Kiwi [44].

2.4.1 Meiklejohn: Coherent Rotation and Rotational Hysteresis

Initial work by Meiklejohn sought to explain the rotational hysteresis using a simple model of a single domain AF coupled to a single domain FM with a smooth interface [47]. The rotational hysteresis or rotational torque experiment measures the amount of work required to rotate the sample in an applied magnetic field. The work is plotted versus applied field. This experiment is an indication of losses, as non-zero work implies

that the system incurs energy loss. For a pure FM system, these losses disappear once the material is saturated. In an exchange-biased system, however, the losses remain even after saturation, indicating that AF spins are rotating along with the FM creating irreversible losses in the system [47].

Meiklejohn considered an uncompensated layer at the interface—that is, a layer where the sum of the AF spins at the interface is non-zero. For example, the interface is uncompensated when all of the spins at the AF interface are oriented in the same direction. The free energy function he used had the form

$$E = -HM \cos(\theta - \beta) + K_{AF} \sin^2(\alpha) - J_K \cos(\beta - \alpha), \quad (2.11)$$

where the first term is the interaction of the magnetization with the applied field, the 2nd term is the FM crystalline anisotropy with constant K_{AF} , and the third term is the exchange anisotropy energy with constant J_K .

The model from Meiklejohn correctly modeled the rotational hysteresis data if he considered that the magnetization rotated coherently and the crystalline anisotropy of the AF to be on the same order as the coupling between the AF/FM layers. If the coupling between the AF/FM layers was too large, the high field rotational hysteresis would disappear, yielding incorrect results. He did not address the loop shift, however subsequent experiments by Kouvel [48, 49] showed that the calculated loop shift was two orders of magnitude larger than the measured results from hysteresis loops. Although Meiklejohn could explain rotational hysteresis, he could not quantify the loop shift accurately.

2.4.2 Malozemoff: Random Field Model via Defects

After the initial work by Meiklejohn and Bean, research in the field declined until Malozemoff re-ignited it in 1987 [26]. His model tries to correct Meiklejohn's work by proposing that a partial domain wall parallel to the interface in the AF or FM would reduce the energy of an uncompensated interface, giving a result that is on the order of

the H_{EB} shift. A partial domain wall parallel to the interface is shown in Figure 2.7. It is a domain wall where the magnetization does not rotate a complete 180° . Fig. 2.7 shows two configurations of a 90° partial domain wall in the AF.

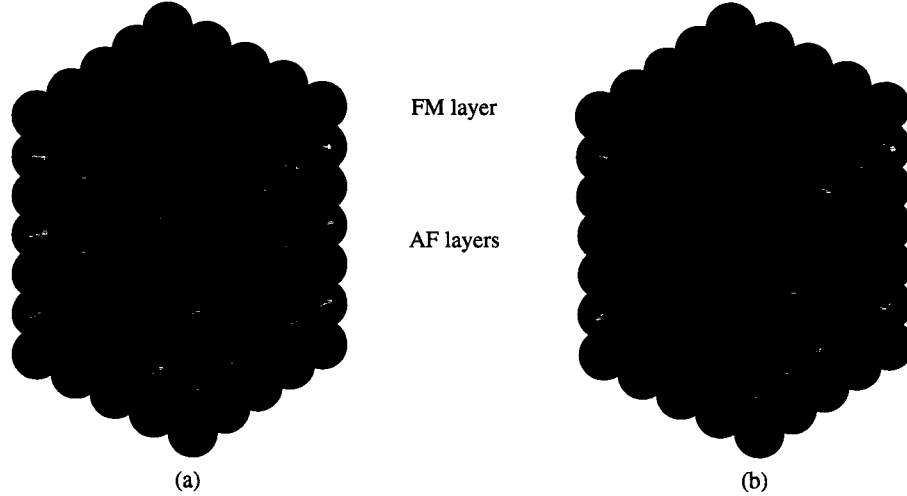


FIG. 2.7: Different configurations for partial domain wall in the AF layer. The top layer is the FM layer (black arrows), and the first three AF sub-lattices are shown with dark and light arrows. The domain wall is called partial domain wall because the angle between the magnetization on either side of the domain wall is less than 180° . The difference between (a) and (b) is the bulk spin configurations, shown by the bottom set of arrows, are aligned opposite to each other. Taken from Ref. [27].

The argument for the planar domain wall is based on frustration and compensation introduced in Sec. 2.3.1. If the magnetization could rotate to form a partial domain wall in either the AF or FM at the interface, there may be a favorable configuration since one can achieve a fully uncompensated interface, decreasing frustration. The cost for the reduced frustration is the energy required to form this domain wall. Accounting for the formation of a domain wall he predicted that the exchange bias shift would have the form

$$H_{\text{EB}} = \frac{2}{M_S t_{\text{FM}}} \sqrt{\frac{J_{\text{AF}} K_{\text{AF}}}{a}}, \quad (2.12)$$

where t_{FM} is the ferromagnetic layer thickness, M_S is the saturation magnetization, J_{AF} is the antiferromagnetic exchange constant, K_{AF} is the bulk anisotropy constant for the antiferromagnetic layer, and a is the lattice parameter. One thing to note about Eq. (2.12)

is the dependence of H_{EB} on inverse FM thickness. This general inverse FM thickness dependence of the loop shift has been seen in all exchange-biased systems.

Malozemoff also predicted that for uncompensated AF interfaces, the introduction of roughness at the interface leads to a similar form of the loop shift as in Eq. (2.12). The roughness would lead to a random field at the interface for the FM layer to couple to during cooling. The modification to Eq. (2.12) is

$$H_{\text{EB}} = \frac{2z}{\pi^2 M_S t_{\text{FM}}} \sqrt{\frac{J_{\text{AF}} K_{\text{AF}}}{a}}, \quad (2.13)$$

where z is the number of defects per unit area at the interface. Equation (2.13) depends on the defect concentration, which varies significantly between systems and methods of preparation. Although this contribution of roughness at the interface was largely ignored, his contributions of the planar domain wall and Eq. (2.12) is still used in experiments today [50]. We will test the inverse thickness law in Eq. (2.12) in Chapter 6.

2.4.3 Spin Flop Models

In 1997 Koon proposed a model which includes a fully compensated AF interface [31]. He was trying to explain some curious experimental results on the AF/FM system FeF_2/Fe where the largest H_{EB} shifts were found for fully compensated AF interfaces and the introduction of defects reduced the exchange bias [33]. The most curious effect, however, is that for special circumstances the induced exchange bias was positive—that is the loop shift was in the *same* direction of the applied field [3, 33].

Koon's model proposed that the frustration of the AF layers near the interface caused the AF spins to “cant” slightly from their anti-parallel state, allowing for small magnetic moments at the interface to form which were perpendicular to the AF spins, causing a 90° coupling between the AF spins and FM spins, dubbed the “spin-flop” coupling. A simplified version of the spin-flop coupling is shown in Fig. 2.6 (c). The argument for the spin-flop being that, for compensated interfaces, the collinear coupling and spin-flop

coupling require the same energy. This can be seen in Fig. 2.6 where the collinear (b) and spin-flop (c) modes are shown. In the collinear mode, half of the interface interactions are fully frustrated (the spins across the interface are anti-aligned), but in (c) all of the interface interactions are half-frustrated, because of their 90° spin-flop.

The actual picture according to the model is slightly more complicated than what is shown in Fig. 2.6 (c) because even with the spin-flop coupling the transition from the AF to the FM is not smooth. Koon suggested that the AF layers close to the interface started to rotate towards the FM. This meant that the AF spins close to the interface (3-4 monolayers) begin to rotate slightly forming a spiral in the magnetization that lead to a magnetic moment for which the FM can couple.

As much as Koon's model helped by suggesting the magnetization spiral as a method for coupling, Shulthess and Bulter in 1998 [51] showed that his model by itself could not explain the exchange bias shift, only the coercivity enhancement. Koon's model also suffered from the drawback that it required a body centered tetragonal structure, and it was not expandable to systems with other structures such as face centered cubic (fcc) or body centered cubic (bcc).

2.4.4 Stiles and McMichael and the Effect of AF Grains

Stiles and McMichael recently produced three papers to model the exchange bias [27], coercivity [38] and temperature dependence [52] of AF/FM systems. Instead of trying to visualize the AF/FM interface, they instead proposed that the polycrystalline system contained AF grains oriented randomly. This more realistically represents experimental conditions (or actual sample structure). Based on the work of Koon [31], they considered spin-flop coupling as well as the traditional collinear coupling between the AF and FM. They also included the idea from Malozemoff [26] of a partial domain wall in the AF that is parallel to the interface.

To explain the results from rotational hysteresis measurements, they suggested [27] that there were two types of AF grains in the system, non-rotatable or “frozen-in” grains and rotatable grains which, through the exchange bias interaction, rotated its magnetization to track the FM. The non-rotatable grains are responsible for the exchange bias loop shift, and the rotatable grains are responsible for the coercivity enhancement and the rotational hysteresis measurements.

Because an AF can be treated as two FM sub-lattices anti-aligned, the two ground states of an uncoupled AF are degenerate. This may be seen by reversing the directions of the magnetization 180° in each sub-lattice such that it is pointing in the opposite direction, and the same energy is achieved. By pinning the sample in an applied field, this degeneracy is removed and one of the states is preferred over the other.

These rotatable grains would irreversibly switch from one state to the other if the grain rotates through a postulated critical angle α_{crit} . After the grain rotates past this critical angle, it flips its magnetization such that the AF layer is pointed oppositely. This is schematically shown in Figure 2.7 where the AF spins are shown for the two AF configurations.

The term “irreversibly” is used because it is not guaranteed that a re-application of a magnetic field in the opposite direction will cause the grain to flip back to the other magnetization state. This depends on the critical angle.

This model has good agreement with experiments [53, 54] and is able to model the rotational hysteresis measurements, exchange bias loop shift, and coercivity with reasonable values. Their results show, similar to Shulthess and Bulter [51], that Koon’s spin-flop coupling term does not contribute to the loop shift at all.

Unlike other models based on a single crystal material, this model is based on polycrystalline films, which are cheaper to manufacture and therefore the predominant film used in technological applications today. Although Stiles and McMichael are able to achieve reasonable agreement with contemporary and historic experiments, their model

suffers from the fact that they have suggested a critical angle, but have not provided a way to measure or quantify this angle. Some [55] have attempted to measure the critical angle but find values inconsistent with this model. This model will be used to explain the experimental results in Chapter 8.

2.5 Materials Used in Exchange Biasing

Because of the wealth of literature in the field of exchange-biased systems, we are focusing on the systems that are being used in this Dissertation, IrMn/Co and FeMn/Co. The AF systems were chosen because of their popularity in technological devices such as hard disk drives and magnetic sensors. The Co FM system is generally used because of its high Curie temperature which makes it robust in magnetic devices.

2.5.1 Antiferromagnets: Iridium Manganese and Iron Manganese

Because IrMn and FeMn are the AF systems that are used in this Dissertation, the details and experimental results reported by others in the literature will be discussed. These two systems are metallic and are formed from transition d-band metal elements.

Generally FeMn forms a disordered fcc structure [56, 57, 58], but it can be influenced by the layers underneath it, known as buffer layers. Most experiments grow Cu underneath to promote fcc growth because copper forms a fcc structure and the layers grown above the Cu tend to take on the structural characteristics of the Cu layer.

FeMn has been shown to have a partial domain wall, or spiraling spin structure, when sandwiched between two FM layers [57]. This confirms some of the ideas of Malozemoff (Sec. 2.4.2) and Stiles and McMichael (Sec. 2.4.4). It has also been found that the Fe in FeMn forms an uncompensated surface at the interface that plays a crucial role in the exchange biasing [59]. The same authors could not validate the ‘spin-flop’ coupling of

Koon (Sec. 2.4.3).

The blocking temperature in FeMn varies according to the grain size, but the range is between 330–440 K with a grain size between 1.8–5 nm [60]. Larger grain sized samples will have a larger blocking temperature. The bulk Néel temperature is 500 K [61].

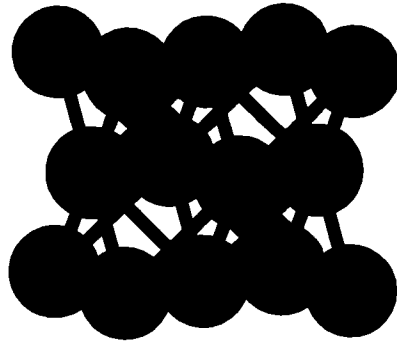


FIG. 2.8: The CuAu ($L1_0$) structure of IrMn. It is a modified fcc structure, with tetragonal distortion.

The IrMn system is fcc with a CuAu ($L1_0$) structure [62]. A sketch of the structure is shown in Figure 2.8. The consensus on grain size for IrMn is about 6–11 nm [63, 64, 65]. The increase in grain size increases the exchange biasing field H_{EB} [63, 66], with a Cu buffer layer providing the largest H_{EB} [63, 67]. Results in the literature have shown that 5 nm buffer layers of Ta or Zr have nearly no effect on the H_{EB} field when NiFe/IrMn is grown on top, but Cu and Ag buffer layers lead to large H_{EB} shifts [63]. This has been attributed to the small grains that the Ta and Zr systems promote, which lead to small IrMn grains and a low blocking temperature.

IrMn has been found to be (111) textured [68, 42, 69, 67]. This (111) texture plays an important role in the exchange biasing and thermal stability, as the removal of the texture (via changing the buffer layer) decreases the blocking temperature and exchange biasing [65].

2.5.2 Ferromagnet: Cobalt

Co is a material commonly used in spin valves. At first glance, one may expect the dependence of the exchange bias field on Co thickness to be complicated, given the structural properties and magnetic interactions which can affect the nature of the exchange biasing [59, 70, 71, 72, 73, 50]. For example, studies have shown that the deposition of Co on NiO induces FM ordering of NiO in the NiO/Co AF/FM system, leading to the conclusion that models of exchange biasing must consider the spin structure at the interface [74]. Anisotropic magneto-resistance measurements have suggested that a twist in the magnetization of the Co occurs for the CoO/Co system [75]. This twist in the FM is similar to the partial domain wall depicted in Fig. 2.7 for AF layers. Studies have shown that Co has thickness-dependent magnetic properties, giving in-plane to out-of-plane transitions [76]. For example, Co/Pt layers exhibit perpendicular (out of plane) anisotropy, but this tends to in-plane magnetization after 15 monolayers [77]. In addition to the thickness-dependent magnetic properties, Co also has a thickness-dependent structural transition from fcc to hcp structure at around 5 nm [78]. The grain size for Co is 10 nm [54], and the domain size is on the order of 1–4 μm [23, 79].

2.5.3 AF/FM Systems: FeMn/Co and IrMn/Co

Since significant variation in EB systems exists, it is important to also consider the AF/FM systems as a whole rather than their individual parts. The body of research here is limited somewhat because there is variation in the types of AF/FM systems that are currently being implemented in devices, of which FeMn/Co and IrMn/Co are two.

Previous studies of FeMn/Co have shown that chemical intermixing can occur at the FeMn and Co interface, forming FeMnCo₂ [73], as well as a 45° coupling between the spins in the AF and FM domains in single crystalline FeMn/Co [72], similar to the 90° coupling model suggested by Koon (Sec. 2.4.3). Experiments have discovered that with

FeMn, when in contact with a Co layer, both the Fe and Mn develop magnetic moments at the interface [61]. This does not happen for FeMn on Cu, a nonmagnetic element. Other studies have shown that the interface of FeMn and Co have aligned spin structures [59], discounting the spin-flop model of Koon introduced in Sec. 2.4.3.

Other work shows that IrMn has a weak magnetic moment at the IrMn/Co interface [80]. This is explained by uncompensated spins at the interface [81]. Of these uncompensated spins, a small amount (4 percent) are “frozen-in” and do not rotate with the magnetization. These are postulated by the Stiles and McMichael model of rotatable and non-rotatable AF grains in Sec. 2.4.4 Magnetic-optical indicator film (MOIF) images of IrMn/Co top spin valves have shown that the Co magnetization breaks up into microdomains during magnetization reversal, unlike IrMn/NiFe where the reversal is via large domain walls [82].

The concepts from this Chapter will be used in Chapters 6, 7, and 8 to explain the results of our static and dynamic measurements on these exchange-biased metallic systems. The interpretation of the results from upcoming chapters will rely on the models of exchange biasing from this Chapter.

CHAPTER 3

Magneto-Optical Kerr Effect

This chapter introduces the coupling of polarized light with magnetic material via the magneto-optical Kerr effect (MOKE). MOKE is the main experimental tool used in this thesis work for measuring the magnetization of different materials and will be discussed thoroughly.

MOKE is a powerful tool for studying magnetic materials, since it has mono-layer sensitivity and allows for selective probing of small regions on the surface of the sample. For metallic films, MOKE has a depth resolution of ~ 20 nm that is determined by the penetration depth.

MOKE is the phenomenon in which linearly polarized light incident on a magnetic material experiences a change in ellipticity and rotation. Conceptually, the Kerr rotation can be explained by considering that linearly polarized light contains equal amounts of right circularly polarized (rcp) and left circularly polarized (lcp) light. In some materials, the refractive indices will respond differently to the rcp and lcp light, leading to the reflected rcp and lcp light having different amplitudes and phases. This leads to a rotation of the linear polarization of the light if the phases differ, and an ellipticity if the amplitudes differ. If the amplitude and polarization respond differently, then both effects will

be present leading to a rotated and elliptical reflected beam [83]. A sketch of the Kerr rotation and ellipticity

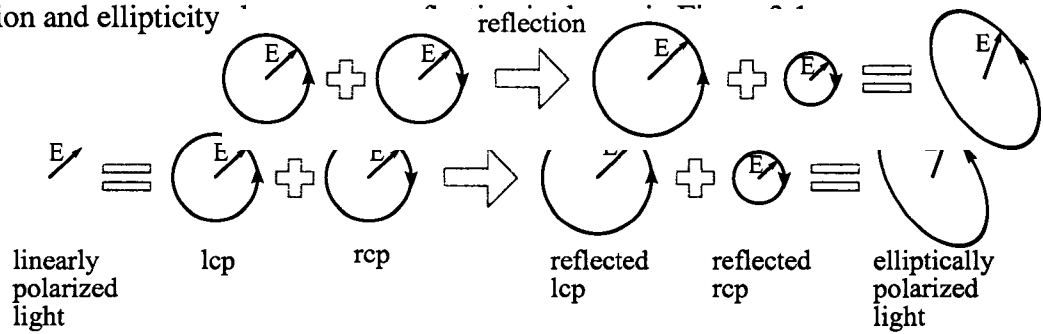


FIG. 3.1: Interpretation of the Kerr rotation using rcp and lcp light. The linearly polarized light can be written as a sum of rcp and lcp light. Upon reflection from a magnetic medium, the rcp and lcp light have different phases and amplitudes, leading to a rotation and a ellipticity.

The magneto-optical Kerr effect is what we use to measure changes in the magnetization of our magnetic system. It is an all-optical technique that arises from a quantum mechanical interaction of polarized light with the magnetic electrons in the sample. The following discussion follows the paper by Florczak and Dahlberg [84].

Microscopically, MOKE is due to the interaction of the oscillating electromagnetic wave with the electrons in the lattice. The conductivity tensor is modified to include off-diagonal components representing the magnetic contributions [85, 86, 87]. Most modern phenomenological interpretations then relate the conductivity and dielectric tensors, and then represent the magneto-optic quantities using the dielectric tensor.

3.1 MOKE Phenomenology

The magneto-optical effects are best described phenomenologically by using the dielectric tensor which depends on the magnetization of the material

$$\epsilon = \begin{pmatrix} \epsilon_{xx} & \epsilon_{xy} & \epsilon_{xz} \\ \epsilon_{yx} & \epsilon_{yy} & \epsilon_{yz} \\ \epsilon_{zx} & \epsilon_{zy} & \epsilon_{zz} \end{pmatrix}. \quad (3.1)$$

If a given material is isotropic (as in polycrystalline samples), then the diagonal components are equal. If the magnetization is along the \hat{z} axis, polarized light will couple to the \hat{x} and \hat{y} components, giving

$$\epsilon = \begin{pmatrix} \epsilon & -i\epsilon' & 0 \\ i\epsilon' & \epsilon & 0 \\ 0 & 0 & \epsilon \end{pmatrix}. \quad (3.2)$$

Typically ϵ and ϵ' are wavelength-dependent, but the small bandwidth of the laser we are using experimentally allows us to consider them independent of wavelength. In optically transparent materials, ϵ is taken to be real and ϵ' is taken to be imaginary. The general case assumes both ϵ and ϵ' to be complex, and is considered here. For paramagnetic and diamagnetic materials, ϵ' is proportional to the applied field H_A . However, for ferromagnetic materials ϵ' is proportional to the magnetization via the Voigt magneto-optical parameter Q [88, 89]

$$\epsilon' = \epsilon Q, \quad (3.3)$$

which simplifies Eq. (3.2) to simple off diagonal terms that depend on Q . Note that when the magnetization is zero $Q = 0$ and dielectric tensor reduces to a single, constant value.

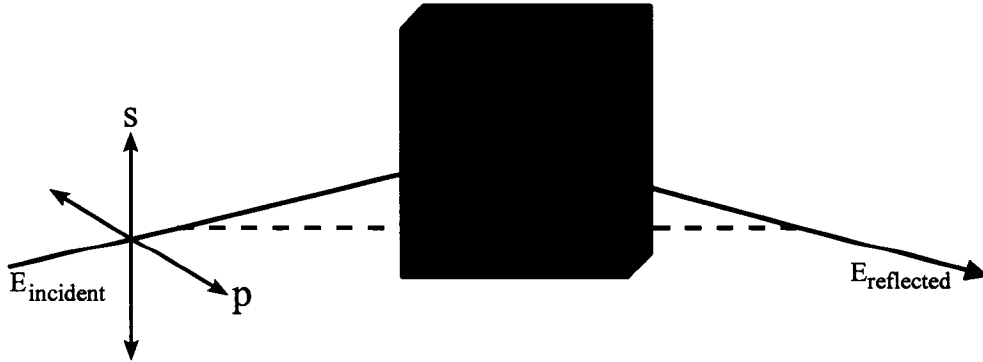


FIG. 3.2: Geometry for a magneto-optical Kerr effect experiment. The sample (blue) is assumed to have a mix of transverse M_T and longitudinal M_L magnetizations. The incoming light is a mix of s and p -polarizations.

Figure 3.2 shows a geometry for a typical MOKE experiment. The magnetization is assumed to be in the plane of the sample with two components, a longitudinal component M_L parallel to the optical plane and a transverse component M_T perpendicular to the optical plane. The optical plane is defined as the plane created by the incident and reflected rays (see Fig. 3.2).

3.2 Fresnel Reflection Coefficients

The Kerr rotation can be described by using the Fresnel reflection coefficients. Suppose we have an incoming optical beam of polarized light in an arbitrary direction, as illustrated in Fig. 3.2. The incoming light is a combination of s and p -polarizations written as

$$\mathbf{E}_{\text{inc}} = E_0 \cos \theta_i \hat{p} + E_0 \sin \theta_i \hat{s}, \quad (3.4)$$

where E_0 is the incident intensity and θ_i is the incoming polarization angle with respect to the optical plane. The reflection of this incoming light beam can be described by a general scattering matrix S^{gen} , where

$$\mathbf{E}_{\text{ref}} = S^{\text{gen}} \mathbf{E}_{\text{inc}}. \quad (3.5)$$

The matrix S^{gen} is a sum of the transverse and longitudinal components

$$S^{\text{gen}} = m_t^2 S^t + m_l^2 S^l. \quad (3.6)$$

Here, $m_t = M_T/M_S$ and $m_l = M_L/M_S$ are the magnetization in the transverse and longitudinal directions normalized by a total saturation magnetization M_S .

The two scattering matrices S^t and S^l are made up of individual Fresnel reflection coefficients. The matrices are

$$S^t = \begin{pmatrix} r_{pp}^t & r_{ps}^t \\ r_{sp}^t & r_{ss}^t \end{pmatrix} \quad S^l = \begin{pmatrix} r_{pp}^l & r_{ps}^l \\ r_{sp}^l & r_{ss}^l \end{pmatrix}, \quad (3.7)$$

where the r quantities are reflection coefficients. For example, r_{sp}^t is an expression for how much the transverse magnetization will rotate an incoming p -polarized wave into the outgoing s -polarized direction. This is a little counterintuitive that the index of the incoming wave comes after the index for the outgoing wave, but unfortunately it is standard notation for the community. For the transverse mode

$$r_{pp}^t = \left(\frac{n\beta - \beta'}{n\beta + \beta'} \right) \left(1 + \frac{(in^2Q/m_t) \sin 2\theta}{n^2(n^2\beta^2 - 1) + \sin^2 \theta} \right) \quad (3.8)$$

$$r_{ss}^t = \frac{\beta - n\beta'}{\beta + n\beta'} \quad (3.9)$$

$$r_{ps}^t = r_{sp}^t = 0, \quad (3.10)$$

and for the longitudinal mode

$$r_{pp}^l = \frac{n\beta - \beta'}{n\beta + \beta'} \quad (3.11)$$

$$r_{ss}^l = \frac{\beta - n\beta'}{\beta + n\beta'} \quad (3.12)$$

$$r_{ps}^l = -r_{sp}^l = \frac{\beta(in^2Q/m_l) \sin \theta}{n^2\beta'(n\beta + \beta')(\beta + n\beta')}, \quad (3.13)$$

where n is the index of refraction, $\beta = \cos \theta$, $\beta' = \sqrt{1 - (\sin^2 \theta)/n^2}$, θ is the angle of incidence measured from the sample normal the optical plane, and Q is the Voigt magneto-optical parameter. This parameter holds all of the quantum mechanics in the problem including the interaction of the light with the magnetization in the ferromagnet. Typically small, Q is proportional to the magnetization of the ferromagnet. Previous work has shown that $Q \approx 4 \times 10^{-2}$ [89]. If $Q = 0$, the sample becomes non-magnetic and the off diagonal components of S^l are zero, which recover the ordinary Fresnel reflection coefficients.

From Equation (3.8) the magnetic component for the transverse magnetization is contained in the r_{pp}^t , meaning that no transverse MOKE signal exists for s -polarized light and a change in only reflectivity for p -polarized light. This means that if one uses p -polarized light and cross polarizes the reflected light with a polarizer in the \hat{s} direction, then the transverse component can be effectively removed.

Most of the terms in the r coefficients depend on geometric quantities, particularly the angle of incidence. Figure 3.3 shows the geometric part of Eq. (3.13) versus the angle of incidence. It shows that the angle of incidence needs to be as large as possible, up to a maximum value of $\approx 65^\circ$ in order to maximize the longitudinal MOKE signal.

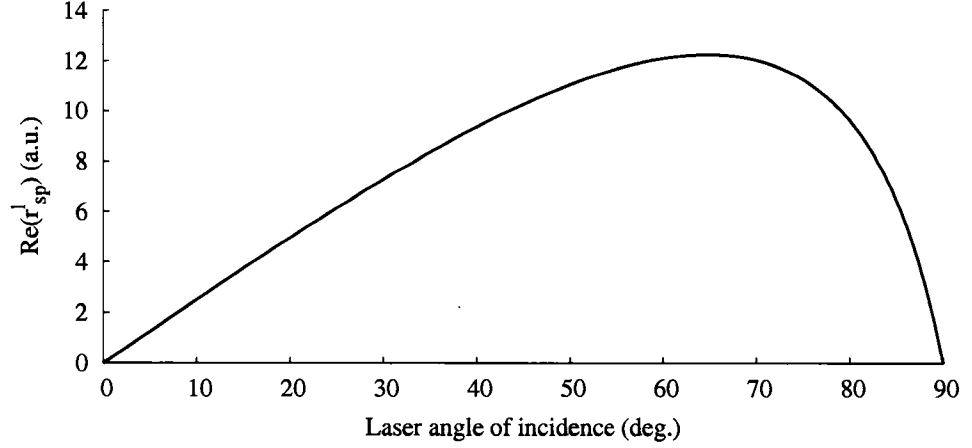


FIG. 3.3: Real part of the longitudinal Fresnel reflection coefficient versus angle of incidence of the reflected light for incoming p -polarized light. It is clear from the plot that a larger angle of incidence will lead to a larger Kerr rotation and MOKE signal in the detector. Shown here the optimal angle of incidence is approximately 65° .

Substituting Eq. (3.6) into Eq. (3.5) leads to a reflected field \mathbf{E}^{ref} of

$$\begin{aligned} \mathbf{E}^{\text{ref}} = & E_0 [(m_t^2 r_{pp}^t + m_t^2 r_{pp}^l) \cos \theta_i + m_t^2 r_{ps}^l \sin \theta_i] \hat{p} \\ & + E_0 [m_t^2 r_{sp}^l \cos \theta_i + r_{ss}^l \sin \theta_i] \hat{s}. \end{aligned} \quad (3.14)$$

In most experimental setups, one of these components can be eliminated by the use of a polarizer in either the \hat{s} or \hat{p} position. For example, if we set the incoming polarization to be in the optical plane ($\theta_i = 0$, p -polarization) and place another polarizer in front of the reflected beam at an angle θ_r from the optical plane, we get

$$\begin{aligned} \frac{I}{I_0} = \left| \frac{\mathbf{E}^{\text{ref}}}{E_0} \right|^2 = & |m_t^2 r_{pp}^l + m_t^2 r_{pp}^t|^2 \cos^2 \theta_r + |m_t^2 r_{ps}^l|^2 \sin^2 \theta_r \\ & - [(m_t^2 r_{pp}^l + m_t^2 r_{pp}^t) m_t^2 r_{ps}^{l*} + c.c.] \cos \theta_r \sin \theta_r. \end{aligned} \quad (3.15)$$

The term labeled *c.c.* is the complex conjugate. If we now rotate the polarizer to allow *s*-polarization only ($\theta_r \simeq 90$), we can further simplify Eq. (3.15). Term by term, the 1st term is small because of the $\cos^2 \theta_r$, the 2nd term is small because it contains terms of Q^2 where $Q \approx 10^{-2}$. The third term contains a term that is proportional to $m_l Q$, which will dominate this expression. Since it is proportional to m_l , the intensity of the light will be proportional to the longitudinal component of the magnetization. It is important to note that although the intensity of the light is proportional to the magnetization, the absolute value of the magnetization cannot be measured. At best, some experimental setups can measure the rotation and ellipticity of the reflected light, but this does not yield the absolute magnetization.

The Kerr effect enables the detection of the magnetization component in the plane by using two polarizers and laser light. This technique is powerful, and can be used to image magnetic domains [90] and obtain magnetic information in a very localized area since the amount of material probed is a function of the width of the laser beam. This locality of the Kerr effect will be used to probe the magnetization in a wedged sample, where the thickness of the material is a function of the length of the film in Chapter 6. The magneto-optical Kerr effect is the measurement technique used in all of the experimental chapters to probe the magnetization of the magnetic materials. Chapter 6 probes the response of the magnetization to an external applied field using the static Kerr effect to investigate the magnetic behavior. Chapter 7 uses a pump-probe experiment to investigate the ultrafast change of the Kerr signal as a function of applied field and pump-probe delay. Finally, Chapter 8 uses the Kerr effect in a pump-probe experiment and static experiment to show how the pump beam affects the magnetic materials.

CHAPTER 4

Ultrafast Magnetization Dynamics

This Chapter presents a theoretical discussion of magnetization dynamics, that is, how an ensemble of spins acts in time under a perturbation. When a group of spins or net magnetization is perturbed from an equilibrium position, the spins relax back to equilibrium in an oscillatory manner. These dynamics can be described phenomenologically using the Landau-Lifshitz-Gilbert (LLG) equation. Section 4.1 introduces the notion of spin waves as a consequence of a FM lattice in an excited state. Section 4.2 discusses magnetization motion under an externally applied field. Section 4.5 takes those results and further extends them to calculate the frequency of the magnetization motion. Section 4.3 introduces motion under damping with the LLG equation. Section 4.4 solves the LLG for weak damping and provides a method to extract frequencies from time-dependent data. The time-dependent data are acquired using the pump-probe MOKE technique described later in Sec. 5.4. This Chapter is based on the assumption that the pump laser provides only a momentary perturbation from equilibrium. The details of the pump laser effects will be discussed in Chapter 8.

4.1 Spin Waves

The idea of magnetic motion may be inferred from the Hamiltonian given in Eq. (2.1), where one can derive [25] ladder operators and ground energy states for the potential. For a given one-dimensional lattice with N sites and lattice spacing a , all of the spins are aligned in the ground state assuming a ferromagnetic interaction ($J_e > 0$). The first excited state has one spin anti-aligned with the other $N - 1$ spins aligned. This happens in any excited state, such as deviations from the 0 K temperature limit. The anti-aligned spin has an equal probability of being at each lattice site. Over a sufficiently long time, the anti-aligned spin will propagate through all the lattice sites. This is called a spin wave, and it is a characteristic of non-equilibrium FM lattices. The quasi-particle that carries the spin-wave is known as a magnon. An illustration of a spin wave propagating through a lattice is shown in Figure 4.1. Here the spin wave propagates through adjacent lattice sites. The FM interaction between lattice sites causes the propagation.

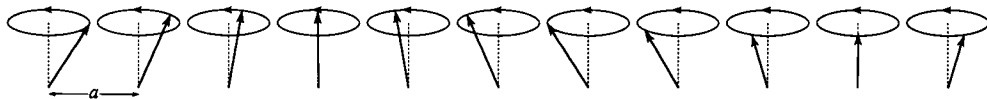


FIG. 4.1: Illustration of a spin wave propagating through the lattice with lattice spacing a . Shown here are 11 adjacent lattice sites. The arrow represents the direction of the magnetization through the lattice. From Ref. [25].

Detection and characterization of spin waves is accomplished using various methods. Inelastic neutron scattering can be used to excite and detect spin waves by measuring the energy loss in the neutrons as a function of wave vector [21]. Another way is to use Brillouin light scattering (BLS) which measures the energy loss of reflected light that has been absorbed by magnons [91]. Yet another way to excite and detect spin waves is via ferromagnetic resonance (FMR). FMR measures the absorption of microwaves as a function of applied field [92]. FMR will be discussed in more detail in Sec. 5.2.3.

4.2 Spin Dynamics—Magnetic Motion

A more formal approach to the discussion of spin dynamics is through the time-dependent Hamiltonian

$$i\hbar \frac{\partial \hat{S}_i}{\partial t} = [\hat{S}_i, \mathcal{H}], \quad (4.1)$$

where the Hamiltonian can be, for example, a spin-spin interaction Hamiltonian introduced in Chapter 2, Eq. (2.1). Alternatively, the dynamics can be discussed in terms of a net magnetization $\mathbf{M} = g\mu_B \hbar N \hat{S}_i$ where N is the number of spins aligned along the direction \hat{S}_i , μ_B is the Bohr magneton, and g is the spectroscopic splitting factor [93].

For a given system of magnetization \mathbf{M} in an applied field of \mathbf{H} the equation of motion is [94]

$$\frac{d\mathbf{M}}{dt} = -\gamma \mathbf{M} \times \mathbf{H}, \quad (4.2)$$

where γ is known as the gyromagnetic ratio given by

$$\gamma = \frac{g\mu_B}{\hbar} = \frac{g|e|\hbar}{2mc} = g\pi 2.79924916 \frac{\text{MHz}}{\text{Oe}}. \quad (4.3)$$

Equation (4.2) is a vector equation that defines the precession of the magnetization as a function of time. The constant g is known as spectroscopic splitting factor, which depends on the material. Typically $g \approx 2$ but it can be as large as 2.2 for materials such as cobalt and nickel [21].

In Eq. (4.2) the motion is assumed to be uniform, meaning that the magnetization behaves as a single domain particle. Phenomenologically, this equation describes the precession under an applied field providing a torque, shown in Figure 4.2.

4.3 Landau-Lifshitz and Gilbert Equation

In Eq. (4.2) the magnetization will precess in a plane perpendicular to \mathbf{H} . Here, precession would continue infinitely because Eq. (4.2) lacks damping terms. Phenomeno-

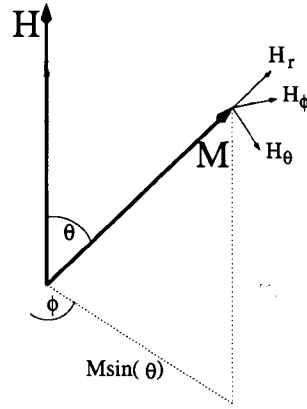


FIG. 4.2: Motion of an undamped magnetization \mathbf{M} in an applied field \mathbf{H} . The circle perpendicular to the external field \mathbf{H} traces out the precessional motion from $\mathbf{H} \times \mathbf{M}$. Also shown are the polar coordinates and the directions of the vectors of \mathbf{H}_{eff} resulting from the vector derivative in Eq. (4.13). Note \mathbf{H}_{eff} is not shown.

logically, Eq. (4.2) can be modified to include damping by introducing an effective \mathbf{H} (as in Eq. (4.10)) which has a time dependence on the magnetization [95, 96, 97]

$$\mathbf{H}_{\text{eff}} = \mathbf{H} - \eta \frac{d\mathbf{M}}{dt}. \quad (4.4)$$

Here η is the damping parameter, typically η is on the order of picoseconds. Substituting this into Eq. (4.10) gives

$$\frac{d\mathbf{M}}{dt} = -\gamma \mathbf{M} \times \left(\mathbf{H} - \eta \frac{d\mathbf{M}}{dt} \right). \quad (4.5)$$

Equation (4.5) is the Gilbert form of the Landau-Lifshitz (LL) equation. One can derive the Landau-Lifshitz form from Eq. (4.5) by recalling from Eq. (4.11) that $|\mathbf{M}| = M_S$ and taking $\mathbf{M} \times$ of both sides of Equation (4.5) and using cross product rules yields

$$\begin{aligned} \mathbf{M} \times \frac{d\mathbf{M}}{dt} &= -\gamma \mathbf{M} \times \mathbf{M} \times \left(\mathbf{H} - \eta \frac{d\mathbf{M}}{dt} \right) \\ &= -\gamma \mathbf{M} \times (\mathbf{M} \times \mathbf{H}) - |\mathbf{M}|^2 \gamma \eta \frac{d\mathbf{M}}{dt}. \end{aligned} \quad (4.6)$$

Combining Eq. (4.6) and Eq. (4.5) with some algebra leads to

$$\frac{1 + \alpha^2}{|\gamma|} \frac{d\mathbf{M}}{dt} = -(\mathbf{M} \times \mathbf{H}) - \frac{\alpha}{|M_S|} (\mathbf{M} \times (\mathbf{M} \times \mathbf{H})). \quad (4.7)$$

where $\alpha = \gamma\eta M_S$ is a redefined unit-less damping constant known as the Gilbert parameter. The value for α is on the order of 10^{-2} . This is the Landau-Lifshitz form of the Landau Lifshitz Gilbert (LLG) equation.

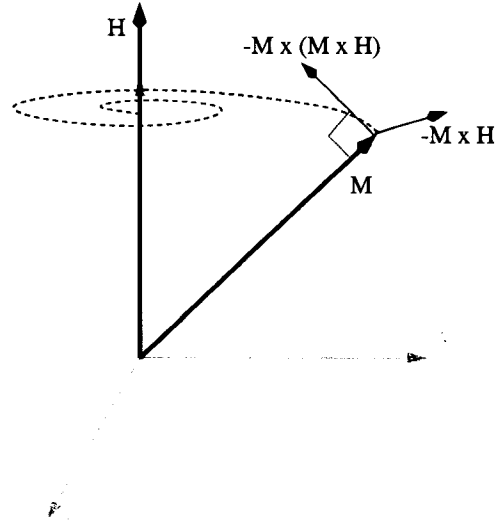


FIG. 4.3: Directions of the vectors and motion of the magnetism in the Landau Lifshitz Gilbert equation. \mathbf{H} is assumed to be in the \hat{z} direction, with \mathbf{M} at an angle determined by Eq. (4.15). Then $-\mathbf{M} \times \mathbf{H}$ precesses in a circular orbit about \mathbf{H} , and the direction of the damping term $-\mathbf{M} \times (\mathbf{M} \times \mathbf{H})$ is at a right angle with \mathbf{M} and always pointing towards \mathbf{H} , giving a $d\mathbf{M}/dt$ component towards \mathbf{H} . The dotted line is a trace of \mathbf{M} as it damps towards the applied field \mathbf{H} .

For this Dissertation Equation (4.7) will be used as the primary form for study of the magnetization dynamics. The terms of Eq. (4.7) are illustrated in Figure 4.3. If $\alpha = 0$, the undamped torque equation Eq. (4.2) is recovered. This is the precession component, where the direction of $d\mathbf{M}/dt$ is tangent to the circle perpendicular to \mathbf{H} , shown in Fig. 4.3. For nonzero values of α , a damping component of $d\mathbf{M}/dt$ is introduced that points towards the direction of \mathbf{H} . This implies that after a long time (where “long” is relative to the gyromagnetic ratio γ and damping constant α) \mathbf{M} will lie along \mathbf{H} because the damping term will pull it towards \mathbf{H} .

4.4 Approximate Solution to the LLG

Under the assumption of a small perturbation from equilibrium and small damping, the LLG can be reduced into a second-order differential equation in terms of the in-plane magnetization [98]. For these small oscillations, the time dependence of the in-plane magnetization angle can be described using a single-frequency sinusoidal given by [99]

$$\Phi(t) = \Phi_0 + \beta \exp(-t/\tau) \sin(\omega t + \varphi), \quad (4.8)$$

where $\Phi(t)$ describes the angle of the magnetization in the plane of the sample. This is the equation for an exponentially decaying sinusoidal, with oscillation frequency of ω and decay time of τ . The parameter β can be used as a measure of the amplitude of the oscillations. From this equation, the Gilbert damping parameter α can be extracted from the decay time τ [99]

$$\alpha = \frac{2}{4\pi M_S \gamma \tau}. \quad (4.9)$$

The Gilbert damping parameter depends on experimental constants such as M_S and γ , and it has an inverse relationship with the decay time constant τ . Figure 4.4 is a plot of Equation (4.8) for three different values of α .

4.5 Ferromagnetic Resonance

Assuming that the magnetization is only slightly perturbed from equilibrium and small damping, the dynamics can be describe by single frequency oscillations with a frequency that will be derived here. These results are commonly used to describe the resonant frequencies encountered in FMR experiments.

Landau and Lifshitz pointed out [95] that \mathbf{H} in Eq. (4.2) is better represented phenomenologically by an effective internal field \mathbf{H}_{eff} which, in addition to the externally applied field, contains other possible magnetization effects such as demagnetization fields

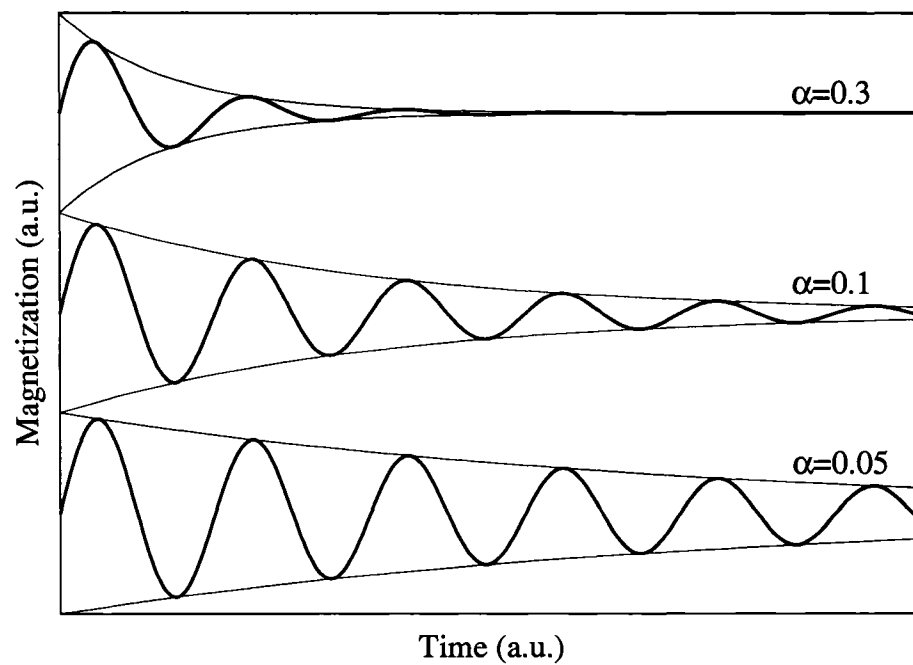


FIG. 4.4: Plot of the approximate solution to the LLG equation for different damping parameters α . The plots use Equation (4.8). As α increases, the damping of the oscillations increase. The envelope of the damping is also shown.

discussed in Sec. 2.1.1 or exchange bias fields discussed in Sec. 2.3. This replacement leads to a simple rewrite of Eq. (4.2) to

$$\frac{d\mathbf{M}}{dt} = -\gamma \mathbf{M} \times \mathbf{H}_{\text{eff}}. \quad (4.10)$$

The first thing to note from this is that by taking $(\mathbf{M} \cdot)$ to both sides of Equation (4.10) gives

$$\begin{aligned} \mathbf{M} \cdot \frac{d\mathbf{M}}{dt} &= -\gamma \mathbf{M} \cdot (\mathbf{M} \times \mathbf{H}_{\text{eff}}) \\ &= 0. \end{aligned} \quad (4.11)$$

This says that the magnitude of \mathbf{M} is constant. By convention, we set $|\mathbf{M}| = M_S$. By changing to spherical coordinates and using the fact that \mathbf{M} is constant, the solution to Eq. (4.10) is

$$\begin{aligned} \frac{d\theta}{dt} &= \gamma H_\phi \\ \frac{d\phi}{dt} &= -\frac{\gamma}{\sin \theta} H_\theta, \end{aligned} \quad (4.12)$$

where H_θ and H_ϕ are the vector components of \mathbf{H}_{eff} in the spherical $\hat{\theta}$ and $\hat{\phi}$ coordinates, respectively. Note that Eq. (4.12) does not have an equivalent for $\frac{dM}{dt}$ because $|\mathbf{M}|$ is constant.

In thermal equilibrium, the direction of the magnetization of the material \mathbf{M} is in the direction of the effective field on the material \mathbf{H}_{eff} . The internal free energy F of the system determines this effective field

$$\mathbf{H}_{\text{eff}} = -\frac{dF}{d\mathbf{M}}. \quad (4.13)$$

The derivative of the scalar F with respect to the vector \mathbf{M} is defined as the derivative of the individual components of the vector. This is somewhat trivial in Cartesian coordinates, but in spherical polar coordinates it is defined as

$$\frac{dF}{d\mathbf{M}} = (H_r, H_\theta, H_\phi) = \left(0, \frac{1}{M_S} \frac{\partial F}{\partial \theta}, \frac{1}{M_S \sin \theta} \frac{\partial F}{\partial \phi} \right), \quad (4.14)$$

where the \hat{r} component is zero since the length M is constant. Figure 4.2 shows the direction of the individual components of \mathbf{H}_{eff} with respect to the vector M . From there one can see that the $M_S \sin \theta$ term comes from an arc length along the direction of $\hat{\phi}$.

When the magnetization is in equilibrium, it is aligned with \mathbf{H}_{eff} and the free energy is at a minimum and the components H_θ and H_ϕ are zero. The angles θ and ϕ where this occurs satisfies

$$H_\theta = \frac{\partial F}{\partial \theta} = 0; H_\phi = \frac{\partial F}{\partial \phi} = 0. \quad (4.15)$$

To calculate the equilibrium direction of the magnetization one needs to solve Eq. (4.15) for equilibrium values θ_0 and ϕ_0 .

The time-dependent case is slightly different. Here the assumption is that there is a small change from the equilibrium angles that causes the magnetization to precess slightly, similar to a gyroscopic top. The polar coordinate angles become

$$\begin{aligned} \theta &= \theta_0 + \delta\theta \\ \phi &= \phi_0 + \delta\phi, \end{aligned} \quad (4.16)$$

where θ_0 and ϕ_0 are the equilibrium orientations calculated from Eq. (4.15).

First, Eq. (4.15) no longer holds and we must use Eq. (4.13) and Eq. (4.12) for the new equations of motion

$$\begin{aligned} \frac{d\theta}{dt} &= \gamma H_\phi = -\frac{\gamma}{M_S \sin \theta_0} \frac{\partial F}{\partial \phi} \\ \frac{d\phi}{dt} &= -\frac{\gamma}{\sin \theta_0} H_\theta = \frac{\gamma}{M_S \sin \theta_0} \frac{\partial F}{\partial \theta}, \end{aligned} \quad (4.17)$$

where the vector derivative in Eq. (4.14) has been used. F now needs to be approximated by using a Taylor series expansion about the equilibrium points found in θ_0 and ϕ_0

$$F = F_0 + \frac{1}{2} \left[\frac{\partial^2 F}{\partial \phi^2} (\delta\phi)^2 + 2 \frac{\partial^2 F}{\partial \theta \partial \phi} \delta\phi \delta\theta + \frac{\partial^2 F}{\partial \theta^2} (\delta\theta)^2 + O(\delta\theta)^3 + \dots \right], \quad (4.18)$$

where F_0 and all derivatives are evaluated at the equilibrium positions θ_0 and ϕ_0 .

Noting that the time derivative leads to periodic solutions,

$$\frac{d\theta}{dt} = i\omega\delta\theta; \frac{d\phi}{dt} = i\omega\delta\phi, \quad (4.19)$$

Eq. (4.18) and Eq. (4.19) can be substituted into Eq. (4.17) to give

$$\begin{aligned} -\frac{i\omega M_S}{\gamma} \sin\theta_0 \delta\theta &= \frac{\partial^2 F}{\partial\phi^2} \delta\phi + \frac{\partial^2 F}{\partial\theta\partial\phi} \delta\theta \\ \frac{i\omega M_S}{\gamma} \sin\theta_0 \delta\phi &= \frac{\partial^2 F}{\partial\theta\partial\phi} \delta\phi + \frac{\partial^2 F}{\partial\theta^2} \delta\theta. \end{aligned} \quad (4.20)$$

This is a set of coupled differential equations in $\delta\theta$ and $\delta\phi$. The solution is non-zero provided that the determinant is zero. This gives a solution for the frequency ω ,

$$\omega = \frac{\gamma}{M_S \sin\theta} \left\{ \frac{\partial^2 F}{\partial\theta^2} \frac{\partial^2 F}{\partial\phi^2} - \left(\frac{\partial^2 F}{\partial\theta\partial\phi} \right)^2 \right\}^{\frac{1}{2}}. \quad (4.21)$$

This is the equation for the resonance frequency of a ferromagnet as a function of the saturation magnetization M_S and free energy F . Equation (4.21) is the standard equation used for analysis in FMR experiments. One writes the free energy F in the system down and calculates the angular derivatives to obtain an expression for the precession frequency.

4.5.1 Free Energy Terms in FMR

The free energy term F introduced in Eq. (4.13) can have complicated behavior but its terms are essential to the determination of the magnetization equilibrium and ferromagnetic resonance frequencies, as seen in Sec. 4.5. The free energy must contain all of the magnetic contributions to the system.

In the analysis in this Dissertation, three free energy terms are included. The terms are written as

$$F = -H_{\text{EB}} M \cos(\phi_{\text{EB}} - \phi) \sin\theta - H_A M \cos\phi \sin\theta + 2\pi M^2 \cos^2\theta, \quad (4.22)$$

where the first term is the Zeeman interaction of the exchange bias field with the magnetization, the second term is the Zeeman interaction of the applied field with the magnetization, and the third term is the demagnetization factor. Here, H_{EB} is the exchange bias

field, H_A is the applied field, M is the magnetization, and θ and ϕ are the usual spherical coordinates. The negative sign in the first two terms implies that an energy minimum is reached when M aligns with H_{EB} and H_A .

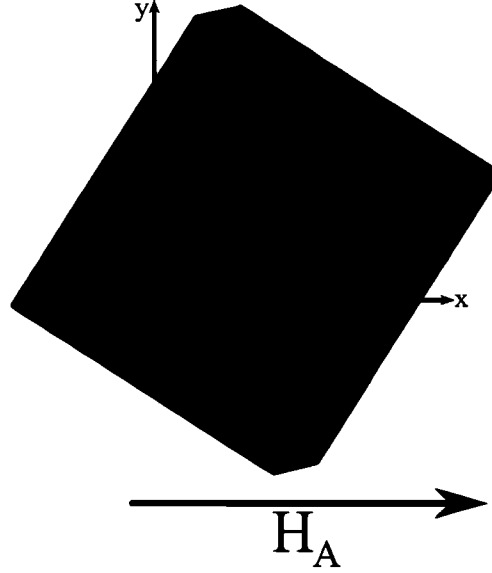


FIG. 4.5: Coordinates for description of the free energy terms. The film is shown in the \hat{x} - \hat{y} plane. The applied field is in the \hat{x} direction, with the exchange bias forming an angle ϕ_{EB} with the applied field direction. The demagnetization field (not shown) points in the \hat{z} direction, out of the plane of the sample.

Figure 4.5 shows the coordinate system and directions of the fields for describing this energy. Because of a large demagnetization field in these materials, M is treated as being nearly or completely in the plane of the sample giving $\theta \approx \pi/2$. This assumption is used in the evaluation of the derivatives in Eq. (4.21) to get an expression for the precession frequency

$$\left(\frac{\omega}{\gamma}\right)^2 = (H_A \cos(\phi) + H_{EB} \cos(\phi_{EB} - \phi) + H_D) \times (H_A \cos(\phi) + H_{EB} \cos(\phi_{EB} - \phi)), \quad (4.23)$$

where the relation $H_D = 4\pi M_S$ from Sec. 2.1.1 has been used. The angle ϕ will be determined by the equilibrium equation Eq. (4.15). Using Eq. (4.15), Eq. (4.22), and assuming that the magnetization is the plane of the film, the equation for the magnetization

direction is

$$\phi = \tan^{-1} \left(\frac{H_{\text{EB}} \sin \phi_{\text{EB}}}{H_{\text{EB}} \cos \phi_{\text{EB}} + H_{\text{A}}} \right). \quad (4.24)$$

This leaves five parameters that can be changed— H_{A} , H_{EB} , H_{D} , g -factor (hidden in γ) and ϕ_{EB} .

In summary, this Chapter introduced the dynamics of magnetic moments under the influence of an externally applied field. The dynamics are modeled using the LLG equation which is addressed for two cases—small damping and no damping. In the case of small damping, an expression for the damping parameter is derived. With no damping, the FMR equation is derived which describes the resonant frequency of a ferromagnet. The next chapter will introduce the exchange-biased samples that will be measured and how they are characterized. The static MOKE and pump-probe MOKE setups are also described.

CHAPTER 5

Samples and Experiments

This Chapter discusses growth of the magnetic samples that were used in the experimental measurements and the optical measurement techniques. In addition, various characterization techniques for the samples will also be discussed. Section 5.1 introduces the deposition process, Sec. 5.2 discusses the different techniques in characterizing the magnetic materials, specifically SQUID (Sec. 5.2.1), BH loopers (Sec. 5.2.2), and ferromagnetic resonance (Sec. 5.2.3). The last sections discuss the optical experiments, specifically the static magneto optical Kerr effect (MOKE, see Chapter 3) in Sec. 5.3 and the ultrafast pump-probe MOKE experiment in Sec. 5.4. The static and pump-probe MOKE experiments are used in Chapters 6, 7 and 8 to measure the magnetization of these samples.

5.1 Sample Growth

The samples used were grown by direct current magnetron sputtering. In basic DC sputtering, a cathode containing a target is held at a low potential with respect to an anode containing the substrate. Then ions are introduced into the sputtering chamber. These

ions (typically argon) are accelerated between the anode to the cathode and bombard the target. The material at the target is ejected and land on the anode, creating a thin film of material. The improvement to this method is the magnetron gun. The magnetron gun uses permanent magnets behind the target to create a magnetic field parallel to the surface of the target. This allows for electrons to be trapped just above the surface of the cathode and a more intense Ar ion bombardment. The enhancement of ion bombardment leads to faster deposition rates [100].

Since the introduction of alien materials will cause impurities in the films, deposition occurs in a vacuum chamber that has been pumped down to low pressures, typically on the order of 10^{-10} Torr. Once it has been pumped to this pressure Argon is added to the chamber to provide the ion bombardment. The Ar pressure is 2 mTorr during deposition.

The samples all have a generic structure of Si / buffer layers / AF / FM / capping layer. The buffer layers are metallic non-magnetic materials used to generate a favorable fcc crystal structure that continues to grow into the AF and FM layers. For this Dissertation the AF layers are restricted to two transition metal compounds, IrMn and FeMn. For the FM layer the transition metal cobalt is used. The capping layer in the structure is used to protect the rest of the material from oxidation from the atmosphere. The details of sample structure will be given in the following respective experimental chapters. Sample deposition for almost all of the samples was courtesy of Bill Egelhoff Jr., P. J. Chen, and Li Gan at the National Institute of Standards and Technology (NIST) in Gaithersburg, MD.

5.2 Sample Characterization

In this Dissertation additional techniques were used to characterize the samples. The SQUID, magnetic hysteresis measurements, and FMR measurements were carried out by collaborators at other institutions.

5.2.1 Superconducting Quantum Interference Device (SQUID)

The SQUID measurement uses a pair of Josephson junctions set in a ring of superconducting metal. When the ring is placed in a magnetic field, a current is generated in the ring and a phase difference is induced between the two Josephson junctions. If a bias voltage is applied on the ends of the ring, the current read from the superconducting ring is a function of the amount of flux lines passing through the ring, with a sensitivity of a single quanta of flux. The SQUID system gives a measurement of the magnetization in a given sample with unparalleled precision.

In this Dissertation, a Quantum Design SQUID Magnetometer was used to take magnetic hysteresis curves where the applied magnetic field was large—out of the range of the other experiments such as the B-H looper or MOKE. The superconducting magnet in the SQUID magnetometer allows for large applied fields in excess of 1 T (10 kOe). The measurements were carried out with support from Buzz Wincheski of the NASA Langley Research Center.

5.2.2 Magnetic Hysteresis Measurement

The absolute magnetization and hysteresis of a sample can be measured using a B-H Looper. The apparatus uses two sets of magnetic coils—a driving coil at a low AC frequency (typically 1–10 Hz) and a set of pickup coils to sense the change of the magnetization of the sample as a function of the driving AC field. This gives a hysteretic plot of the sample magnetization B versus applied field H [101]. These measurements were carried out by Bill Egelhoff Jr., P. J. Chen, and Li Gan at the National Institute for Standards and Technology (NIST).

5.2.3 Ferromagnetic Resonance

The ferromagnetic resonance experiment measures the response of a precessing magnetization by detecting the amount of microwave radiation that it absorbs as a function of applied field. Following the analysis from Sec. 4.5, there is a resonance frequency that is a function of the free energy in the system. The free energy terms (shown in Eq. (4.22)) include the exchange bias field H_{EB} , demagnetization field H_D , and saturation magnetization M_S .

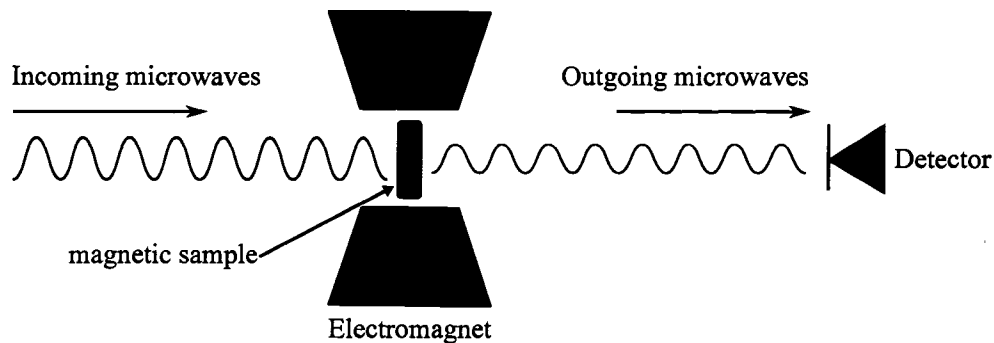


FIG. 5.1: Setup for a ferromagnetic resonance experiment. Incoming microwaves are absorbed depending if the resonance condition Eq. (4.21) is met. The detector senses the absorption as a function of applied field.

The experimental setup for FMR is shown in Fig. 5.1. A typical FMR experiment is set up as follows: the ferromagnetic sample is placed in a microwave cavity between the poles of an electromagnet. Microwaves are used in the experiment because the precession frequency of ferromagnetic materials is in the 3–30 GHz ($\lambda = 1\text{--}10$ cm) range. Typically it is easier to fix the frequency of the microwaves and sweep the field at a particular orientation to achieve the resonance condition than it is to fix the field and sweep the microwave frequency. A detector is placed at the end of the cavity to detect a change in the absorption of the microwaves. The field is swept until the resonance condition shown in Equation (4.23) is met. This causes an absorption of the microwaves and a drop in the intensity detected. The spectrum of the detector intensity as a function of field can be

used to fit Eq. (4.23) and quantities such as the Gilbert parameter α , H_{EB} , and H_{D} can be extracted. The FMR experiments in this Dissertation were carried out at NIST by Jim Rantschler.

5.3 Static MOKE

To measure the magnetization as a function of applied field, a static MOKE setup was built. The theory of MOKE was outlined in Chapter 3. The static MOKE setup uses polarized light incident on a sample placed in a magnet. The light is generated by a diode laser with a wavelength of ≈ 635 nm, modulated by a function generator. The modulated frequency varied, but was between 5–50 kHz. Our tests show that the Kerr signal is not affected by the modulation frequency. The incident light is polarized using a Glan-Taylor polarizer (Newport 10GL08), which has an extinction ratio of $10^5:1$. The beam is directed onto a magnetic sample placed between the poles of an electromagnet (GMW 3470). The poles of the electromagnet are placed far enough apart to ensure a uniform field in the region where the sample is located. The reflected beam is directed back through a second Glan-Taylor polarizer oriented nearly 90° from the incident polarizer. The light is detected by a photodiode (typically a Thorlabs DET110, but the DET210 and DET410 have also been used). A sketch of the MOKE system is shown in Figure 5.2.

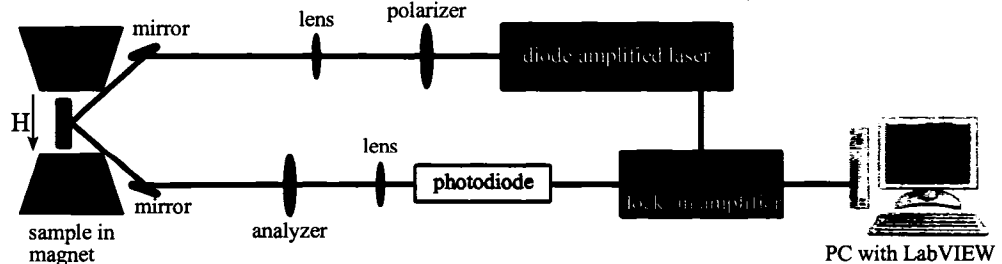


FIG. 5.2: Magneto-optical Kerr effect experimental setup. The setup uses the polarizer-analyzer scheme with a lock-in amplifier to increase the signal-to-noise ratio. Lenses are used to focus the beam onto the sample and the photodiode.

Although not necessary for general measurements, a pair of lenses were used—first to focus the light onto the sample and to focus the light onto the detector. Focusing onto the sample provides a smaller beam spot on the sample. The second lens is used to re-focus the cross-polarized light onto the photodiode to provide the detector with the maximum amount of light.

To facilitate a higher signal to noise ratio, a lock-in amplifier (SRS SR530) is used. The lock-in technique is designed to pick up signals in environments where the noise is large by modulating the signal periodically. Since the noise is random, it will not have the same periodic frequency as the signal, and will not make any contribution to the periodic signal [102].

Generally the complications in this setup are the alignment of the optics and the orientation of the polarizers relative to each other. If the angle between the two polarizers is larger than 2° , the amount of light propagating through the polarizers is too large and the change in the Kerr signal is too small to detect from the background.

The usual procedure for alignment is to adjust the polarizers such that a minimum signal is reached, indicating maximum extinction between the two polarizers, then rotating the analyzer approximately 0.5° off the minimum. Since the absolute magnetization cannot be determined by MOKE (discussed in Chapter 3), the angle that the analyzer is rotated does not matter as long as it is small enough that the Kerr signal does not disappear in the noise.

In addition to a diode laser, a sufficiently weak beam from an ultrafast laser can be used (see Sec. 5.4) by locking in on the repetition rate of the pulses in the laser instead of using a modulated beam.

5.4 Ultrafast Pump-probe MOKE

To extend the system shown in Sec. 5.3 for ultrafast measurements a ultrafast laser must be used. A pulsed Ti:Sapphire laser (Spectra-Physics Tsunami), which gives pulses ≈ 150 fs wide at 800 nm with a repetition rate of 80 MHz, is amplified with a regenerative amplifier (Spectra-Physics Spitfire), giving a final output pulse train of ≈ 150 fs wide and a 1 kHz repetition rate.

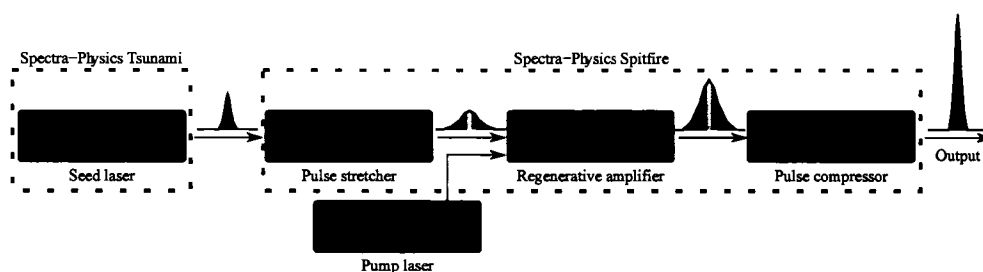


FIG. 5.3: Schematic of the amplified laser system. The seed beam is stretched in time, amplified, then compressed. The blue rectangles represent laser systems or laser components. A cartoon of the pulse characteristics is shown illustrating the stretching of the pulse, amplification, then compression of the pulse.

The regenerative amplifier uses a cavity with the Ti:S lasing medium placed inside the cavity. This allows for multiple passes through the medium and optimum amplification. Pockels cells are used to switch the pulses in and out of the cavity. The cavity is pumped with a Nd:YLF (Spectra-Physics Evolution-X) with a wavelength of 527 nm, a pulse width of 150 ns, and a repetition rate of 1 kHz. The energy gains are on the order of 10^6 . With a typical 150 fs pulse the gain medium (Ti:S) would break down due to the amount of energy in a short pulse. To avoid this the pulse is stretched in time using diffraction gratings such that the red components of the pulse travel ahead of the blue, amplified as mentioned above, then compressed in time to a short pulse. This minimizes damage to the gain medium and cavity optics during amplification. A schematic of the laser system is shown in Figure 5.3.

Figure 5.4 is a sketch of the pump-probe experiment. The amplified beam is split by

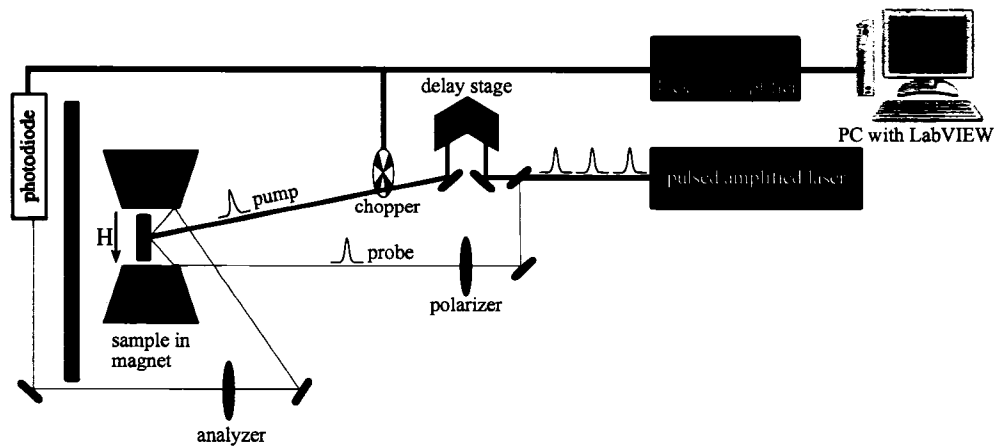


FIG. 5.4: Pump-probe MOKE setup. The pump beam is delayed relative to the probe via an optical delay stage. Both the pump and probe laser pulses are placed on the same point of the sample. Like the static MOKE, the probe uses a polarizer-analyzer scheme. The frequency from the optical chopper and signal from the photodiode are fed into the lock-in amplifier for detection

a beam-splitter for the pump and probe beams. The probe beam is delayed using a motion stage to arrive some time after the pump beam. The power of the pump beam is about 20–25 times the power of the probe beam. Both beams are directed onto the sample which sits in between the poles of a magnet. The applied field is in the plane of the sample. The angle of incidence of the probe beam with the sample is 45° . The angle between the applied field and the exchange bias axis of the sample, ϕ_{EB} can be rotated in any direction by placing the sample on a rotatable mount. The spot size of the pump was measured using standard techniques [103] and has a diameter of ~ 2 mm, which gives a fluence 0.61 mJ/cm² per pulse for the pump pulse for an average power of 20 mW. The probe beam detects the longitudinal (in the optical plane) component of the magnetization of the FM using a polarizer-analyzer scheme. The probe beam is polarized in the \hat{p} direction when incident on the sample and the analyzer is set to approximately $1\text{--}2^\circ$ crossed with the incident probe beam. The signal is detected by chopping the pump beam with an optical chopper and using lock-in techniques. The measurements are made at room temperature. In addition to time-resolved MOKE, static MOKE curves were measured by blocking the pump beam and locking in on the 1 kHz repetition rate of the probe beam. In the MOKE

measurements, the applied field is swept from negative saturation to positive saturation then back to negative saturation.

This Chapter provided details of the sample growth and the methods to characterize these samples via various experimental techniques. It also discussed the static MOKE and pump-probe MOKE experiments that are used in subsequent chapters. With the pump-probe MOKE, a brief summary of the amplified pulsed laser used in the experiment was also given. The next chapter will use the static MOKE experimental setup to explore the Co thickness dependence of exchange biasing and coercivity.

CHAPTER 6

Static MOKE on IrMn/Co and FeMn/Co

This chapter investigates the dependence of exchange bias strength on FM layer thickness for IrMn/Co and FeMn/Co bilayers. These materials are important for technological applications and are used in exchange-biased spin valves in computer hard disk sensors. Although these bilayers have been studied for applications, the dependence of the exchange bias interaction on Co layer thickness has not been thoroughly investigated.

Previous work on Co with a Cu buffer layer [78] showed that the structure of Co changed from face centered cubic (fcc) to hexagonal closed packed (hcp) as the thickness of the Co increased. For a 6 nm layer of Co grown on 9 nm of Cu, 40 percent of the Co was hcp and 60 percent was fcc. Since the wedges tested have the thickness where this fcc to hcp transition is expected, we will be able to explore the effect that the structural transition has on the exchange biasing and coercivity. Such a transition may induce a twist of the magnetization alignment in the Co.

Exchange-biased systems with a wedge in the FM were constructed to allow varying the exchange bias field strength by varying the FM thickness t_{FM} . Experiments were

carried out on IrMn/Co and FeMn/Co wedges where the Co thickness varied and also on single-thickness FeMn/Co films. The results show that on FeMn/Co for certain buffer layers, H_{EB} levels off indicating that the buffer layer plays a role in the strength of the exchange biasing [50]. For IrMn/Co, the exchange bias follows a monotonic increase with inverse thickness, as predicted by models [26]. For both wedges a single domain wall is observed in the Co as the field is varied. Rotational dependence of the exchange bias and coercivity on thick FeMn/Co samples shows that the system is well pinned, and that there is no twist in the Co magnetization as others have seen in Co systems [75].

6.1 Experimental Details

Experimentally, the setup from Sec. 5.3 is used to study the wedge samples with minimal modification. To study wedge samples, the sample holder is replaced with a sample holder that is attached to a vertical micrometer. The sample is then placed in the holder and the laser beam is moved to the edge such that it is reflecting off the end. The micrometer value is recorded. This value is used as a zero value, where the thickness of the FM anywhere else on the wedge will be determined by the amount that the micrometer has moved from this value and the thicknesses of each end of the wedge.

Because the wedges are long relative to the range of motion of the micrometer, the samples had to be rotated 180° once the full length of the micrometer stage had been reached. This means that, to scan the whole thickness range of the wedge, the data was taken in two separate runs.

MOKE curves were taken on wedged samples where the Co thickness was varied. The samples were grown using techniques outlined in Sec. 5.1. The films have a structure of Si / thermal oxide / Ta (5 nm) / Cu (5 nm) / FeMn or IrMn (10 nm) / Co (1–17 nm) / Al_2O_3 (1.2 nm) and are outlined in Figure 6.1 (a)–(b). In all of the samples, Al_2O_3 is formed from sputtered Al exposed to air and is used as a capping layer to prevent oxida-

tion. X-ray photoelectron spectroscopy shows no evidence of the formation of oxidized CoO. Pinning is achieved by heating the samples to 250°C and cooling in an external magnetic field of 100 Oe. The samples were pinned along the axis perpendicular to the thickness gradient.

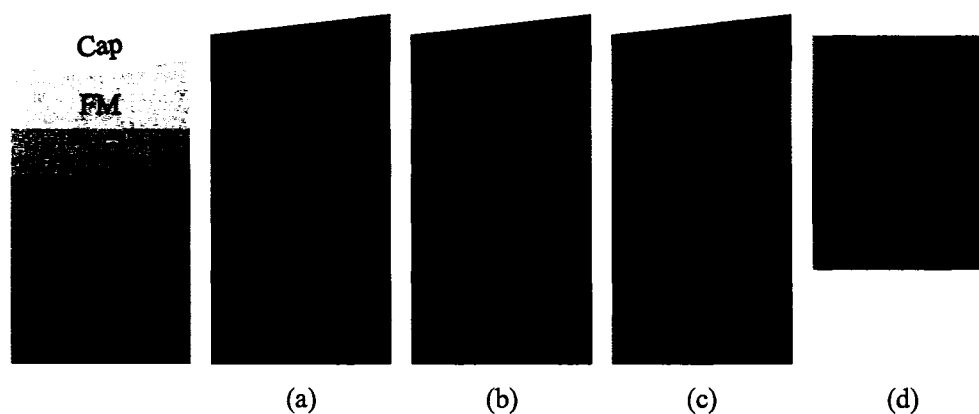


FIG. 6.1: Sketch of samples used in the MOKE experiments. The left shows the generic structure of the films. Samples (a)–(c) are wedged with the Co thickness varying. In samples (a) and (b) the buffer layers are the same (Ta/Cu) and are used in this section. Sample (c) has a slightly different buffer layer (W instead of Ta) than (c) and is used in Sec. 6.3.1. Finally, sample (d) is used to study the rotational dependence in Sec. 6.5. The samples in (a)–(c) were grown by Bill Egelhoff Jr., P. J. Chen, and Li Gan at NIST Gaithersburg. Samples in (d) were grown by Anne Reilly at Michigan State.

6.1.1 Errors and Uncertainties

A gaussmeter was used during MOKE measurements to measure the field. Corrections were made to compensate for the magnetic field gradient between the poles of the magnet, such that the magnetic field at the center of the magnet where the sample is located is different from the magnetic field towards the side where the gaussmeter was located. An estimated error from the extraction of the exchange bias field of 5 Oe. This is a rough upper-limit to the error in the field and the ability to extract the exchange bias from the hysteresis loops. This value is constant for all field values extracted, meaning it will be more significant at smaller fields than at larger fields.

The FM thickness was measured using a linear formula based on the measured length of the wedge and the reported thickness gradient. For the measurement of t_{FM} , the samples were on average 3 cm long (the precise length was measured with calipers) with a Co thickness gradient of 15 nm. The micrometer on the stage mount had a resolution of 0.1 mm, and the uncertainty in the measured Co thickness is estimated to be 0.05 nm. These errors have been used in the following figures, although they often do not show up because they are small.

6.2 MOKE curves

Figure 6.2 shows some sample MOKE curves taken using the experimental setup for a wedge discussed previously. Shown are MOKE curves from three wedges taken on the thick (purple, green, light blue) and thin (red, blue, orange) ends of the wedge. Since MOKE cannot measure the absolute magnetization, the y -axis is plotted using arbitrary units. The thickness given in the plots is the thickness of Co for the portion of the wedges where the laser was incident.

The coercivity H_C (half-width of the loop) and exchange bias H_{EB} (shift of the loop from zero) are extracted by centering the y -axis about zero, normalizing the y -axis to unity, and finding the switching field (point where the magnetization is zero) for both increasing and decreasing field. The half-difference between the two is H_C and the average of the two is H_{EB} .

By coincidence, this Figure also shows different noise levels of the MOKE signal, from large noise (a) to little noise (c). Although noise is a factor in the loops, it is straightforward to pick out H_{EB} and H_C from the loop if the loops are square, as shown in Fig. 6.2 (a). Additionally, the curvature of the loop makes picking out the loop shift difficult or ambiguous as shown in Fig. 6.2 (b). Since the loop in Fig. 6.2 (b) is not square, it is less clear where the exchange bias and coercive fields are located. Generally the noise occurs

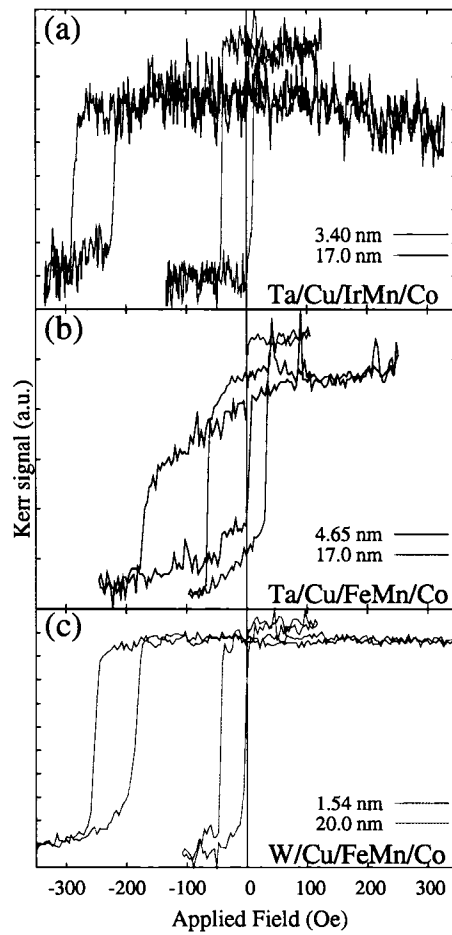


FIG. 6.2: Easy axis MOKE curves on wedged-Co samples. Three wedges are shown with (a) Ta/Cu/IrMn/(1–17 nm Co), (b) Ta/Cu/FeMn/(1–17 nm Co), and (c) W/Cu/FeMn/Co (1–20 nm Co) on the thick and thin sides of the wedge. As expected from Eq. (2.12), the thicker Co side has a smaller H_{EB} shift.

because maximum extinction is not achieved between the polarizer-analyzer pair. The polarizers perform best when they are oriented such that any reflections from the incident beam are retro-reflected. Although this was attempted, angles as much as 5° can cause problems. In the experimental setup, the extinction between the two polarizers can sometimes be increased by rotating one of them 180° . Why this is true is not clear; possibly due to the orientation of the crystals in the polarizers being better at one 180° orientation than another.

6.3 Co Thickness Dependence of H_{EB} and H_C

All of the wedges measured varied the ferromagnetic Co thickness t_{FM} . Figure 6.3 is a representative set of the $1/t_{FM}$ dependence of the exchange biasing (left) and coercivity (right) on a Ta/Cu/IrMn/Co wedge. $1/t_{FM}$ is plotted instead of t_{FM} because Malozemoff predicts an inverse- t_{FM} relationship with H_{EB} shown in Eq. (2.12). The equation used to fit the data are given by

$$H_{EB}, H_C = m(1/t_{FM}) + b. \quad (6.1)$$

One can see that for IrMn the exchange bias increases monotonically with inverse t_{FM} , as illustrated by the black line fit to the red squares. Fig. 6.3 also shows strong run-to-run coincidence in the extracted data as two runs shown are comparable to each other.

From the data, it appears that the IrMn/Co sample shows strong exchange biasing as evidenced by square loops, a $1/t_{FM}$ dependence of H_{EB} and independence of data from run to run.

The same experiment was conducted on a similarly constructed layer with FeMn as the AF. Figure 6.4 shows H_{EB} (left) and H_C (right) versus inverse- t_{FM} for a Ta/Cu/FeMn/Co wedge. The behavior in the plot is similar to Fig. 6.3; however, strong run-to-run variation

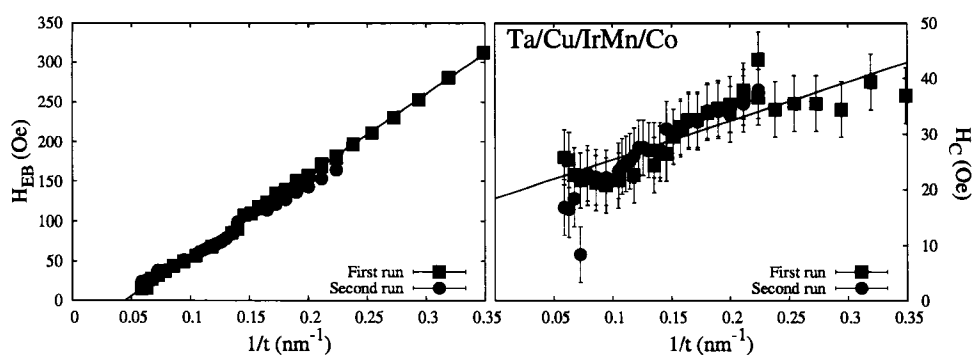


FIG. 6.3: H_{EB} and H_C as a function of inverse Co thickness for a IrMn/Co wedge sample. Two runs taken a few days apart. The first measurement (red squares) show a strong linear dependence of H_{EB} with inverse thickness and generally increasing H_C . A subsequent run (purple circles) shows similar behavior in the linear dependence, as the points align on top of each other. The black lines are linear fits to the first run.

in H_{EB} and H_C for FeMn/Co (two separate data runs are shown in the figure) is present. For this set, two single-thickness films were grown to compare with the wedge. These two films, with Co thicknesses of $t_{FM} = 3, 10$ nm, are shown in aqua triangles.

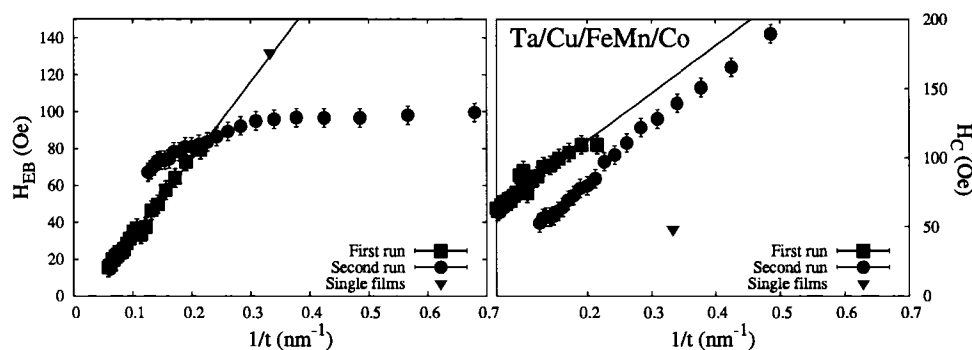


FIG. 6.4: H_{EB} and H_C as a function of inverse Co thickness for a FeMn/Co wedge sample with a Ta/Cu buffer layer. Two runs are shown taken on different days. The first measurement (blue squares) shows a linear dependence in both H_{EB} and H_C . A subsequent measurement (green circles) taken at a later time shows a leveling off of H_{EB} and an increase in H_C for the same given thickness. Also shown are two measurements taken on single-thickness films (aqua triangles), to compare with the wedge samples. The black lines are linear fits to the first run.

It appears that in the FeMn system, the buffer layers Ta/Cu seem to affect the exchange bias at small t_{FM} thicknesses. This will be explored more in Sec. 6.3.1. Since the MOKE curves for FeMn with Ta/Cu buffer layers shown in Fig. 6.2 (b) are more rounded

than the IrMn curves, this result in Fig. 6.4 is not unexpected. It is surprising that although H_{EB} shows leveling off with $1/t_{FM}$, the coercivity shows a strong increase through the Co thicknesses measured.

The measurement of the single-thickness films was repeated twelve times to ensure that the field cycling did not affect H_{EB} and H_C . This phenomenon, known as training [104, 105, 106], is well documented in the literature and is generally attributed to irreversible changes in the AF layer as the field is cycled. It manifests itself as varying H_{EB} and H_C field values, and can last as long as ten field cycles before stabilizing.

The single-thickness films overlap well with the fit from the first run in Fig. 6.4. The fit to the first run shown in black appears to also extend out to the 3 nm Co film measurement for H_{EB} . For H_C the 10 nm single-thickness Co film fits well with the first run, but the second 3 nm film shows a coercivity that is significantly less than the coercivity extracted from the second run.

For the FeMn/Co, H_{EB} shows a linear dependence on $1/t_{FM}$ for Co thickness greater than ≈ 5 nm with a strong run-to-run data variation. This may indicate that the pinning is not strong or there is a modification in the AF layer as the Co layer is flipped. Surprisingly for FeMn/Co, even though the behavior of H_{EB} shows leveling off, H_C shows a strong, smooth increase across all thicknesses.

It is tempting to attribute the second run data in Fig. 6.4 to training, since H_{EB} appears to be changing in a non-linear fashion as was seen in Fig. 6.3. It is unlikely that it is training, because the number of field cycles that the sample has been through at the time of this second run of data is on the order of 20. The monotonic increase of H_C in Fig. 6.4 further suggests that it is not training, since training effects affect H_C as much as H_{EB} [104].

Even though the Co thickness studied is in a range of expected deviations in Co structure, the only effect we see is a small bump in H_{EB} and H_C around 7 nm for IrMn/Co, and 10 nm for FeMn/Co (most obvious in Fig. 6.7). This may be related to the structure

change from fcc to hcp at 6 nm as discussed at the beginning of this Chapter [78].

6.3.1 FeMn: Effects of Buffer Layers on H_{EB} and H_C

Since the buffer layer was the suspected problem with the FeMn layers, a new set of films were grown with a different buffer layer using tungsten to replace the tantalum. A schematic of a wedge used is shown in Fig. 6.1 (c). Two Co wedges were grown with the new buffer layers, where Co was varied from 1–20 nm and from 15–35 nm variation. Figure 6.5 shows the exchange bias (left) and coercivity (right) of the thick (aqua circles) and thin (orange squares) wedges.

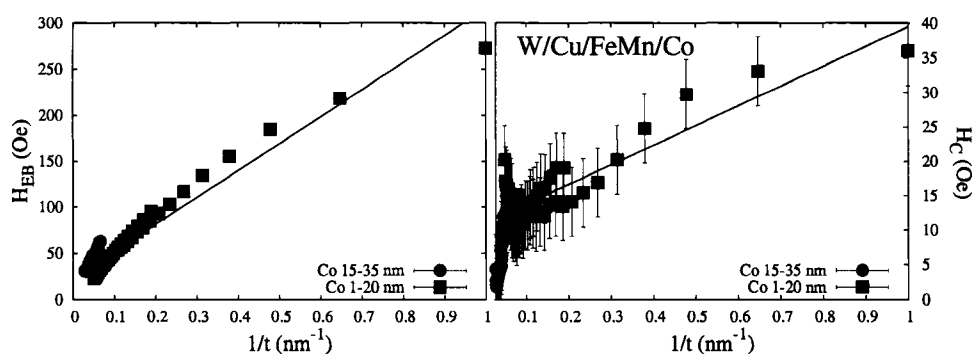


FIG. 6.5: Inverse thickness dependence of H_{EB} (left) and H_C (right) on FeMn/Co with a W/Cu buffer layer. This shows a set of two wedges with different Co thickness ranges, from 1–20 nm (aqua circles) and 15–35 nm (orange squares). The error bars are fixed at ± 5 Oe to compensate for the errors in reading the field. The black lines are linear fits to the thinner wedge.

Unlike Fig. 6.4, the thickness dependence of H_{EB} is much more linear, shown in the fits in black. Additionally, the MOKE loops shown in Fig. 6.2 (c) are square loops and have a well-defined switching field. The leveling off that was observed with the Ta/Cu/FeMn/Co is much less evident with the tungsten buffer layer. The shift between the two sets of data in the H_{EB} plot are not worrisome, because these are different samples. Small and uncontrollable variations in the growth processes restrict us from comparing the two.

6.3.2 Interface Exchange Energy

A common way to quantify the strength of the coupling in exchange-biased layers is to define a constant called the interface exchange energy, J_{EB} (sometimes called σ [107], or J_k [67]). For an ideal interface [17]

$$J_{\text{EB}} = M_S H_{\text{EB}} t_{\text{FM}}. \quad (6.2)$$

This is similar to a modified version of Eq. (2.12) by Malozemoff with all of the constants combined into J_{EB} .

From the inverse t_{FM} dependence of the exchange bias in Fig. 6.3, Fig. 6.4, and Fig. 6.5, the interface energy is calculated per-point using Eq. (6.2). Another method to calculate J_{EB} is to modify Eq. (6.2) such that

$$H_{\text{EB}} = \left(\frac{J_{\text{EB}}}{M_S} \right) \frac{1}{t_{\text{FM}}}, \quad (6.3)$$

and it is evident that the slope of a H_{EB} versus $1/t_{\text{FM}}$ plot reduced by the multiplicative factor of M_S leads to J_{EB} .

The values for the interface exchange energy were calculated per point using Eq. (6.2) and then via the slope from the $1/t_{\text{FM}}$ fits using Eq. (6.3) and it shown in Figure 6.6 for the three wedges. The error bars represent a standard propagation of error from the errors discussed in Sec. 6.1.1. The horizontal lines in each of the curves represent the interface exchange energy calculated from the slope. The values we extract are 0.145 erg/cm^2 for Fig. 6.3, 0.0592 erg/cm^2 for Fig. 6.4, and 0.0417 erg/cm^2 for Fig. 6.5.

The values from Fig. 6.6 compare favorably to the literature. For polycrystalline FeMn, values between $0.02 - 0.20 \text{ erg/cm}^2$ have been reported [2]. Specifically, studies on wedged FeMn/NiFe report a interface energy of 0.057 erg/cm^2 [56] and 0.2 erg/cm^2 was reported on epitaxial FeMn/Co [61]. Our values extracted from FeMn of 0.0592 erg/cm^2 and 0.0417 erg/cm^2 fall into the range reported.

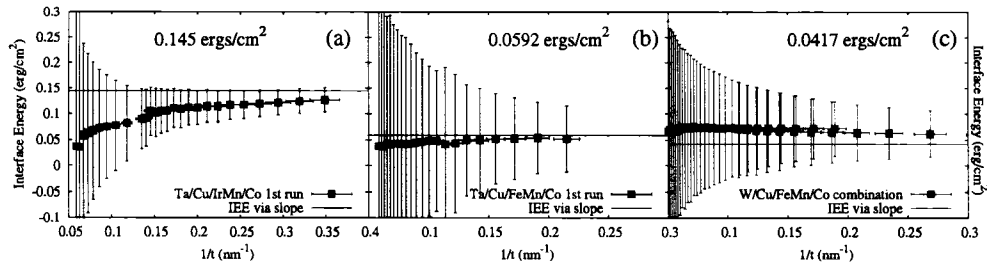


FIG. 6.6: Comparison of interfacial exchange energies for different wedge systems. Shown are the energies calculated per point using Eq. (6.2) from (a) Fig. 6.3, (b) Fig. 6.4, and (c) Fig. 6.5. The horizontal lines are the interface exchange energies calculated from the slopes extracted from the square points in the H_{EB} vs. $1/t_{FM}$ plots. The values for the lines extracted from the slopes are shown in each figure.

For IrMn, reported values range from 0.1 – 0.19 erg/cm² [2]. Studies on IrMn/CoFe report an interface energy of 0.192 erg/cm² [108]. Our value of 0.145 erg/cm² fits within the range of reported values.

6.4 Switching Field in a Wedge

An interesting artifact of wedge structures is that a single domain wall appears to sweep through the wedge as the field is increased. This is most obviously seen by looking at the switching field (the field where the magnetization is zero) in both sweeping up and down of the magnetic field.

Figure 6.7 shows the thickness of the Co wedge versus the switching field for IrMn/Co (squares) and FeMn/Co (circles). The arrows indicate the decreasing field (from $+M$ to $-M$), and increasing field (from $-M$ to $+M$). These plots indicate simplified domain structure in the wedges, similar to the effect seen in NiFe/FeMn bilayers, where motion of a single domain wall was seen [56, 109]. At an applied field of 0 Oe, all the spins are oriented in the same direction. As the field is decreased, the spins start to flip in the opposite direction. At -50 Oe, Co thicknesses on the wedge larger than 8 nm are spin flipped 180°. As the field increases to -275 Oe, all of the spins flip accordingly.

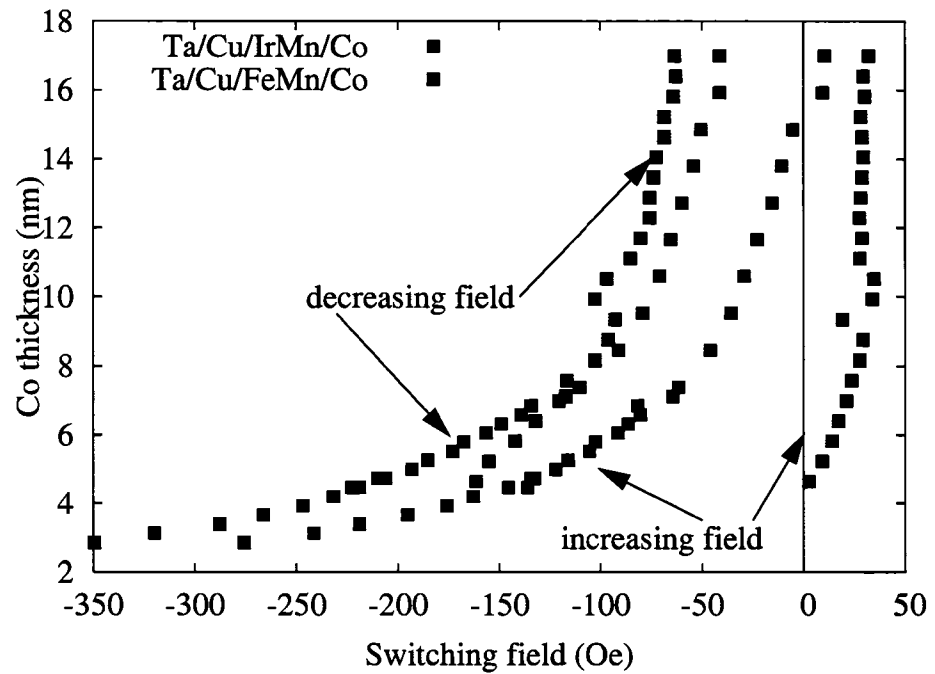


FIG. 6.7: Switching field ($H_{EB} \pm H_C$) as a function of thickness for two wedges of IrMn/Co and FeMn/Co. The sweeping motion of the fields here show that there is a domain wall in the wedge that is shifting as a function of field. The thicker Co side switches first because its exchange bias is smaller than the thin Co side.

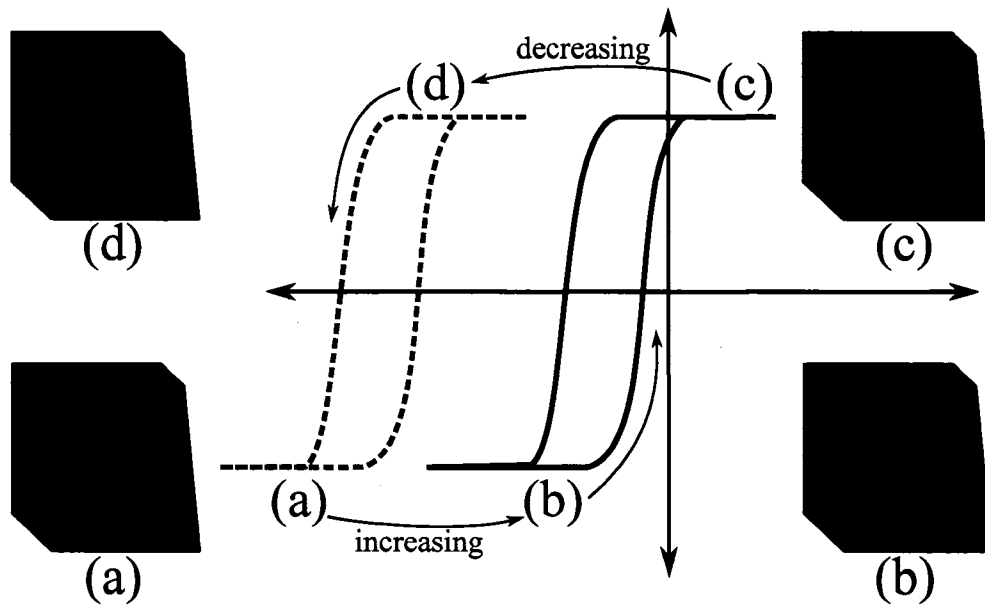


FIG. 6.8: Schematic of domain wall motion in a wedged Co sample. Two hysteresis loop schematics are shown taken on the thin (green dashed line) and thick (blue solid line) sides of the Co film. The FM configurations are shown along the outside with arrows indicating the FM direction. In (a), the magnetization is saturated and all of the FM moments are pointed toward the applied field. As the field is increased, shown in (b), most of the wedge has reversed directions but the thick side has not, leaving a domain wall depicted as a red line in (b). Configuration (c) is identical to (a) except the field and moments are reversed. In (d) most of the thick side of the wedge has reversed but the thin has not, leading to a domain wall in the wedge, shown in red.

The schematic of the domain wall switching is shown in Figure 6.8. In this figure, the magnetization in the Co wedge is depicted as the magnetic field is swept. Shown in the middle are two hysteresis loops taken on the thin (green, dashed) and thick (blue, solid) ends the wedge. When the field is at (a), the magnetization is in the direction of the applied field and all of the wedge is saturated. As the field is decreased in (b), the thin end of wedge has reversed but the thick end has not. The domain wall in (b) is shown as a red line on the FM film. At (c), the magnetization is aligned with the applied field. Once again, as the field is reversed in (d), the thick end has rotated but the thin end has not. The domain wall is shown as a red line.

6.5 Angular Dependence of H_{EB} and H_C on FeMn

To study the unusual behavior of FeMn further we constructed single-thickness films to examine the rotational dependence of the exchange biasing. The angular dependence of H_{EB} and H_C provide fruitful information about the pinning mechanism. A well-pinned system will show two peaks in H_{EB} and H_C , located when the H_{EB} axis is aligned with the applied field.

There were two films used in this set of experiments. The films were grown by Anne Reilly at Michigan State University. Their structures are shown in Fig. 6.1 (d) where Co thickness was 12 nm and 35 nm. Since there is no capping layer on the Co, presumably a CoO layer formed after being exposed to air. Although CoO is an antiferromagnet, it does not induce a second exchange-biased interface because its Néel temperature is 290 K [2], below room temperature where these experiments were conducted. The pinning axis was set by heating the samples ex-situ above the blocking temperature (~ 500 K) and cooling them in an applied field of ~ 30 Oe. The experiments were conducted using a modified experimental setup from Sec. 5.3 by adding rotation stage placed between the poles of the magnet. The stage has an angle sensitivity of 1° , and can be rotated 360° .

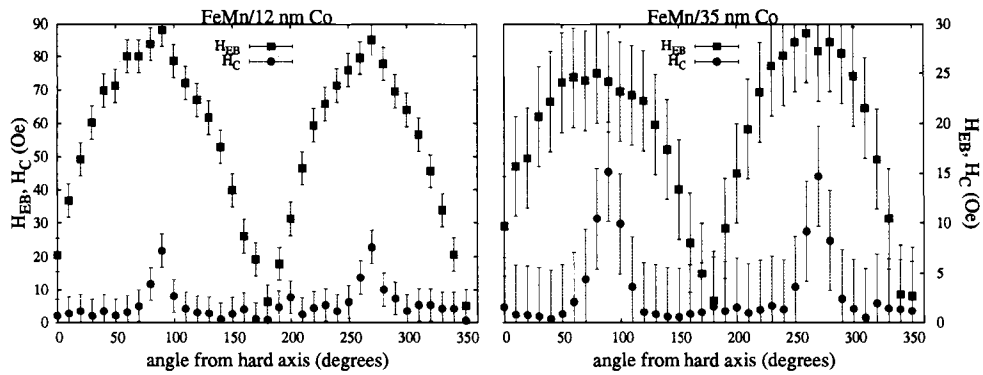


FIG. 6.9: H_{EB} and H_C as a function of angle between the applied field and H_{EB} for FeMn/(12 / 35 nm) Co. In this case, the angle is measured from the hard axis to the applied magnetic field. H_{EB} is typically negative, but the absolute value of H_{EB} is plotted here.

Figure 6.9 shows H_{EB} and H_C measured by the MOKE, versus applied field angle. The 0° angle means the hard axis and the applied field are aligned. H_{EB} and H_C reach a maximum at 90° and 270° , when the applied field is parallel to the pinning axis. The strong two-fold symmetry indicates that the system is well-pinned. Previous work on NiFe/CrMnPt_x exchange-biased systems has shown that as the quality of the pinning is compromised (for example by increasing the thickness of the AF layer) additional symmetries or lack of any symmetry in the angular data will result [110]. This does not appear to be the true for FeMn/Co.

The two-fold symmetry in the rotational MOKE data indicates that even for the thicker Co layer (35 nm), the Co film is well-pinned throughout the layer. If the thicker Co layer began switching according to a twist or significant rotation at the surface, it is expected that MOKE, being a surface-sensitive technique, would detect this. Other measurements using polarized neutron reflectivity taken by collaborators at NIST also suggest that no twist is present in the magnetization of the Co.

To summarize this Chapter, static MOKE studies were carried out on wedged FeMn/Co and IrMn/Co samples. The studies show that IrMn/Co is pinned well according to the square MOKE curves, strong linear dependence of H_{EB} vs. $1/t_{FM}$, and run-to-run corre-

lation. The measured interface exchange energy for IrMn compares well to the literature.

The FeMn/Co layers show a buffer layer dependence on the $1/t_{\text{FM}}$ measurements, as the Ta/Cu buffer layer exhibits a round hysteresis loop and a leveling off of H_{EB} at thin Co thicknesses, but the W/Cu buffer layers shows square loops and reasonable $1/t_{\text{FM}}$ dependence. The interface exchange energies for both buffer layer systems are within reported results in the literature. Rotational studies on single-thickness films show that the pinning in FeMn/Co is strong even at larger thicknesses, indicating that it may be used as a model system provided that the buffer layers are controlled carefully. In wedged FeMn/Co and IrMn/Co, a domain wall that sweeps from the thick to the thin side is the cause of the magnetization reversal in the FM. The next chapter will use the ultrafast laser to probe the dynamic magnetic properties of the IrMn/Co system using the Kerr effect.

CHAPTER 7

Pump-probe MOKE Results

This chapter presents measurements on exchange-biased thin films using ultrafast pump-probe MOKE. These experiments were carried out on various IrMn/Co samples because of the buffer layer problems with FeMn/Co discussed in Chapter 6. The pump-probe technique is a novel way to probe the time domain response of the magnetization of magnetic materials.

A goal of this Chapter is to show that the time domain pump-probe technique is able to extract comparable information to FMR. To do this, we compare to FMR data points to the points we extract from the time-domain pump-probe measurement and conduct the data analysis using standard FMR techniques.

The results from this Chapter show that the single-frequency coherent magnetization oscillations can be produced and measured in metallic exchange-biased systems by ultrafast pump-probe techniques. The frequency dependence at a fixed angle between H_{EB} and H_A has been studied, and it was found that standard FMR data analysis models fit the data well. The Gilbert damping parameter α has been extracted from the damping in the oscillations and is comparable to what is seen in the literature. Angular dependence at a fixed field was also studied. In addition, pump-probe hysteresis loops were taken and

they show dramatically different behavior along the hard and easy axes, with a fast (<5 ps) time response to the pump laser.

7.1 Experimental Details

The samples in this Chapter are different IrMn/Co samples from those in the previous chapter. They are grown the same way as the others in Chapter 6, but consist of single-thickness Co films. Because we concluded in Chapter 6 that the FeMn/Co samples have a sensitive buffer dependence, they were not included in this study. The structure of these samples is 5 nm Ta / 5 nm Cu / 10 nm IrMn / x nm Co / 2.5 nm Al₂O₃, where the Co thickness varied from sample to sample. The initial pinning was achieved by cooling from 250°C in a field of 100 Oe.

7.2 Ultrafast Oscillations

The experiments in this chapter were conducted using the ultrafast laser system under the conditions discussed in Sec. 5.4. To review, the idea is that two pulses of light are delayed relative to each other. The first (pump) beam excites the sample by fast electronic heating [14] followed by energy transfer into the lattice. This causes a new equilibrium in the magnetization and a launching of spin waves in the sample that is detected by a delayed second (probe) pulse using the Kerr effect. The pump pulse essentially provides a “kick” such that the magnetization will precess. This is measured using the probe pulse.

The expected results are ultrafast oscillations of the magnetic moment about the applied field. The oscillations can be described by the LLG equation discussed in Sec. 4.3. Assuming a small perturbation from equilibrium, the Gilbert damping is $\alpha \ll 1$, and we can use FMR analysis on these oscillations to check to see if the parameters extracted from these fits are comparable to FMR.

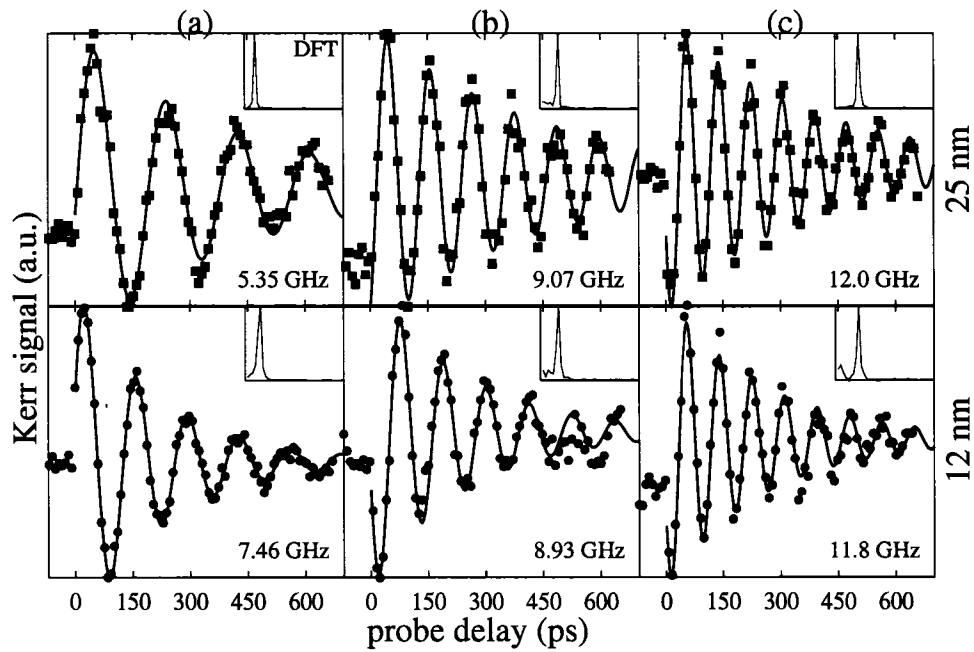


FIG. 7.1: Pump-probe MOKE signal as a function of pump-probe delay in various external applied fields. Shown are example plots of the pump-probe MOKE signal as a function of pump-probe delay for IrMn/Co for two Co thicknesses, 25 nm Co (top) and 12 nm Co (bottom) at three different orientations of the pinning axis about the applied field direction (ϕ_{EB}) and applied field strength. The oscillations are for column (a) 0° and 214 Oe, column (b) 30° and 490 Oe, and column (c) 60° and 935 Oe. The lines are fits to an exponentially damped sinusoidal in Eq. (4.8). Frequencies extracted from the fits and the discrete Fourier transforms (DFT) are inset in each panel, showing a single-frequency peak.

Figure 7.1 is a representative set of the magnetic oscillations as a function of delay between the pump and probe. Two samples are represented here, the 25 nm Co sample (top, blue squares) and the 12 nm Co sample (bottom, red circles). Both use IrMn and the AF with Ta/Cu buffer layers. For these two samples, the oscillations are shown for different orientations between the magnetic field and the H_{EB} axis and magnetic field strengths. Here, column (a) is for 0° and 214 Oe, column (b) is for 30° and 490 Oe, and column (c) is for 60° and 935 Oe. The fits to Eq. (4.8), shown as black lines, are an approximate solution to the LLG equation based on small perturbations outlined in Sec. 4.4. To ensure that the fits are single-frequency, the discrete Fourier transform is shown inset in each of the figures. All of the DFTs show a single peak in the frequency spectrum. The frequencies extracted from the fits are shown inset and are in the GHz range.

For the following analysis, the frequencies extracted from the sinusoidal fits are used instead of the DFT frequencies because the spectral resolution of the DFT is limited by the length of the delay stage. Specifically, for the length that we travel down the delay stage the precision in the frequency is ± 1.3 GHz. If the DFT frequencies were used in Fig. 7.1, columns (b) and (c) are indistinguishable from each other, as the frequency difference between the 12 nm and 25 nm at those given field strengths and orientations are within 1.3 GHz.

7.3 FMR Analysis of Pump-Probe Data

The goal of this analysis is to determine if the quantities extracted from FMR analysis of the optical data presented here give results similar to traditional FMR measurements. This will be done using FMR analysis of the frequencies that have been extracted from the all-optical data.

From the plots shown in Fig. 7.1, the oscillation frequency versus the applied exter-

nal field can be plotted for different angles between the field and the H_{EB} axis. A plot of the data for the 25 nm Co sample is shown in Figure 7.2. The fits to the data points are shown with solid lines. Also shown in Fig. 7.2 is a data point using the traditional FMR measurements. As can be seen, the optical frequencies correspond well to that measured by traditional FMR.

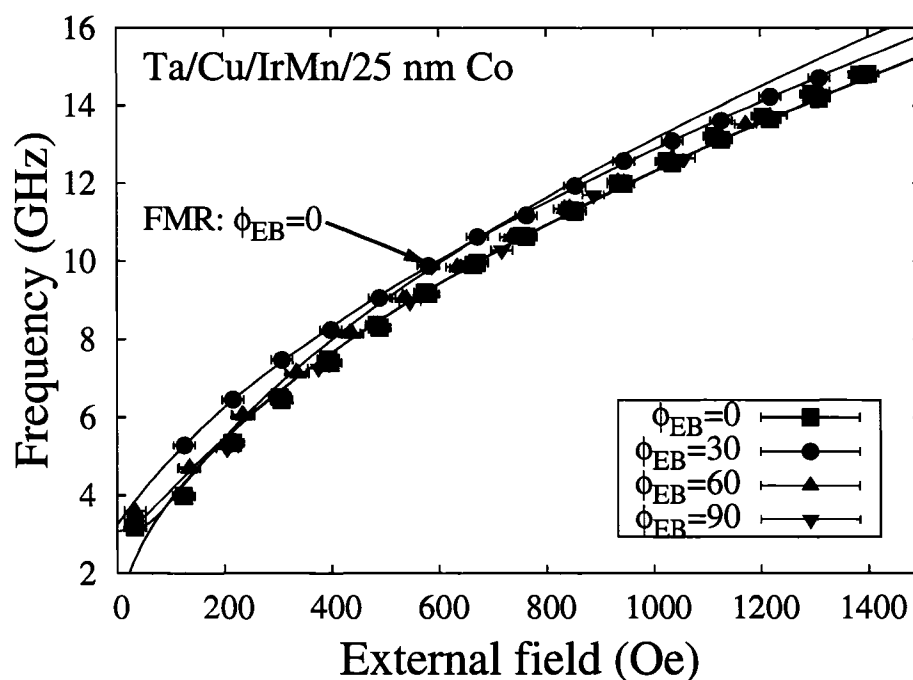


FIG. 7.2: Extracted oscillation frequency versus external field for IrMn/25 nm Co. The curves are shown for different angles between H_{EB} and H_A with an FMR point for the $\phi_{EB} = 0$ is shown for comparison. The fits from Eq. (4.21) are shown.

By using FMR analysis developed in Sec. 4.5 with the free energy terms discussed in Sec. 4.5.1, a relationship between the external field and oscillation frequency can be extracted. The resonance condition shown in Equation (4.23) has numerous parameters— H_A , H_{EB} , H_D , g -factor, and ϕ_{EB} . For this section the fitted parameters will be the exchange bias field H_{EB} and demagnetization field H_D . The other parameters (g -factor, ϕ_{EB}) are taken as fixed quantities for these experimental conditions. Figure 7.2 is a plot of the frequency versus field for an exchange-biased IrMn/25 nm Co sample using the

data extracted from the top row of Fig. 7.1. Four data sets are shown here corresponding to different orientations between the applied field H_A and H_{EB} axis. For this sample, oscillations were measured between $H_{EB}-H_A$ of 0-90° in 15° increments, but the data taken every 30° is only shown here for clarity.

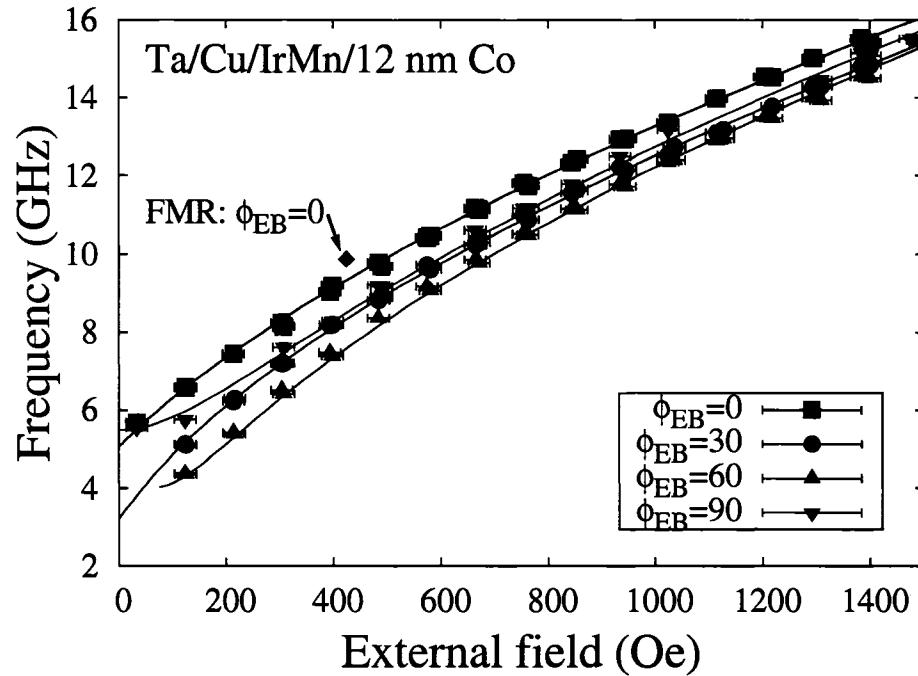


FIG. 7.3: Extracted oscillation frequency versus external field for IrMn/12 nm Co. The curves are shown for different angles between H_{EB} and H_A with an FMR point for the $\phi_{EB} = 0$ is shown for comparison. The fits from Eq. (4.21) are shown.

The same analysis was conducted with the IrMn/12 nm Co sample. The results are shown in Figure 7.3 for various angles between H_{EB} and H_A . Another FMR point taken on this sample in the orientation where H_{EB} and H_A is aligned is shown in light blue, that should be compared to the dark blue squares from the all-optical measurements.

Here again, the fits to the data are good as the lines seem to fit well over the data points. From these fits, the values for H_{EB} and H_D are shown in Table 7.1. It should be stressed that the goal of this project was to see how FMR analysis of all-optical data would compare with FMR. This, along with the FMR points in Fig. 7.2 and Fig. 7.3

12 nm Co				
ϕ_{EB} (degrees)	$ H_D $ (Oe)	error (Oe)	$ H_{EB} $ (Oe)	error (Oe)
0	14,516.2	95.89	183.569	4.631
30	14,417.5	79.25	75.879	3.78
60	15,718.1	127	124.063	12.27
90	15,767.3	119.6	199.832	9.25
average	15,104.8		145.84	
25 nm Co				
ϕ_{EB} (degrees)	$ H_D $ (Oe)	error (Oe)	$ H_{EB} $ (Oe)	error (Oe)
0	14,834.1	170.6	7.02657	5.562
15	15,550.5	51.57	72.2457	2.094
30	15,336.4	74.17	71.4255	3.247
45	15,083.5	56.89	64.2714	2.551
60	17,792.9	398.3	67.1959	0.01083
75	14,928.9	92.72	78.7833	4.862
90	14,875.3	170.4	66.8738	8.382
average	15,485.9		61.117	

TABLE 7.1: Extracted values for H_D and H_{EB} using Eq. (4.23) for various angles between H_{EB} and H_A . The fits use a non-linear least-squares algorithm [111] with the standard deviation of each parameter shown as an error. The values are for a fixed g -factor of $g = 2.2$.

provide some evidence that the experiments are measuring comparable quantities.

From the BH loops taken on the samples before these pump-probe experiments were conducted, the H_{EB} shifts were 67.27 Oe (with a coercivity of 64.75 Oe) and 25.43 Oe (with a coercivity of 38.12 Oe) for 12 and 25 nm Co respectively. The FMR calculations for the frequency-field relationship in Sec. 4.5 assume that H_{EB} value that is used has zero coercivity, ie: the H_{EB} field is really the switching field. In most samples, the H_C field is non-zero (in fact the exchange bias interaction enhances H_C [2]), and it must be considered in the fits. It seems more accurate to compare the values extracted from the FMR fits in Table 7.1 to the switching fields ($H_{EB} \pm H_C$) from the BH loops [112]. The switching fields for increasing field are 132.02 Oe and 63.55 Oe for 12 nm and 25 nm Co, respectively. These values compare favorably with the extracted values for H_{EB} from Table 7.1, with the 25 nm Co value within 3 Oe of each other and the 12 nm Co value within 15 Oe of each other.

Table 7.1 shows some anomalies in the data. The most obvious is the striking discrepancy in the 25 nm Co data between the H_{EB} - H_A angle of 0 degrees and the other angles in that data set. For 0 degrees, the H_{EB} field is about a factor of 10 smaller than the other values. We believe that H_{EB} value is abnormally small because the assumptions by which the FMR frequency-field equation is derived in Sec. 4.5 breaks down along the easy axis. It is assumed that a small perturbation from equilibrium causes the magnetic moment to oscillate. Along the easy axis, particularly at large fields, the traditional theory of H_{EB} destruction and recovery where oscillations are launched in this process does not apply. The details of why it does not apply will be discussed in Chapter 8. We are unsure why the same effect of a small fitted H_{EB} is not seen for the 12 nm Co sample along the easy axis as it is seen for the 25 nm Co sample. Even though the alignment of the H_{EB} axis in the magnet was done by eye, this is not a factor in the fits. The fits were refitted assuming an error of 2–3° in the orientation of the H_{EB} axis but yielded similar results for H_D and H_{EB} .

The demagnetization field was measured on a portion of the IrMn/12 nm Co sample using a SQUID magnetometer. The SQUID experiment measures the magnitude of the magnetization as a function of field. SQUID was used to measure the demagnetization field instead of MOKE because the value for the demagnetization field is much larger than the magnetic fields that can be achieved in the MOKE experiments. The measurement, shown in Figure 7.4, is of the out-of-plane magnetization component. A large linear diamagnetic component is shown in the inset which needed to be subtracted out of the final curve, which is shown in the main graph. The demagnetization field is the field required to pull the magnetization out of plane. This manifests itself as the field where the magnetization is the largest in the hysteresis plot. For this sample, the demagnetization field is 19 kOe. From Table 2.1 the bulk demagnetization field value is 17.9 kOe, comparable to what is measured in the SQUID.

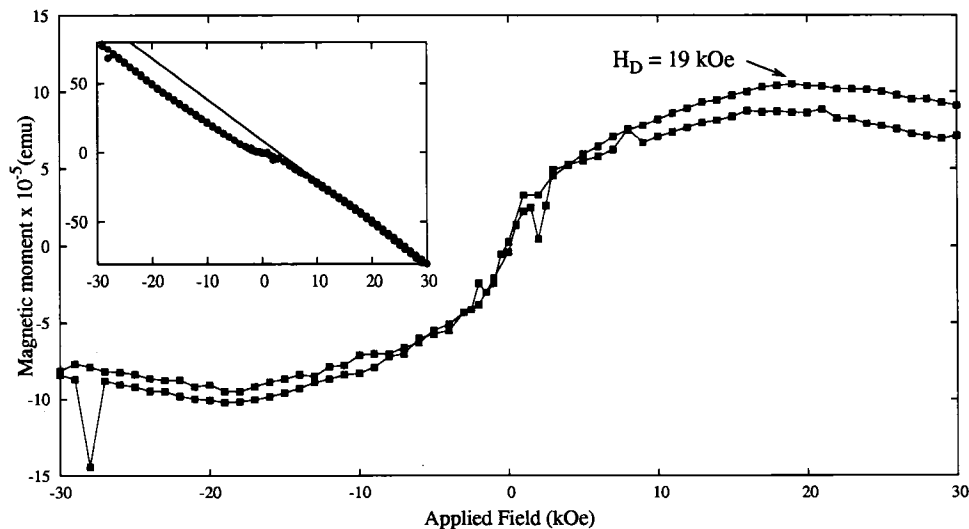


FIG. 7.4: SQUID measurement of the perpendicular component of the magnetization on IrMn/12 nm Co. The demagnetization field extracted from this curve is 19 kOe. Inset is the initial data before the paramagnetic effects of the sample, shown as a linear fit in black, is subtracted out.

Comparing H_D from Fig. 7.4 and Table 7.1, it is possible to compare how accurate the extracted parameters from fitting the FMR equations are to the same parameters measured using other techniques. For H_D , the values we extract are 15% different compared

with the bulk measurement of 17.9 kOe, and more for H_D extracted from the SQUID.

The behavior of g in the fitting formula Eq. (4.23) has also been analyzed. When setting g as a free parameter in the fit, it tends to either increase or decrease out of the acceptable range of values, set to be $g = 2.0 - 2.2$. The H_{EB} and H_D values that are extracted from these fits are unreasonable. When attempting to allow g to be a free parameter in a range of $2.0 - 2.2$, g tends to either 2.0 or 2.2 in the final fits, and the H_{EB} and H_D values are unreasonable. We decided then to fix $g = 2.2$ as a reasonable value. Estimates using FMR have $g = 2.15 - 2.26$ for cobalt with the bulk value being 2.18 [113].

7.4 H_{EB} - H_A Angle Dependence of Spin Wave Frequencies

The angular dependence of the extracted frequencies was also studied for a IrMn/25 nm Co sample. This was done using the same rotation mount that was used in the static MOKE measurements in Sec. 6.5. Because of hysteresis, the applied field was set to positive saturation then decreased to the desired field value.

The plot of the angular dependence of the oscillation frequency is shown in Figure 7.5 for fixed fields. The fits to Eq. (4.23) are shown as solid lines. The free parameters in the fits are H_{EB} and H_D . Again, as in Sec. 7.3 we emphasize that the data, although extracted from a time-domain experiment (pump-probe MOKE), fit well to a frequency-domain analysis technique (FMR).

For all fields the fits to the data points, shown with lines, look good. The parameters to the fits are shown in Table 7.2. Overall, the parameters for H_D in Table 7.2 are low compared to the SQUID measurement (Fig. 7.4) and the other set of FMR fits (Table 7.1). The H_{EB} values extracted are also slightly above the fitted values from Table 7.1. Most

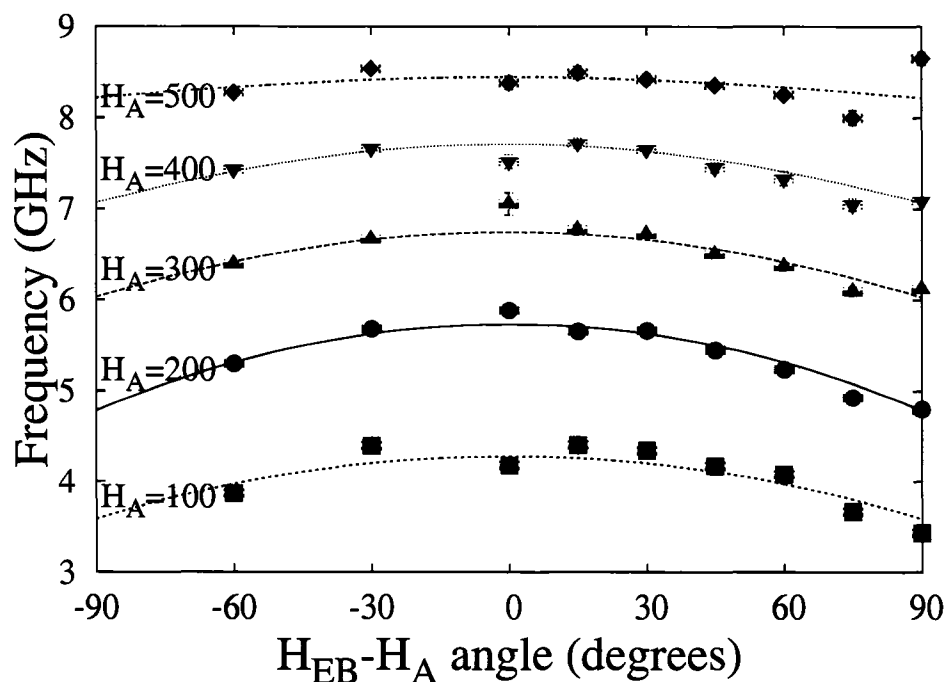


FIG. 7.5: Angular dependence of the spin-wave frequency for fixed external fields for IrMn/25 nm Co. Shown are the angular dependence of the oscillation frequency as a function of applied field for fixed field values. The fits are to Eq. (4.23) with free parameters H_D and H_{EB} . The applied field values H_A are shown on the left in Oe.

H_A (Oe)	H_D (Oe)	error (Oe)	H_{EB} (Oe)	error (Oe)
100	9326.45	482500.	102.606	10050.
200	7920.56	32490.	215.038	1541
300	11944.9	418	89.5108	15.68
400	12490.1	237.6	83.1515	11.26
500	13718.5	526.2	27.936	26.79

TABLE 7.2: Extracted values for H_D and H_{EB} as a function of applied field using Eq. (4.23) for IrMn/25 nm Co. The fits use the same equation as Table 7.1 with the same free parameters except the field is held constant and the angle is varied. This is the opposite as Table 7.1 where the angle is held constant and the field is varied. The fits use a non-linear least-squares algorithm [111] with the standard deviation of each parameter shown as an error. The values are for a fixed g -factor of $g = 2.2$.

striking, however, is the errors for H_{EB} and H_D at 100 Oe and 200 Oe applied fields. The errors here are larger than the extracted values for H_D and H_{EB} . We suspect that this is because the angle calculated for the magnetization can change dramatically at low fields, as this is the area where the magnetization switches from the positive saturation to negative saturation state. The equation to calculate the magnetization direction (Eq. (4.15)) does not take hysteresis into account, so at low fields it is possible to be at two points in the magnetization; the hysteresis loop has two different points that correspond to that field. At larger fields, the magnetization has saturated and Eq. (4.15) can calculate the magnetization angle well.

We also tried to refit Fig. 7.5 with $g = 2$, which yields nearly the same values for H_{EB} at all applied fields (including errors) but gives demagnetization fields about 21% larger, with the errors in the demagnetization fields larger by the same percentage.

7.5 Damping Coefficient

Another important aspect of these oscillations is the magnitude of the Gilbert damping involved with the oscillations. In magnetic structures, such as hard disk drive read heads, the switching time between magnetic states depends on the damping in these systems. To quantify this, the damping has been extracted from the oscillations in Fig. 7.1 using Eq. (4.9). The damping extracted for Fig. 7.2 and Fig. 7.3 is shown in Fig. 7.6 for IrMn/25 nm Co and IrMn/12 nm Co.

In neither graph does there appear to be any appreciable field dependence of the data. It also appears that, although the error bars are small compared to the spread of all of the data points, the damping is independent of the H_{EB} - H_A angle ϕ .

The Gilbert damping coefficients extracted from the oscillations are larger than reported values of $\alpha = 0.005$ for bulk cobalt from the literature [114, 115]. Others [116, 117, 118] have reported larger values for thin Co systems or exchange-biased Co sys-

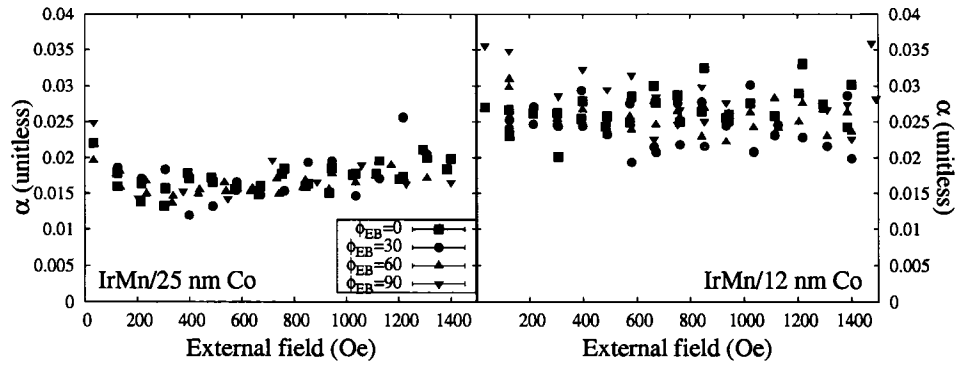


FIG. 7.6: Damping parameter α versus applied field. Shown here is the IrMn/25 nm Co (left) and IrMn/12 nm Co (left). The damping parameter is calculated from Eq. (4.9) and depends on the damping in the pump-probe MOKE scans and M_S .

tems. Because of two-magnon scattering where the lowest mode magnon (measured here in Fig. 7.1) scatters energy to another mode through defects in the system or local fluctuations in the exchange energy caused by the pump beam, the damping for exchange-biased systems has been reported to be enhanced [119, 120, 121]. Although the enhancement seen here compared with the bulk, the all-optical technique is relatively new and may be providing more or alternative information from other traditional measurements where the damping is extracted, such as FMR. Other measurements on Mn/Co exchange-biased Co wedges report that α varies (depending on the exchange bias field) from $0.05 \leq \alpha \leq 0.2$ [122].

7.6 Pump-probe Hysteresis Loops

In the previous work in this chapter, the applied field has been fixed and the delay has been changed to extract time dependent information of the Kerr signal. The experiments in this section instead set the delay to a fixed time and sweep the field to observe changes in the hysteresis loops as specific times. For static measurements the sweeping of the field traces out a magnetic hysteresis loop shown in Chapter 6.

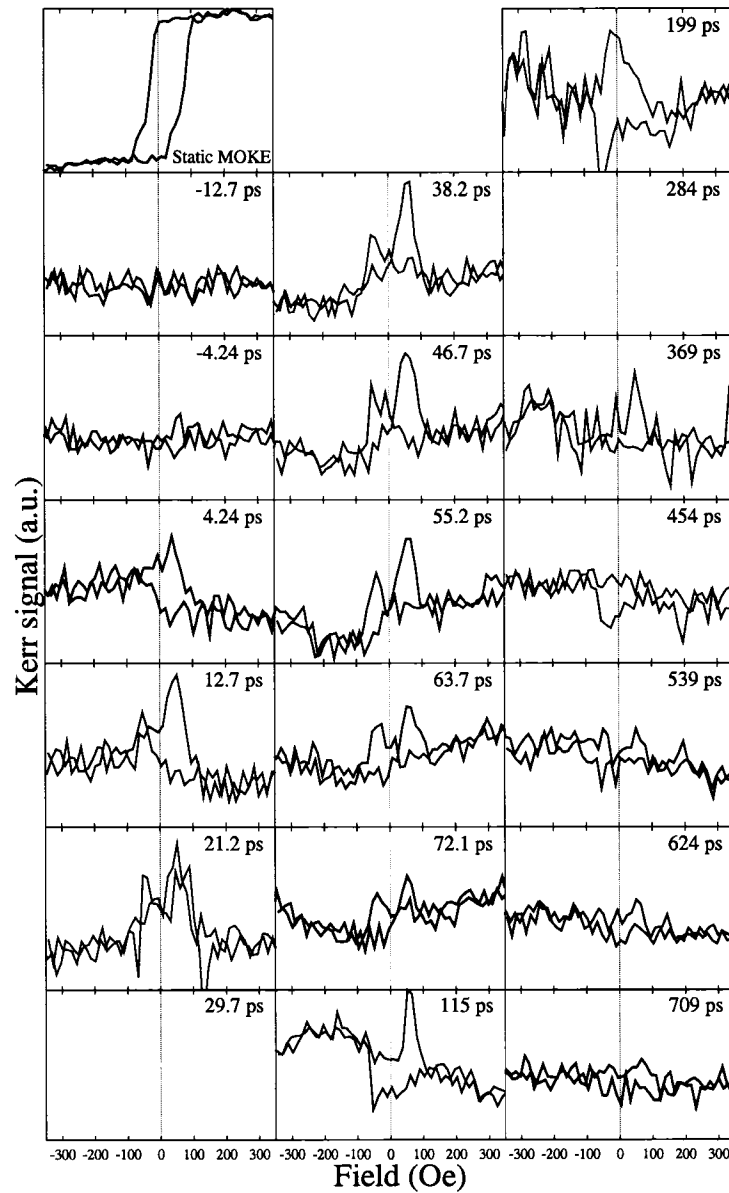


FIG. 7.7: Easy axis hysteresis loops for various delay times between pump and probe for an IrMn/15 nm Co sample. When the probe arrives before the pump (indicated by negative time), the signal does not have a field dependence. When the probe arrives after the pump, two peaks are shown that roughly correspond to the switching fields in the static MOKE (pump blocked) loop, shown on the top left.

Figure 7.7 shows the results of the dynamic hysteresis loops along the hard axis for a IrMn/15 nm Co sample. The Kerr loop in the top left shows a hysteresis loop when the pump beam is blocked and the lock-in amplifier references the 1 kHz repetition rate from the amplified system. Once the pump is unblocked and the lock-in amplifier references the frequency of the optical chopper, chopping the pump, the lock-in detects the *change* in the Kerr signal from the pump. The panels in the Figure represent fixed delay times between the pump and probe. The time overlap (0 ps delay) was calibrated using a reflectivity signal from the surface of the Co.

At a short time after the pump pulse arrives (4.24 ps), the remnants of an inverted hysteresis loop appear. As the time delay is increased, a double peak begins to appear. In each graph, the peak on the right occurs as the field is increasing (meaning that the field is swept from $-H$ to $+H$), and the peak on the left occurs as the field is decreasing. The peaks, and the occurrence of them in terms of the sweep direction, seem to correlate with the switching fields and reversal of the magnetization in the static hysteresis loop. This means that the largest pump-induced change in the magnetization is at fields where the magnetization is switching. Incidentally, a derivative of the static MOKE loops leads to a plot similar to Fig. 7.7 for 55.2 ps, with two peaks at the points where the field switches.

The third column of Fig. 7.7 shows the long time response of the Kerr signal. These plots are flat, indicating that the damping has caused the magnetism to stabilize and the pump-induced change is zero.

Figure 7.8 shows the same technique taken on the hard axis. The top left shows a static MOKE curve of the hard axis, with the pump beam blocked. As in the previous easy axis data, when the pump arrives after the probe no field dependence is present. Also, when the probe arrives a short time after the pump (5.94 ps) remnants of the static hysteresis loop exist, similar to what is seen in the easy axis configuration. It appears that the peaks in the hysteresis loop in intermediate delay times (20–80 ps) correlate roughly to the point where the magnetization begins to switch. The easy axis exhibits similar

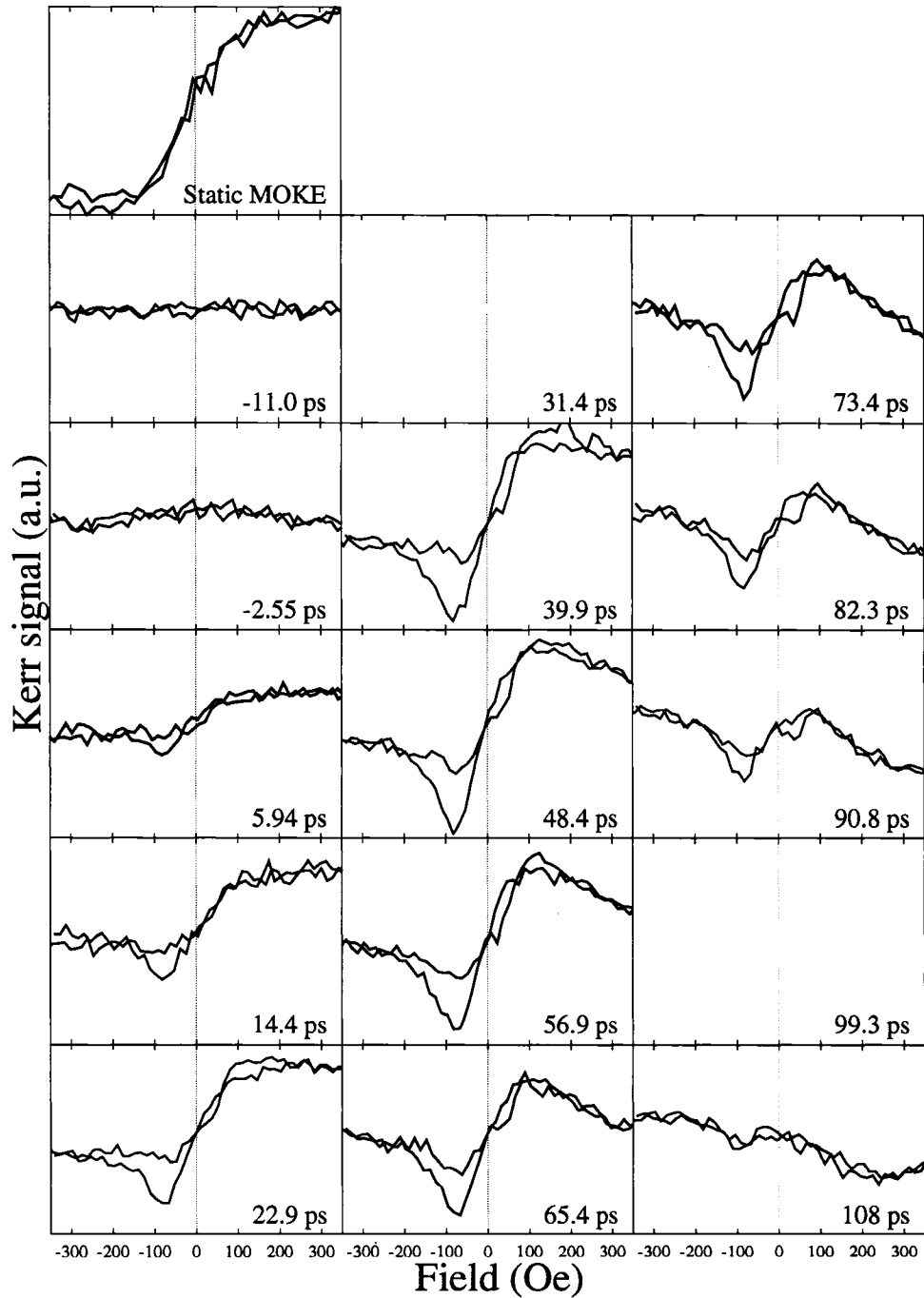


FIG. 7.8: Hard axis hysteresis loops for various delay times between pump and probe for an IrMn/15 nm Co sample. Down each column is increasing delay time between the pump and probe. At larger delay times the pump-probe signal gets weaker, indicating the damping in these systems. The top left plot is a static MOKE loop with the pump beam blocked.

behavior, but because this is a hard axis the switching field is not well defined since the magnetization switches over a range of fields (-100 to 100 Oe from the static MOKE loop).

Although the y -axis in this Figure uses arbitrary units, the data uses the same arbitrary units and it is valid to compare the values in each of these panels. The scale in each of the panels is the same. For example, one can see that at a field of 300 Oe, the magnetization at 22.9 ps decreases gradually as the delay is increased. The other observation is that in the intermediate delay time regime (20–80 ps), the Kerr signal has hysteresis—that is the signal depends on the previous direction of the magnetization. This can be most easily seen at about -80 Oe, where the Kerr signal has two different values depending on if the field was increasing ($-H$ to $+H$) or decreasing ($+H$ to $-H$).

From the observation that the magnetization decreases (and increases) for various fixed fields, we attempted to visualize the magnetic oscillations using the static hysteresis data. This is shown in Figure 7.9 for the hard axis. Since hysteresis is important in these samples, the data are plotted for half of the hysteresis loop, (a) for decreasing field ($+H$ to $-H$) and (b) for increasing field ($-H$ to $+H$).

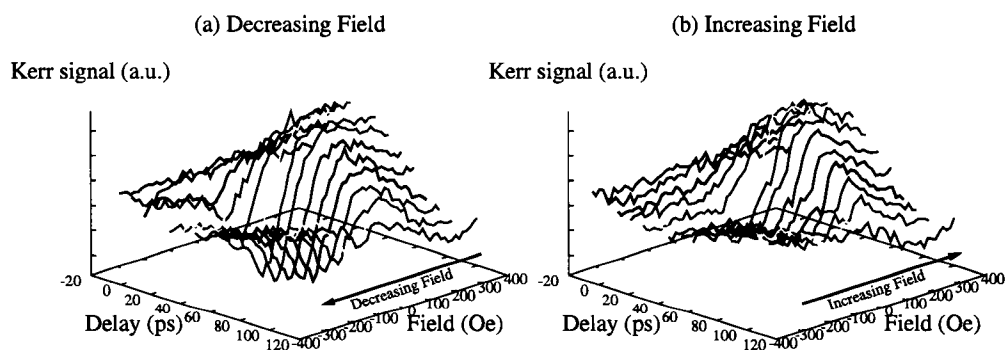


FIG. 7.9: Three dimensional map of the decreasing field for IrMn/15 nm Co along the hard axis. This plot is extracted from the hysteresis loops taken in Figure 7.8 for two parts, the field values from positive saturation to negative saturation. For a given fixed field the half-cycle of an oscillation can be picked out from the data, similar to what is seen in Fig. 7.1.

By observing the Kerr signal while at a fixed field point in Fig. 7.9 one can observe a trace of oscillations in along the time axis. It is most obvious by tracing the valley near -100 Oe in (a) and the peak at 100 Oe in (b), where a half-cycle of the magnetic oscillation can be observed. It is also clear in both plots that at positive saturation the magnetization goes through just over one half of a cycle.

Now it is possible to model Fig. 7.9 by using FMR analysis. The frequency of the oscillations obey Eq. (4.23) and it was shown in Sec. 7.3 that they fit well to the frequencies we measure. These frequencies we measure are extracted from a decaying oscillating exponential described by Eq. (4.8), and Sec. 7.5 showed that the damping coefficient is independent of field. From all of this, a 3D map can be theoretically modeled to compare to Fig. 7.9. The theoretical model is shown in Figure 7.10.

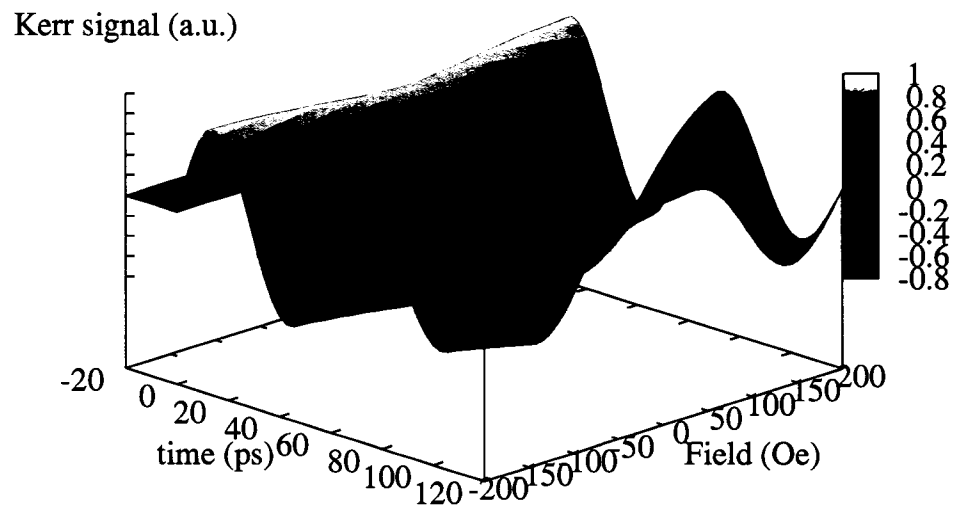


FIG. 7.10: Theoretical model of Fig. 7.9 using the FMR (Eq. (4.23)) and oscillation fit (Eq. (4.8)) equations. From the edge of the plot ($H_A = -200$ Oe) one can see the trace of the oscillations in the time axis. As the field gets closer to zero, the frequency of the oscillations decrease.

Some features in Fig. 7.10 that are important. First, the frequency of the oscillations

increase as the field is increased. This is inferred from the field dependence of the maximum field and the fact that the peaks get closer together as the field is increased. Second, the zero field situation shows no oscillations or a long period of oscillation, similar to the data we see.

The major difference between Figure 7.9 and Figure 7.10 is that Fig. 7.10 shows more increasing oscillations at higher fields. It is not yet clear why the experiments and theoretical calculations do not match up, but it is not surprising. From the dynamic hysteresis loops, it appears that the magnetization follows different reversal mechanisms depending on how the field is swept because the two traces of the curves for increasing and decreasing field are different. One would expect that if the reversal mechanism was the same, the two halves of the dynamic hysteresis loops would be the same along the hard axis. Asymmetry in magnetization reversal has been reported before in static [109, 123, 124] and dynamic [125] measurements.

To summarize, ultrafast pump-probe MOKE time-domain measurements were done on exchange-biased IrMn/Co samples at all orientations and applied fields. In particular, the frequencies extracted from the pump-probe measurements fit well to equations generated from standard FMR analysis, a frequency domain technique. The angular dependence of the frequencies were studied for fixed fields using the same FMR equation. These fit well too, but begin to degrade at large fields. It is not yet clear why this happens. Pump-probe hysteresis measurements were also completed by fixing the pump-probe delay and sweeping the field. These show that the magnetization responds quickly, occurring less than 6 ps. The easy axis and hard axis curves from this show different behavior, but the results are quantitatively explainable. Using these pump-probe hysteresis scans, the oscillations were reconstructed by stacking successive pump-probe scans on a three-dimensional map. This was modeled theoretically and shown to be somewhat comparable. The next chapter will explore the effects of the pump-pulse on the magnetic properties of the exchange-biased structures.

CHAPTER 8

Pump-Induced Exchange Biasing

In the last Chapter it was shown that the pump can induce oscillations under any applied field strength and field angle about the pinning axis. Given this, clearly the mechanism providing the magnetization perturbation is different than that seen before. We propose that the oscillations we measure are due to a pump-induced setting of the exchange bias.

This Chapter reviews other mechanisms seen before in exchange-biased systems and introduces a model for the behavior we see. Evidence for the pump-induced setting of the exchange bias interaction is given.

8.1 Background

The current phenomenological theory on the excitation of magnetic oscillations was offered by Beaurepaire *et al.* [14] for ferromagnetic nickel and extended to exchange-biased systems by Ganping Ju *et al.* [9]. When the laser pulse hits the exchange-biased sample, the exchange biasing is temporarily destroyed through electron heating and subsequent heat transfer into the lattice. This destruction changes the shape of the hysteresis

loops and launches magnetic oscillations that are detected by the probe pulse. The oscillations follow the LLG equation.

According to Ju *et al.* [9], the oscillations disappear in the region where the applied field is large enough to completely pull the magnetization into the direction of the field. Also, along the easy axis in the saturation regime the oscillations disappear. By “disappear” we mean that they are not observed in the pump-induced MOKE signal. The reason that the oscillations disappear can be shown using the LLG equation in Eq. (4.7). When \mathbf{M} and \mathbf{H} are in the same direction as they are in the saturation regime, the term $\mathbf{M} \times \mathbf{H} = 0$, and the RHS of Eq. (4.7) is zero and the magnetization vector has no time dependence. This is not true at other orientations of H_{EB} and H_{A} (besides 180°) because the H_{EB} field, which is included in \mathbf{H} , will have a component that is not collinear with H_{A} and $\mathbf{M} \times \mathbf{H} \neq 0$. Others have reported oscillations along the easy axis, but these are in specific cases where the applied field has not yet saturated the sample or the applied field is at a value such that the destruction of the exchange biasing creates a reorientation of the magnetization vector that provides the “kick” to launch oscillations [8, 9, 16].

One can also argue from inspecting the phenomenological description of the hysteresis loops before and after the pump pulse hits that oscillations should not occur in certain applied field regions. This is generally formulated as an energy argument where, by tracing the hysteresis loop, one can find regions where the applied field has pulled the magnetization along the applied field direction, which is unaffected by the destruction of the hysteresis loop by the pump pulse.

Figure 8.1 is a sketch of the theory behind oscillations along the easy axis. The left panel shows an applied field H_{A} where oscillations occur, and the right panel shows a field H_{A} where they do not occur. In each configuration the FM layer is shown with an arrow representing the magnetic moment, and a sketch of the hysteresis loop. In the hysteresis loop sketch an arrow points to the magnetic configuration for the applied field H_{A} . For the left panel (a) at $t < 0$, the magnetization is in a state near the switching

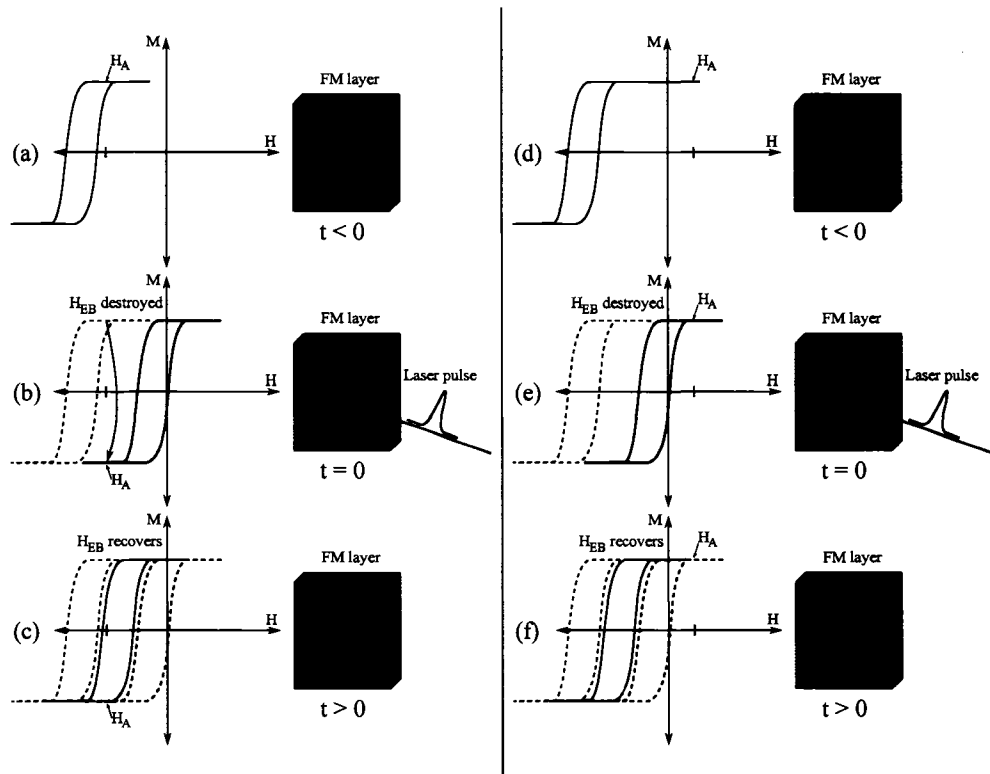


FIG. 8.1: Sketch of the conditions necessary for oscillations along the easy axis. The left panel shows a H_A near saturation and oscillations are possible. The right panel shows an applied field H_A where the destruction of H_{EB} does not affect the magnetic configuration and provide a “kick” to start the precession. The magnetic configuration of the FM layer is shown to the right of the hysteresis loop for $t < 0$ (top row), $t = 0$ (middle row), and $t > 0$ (bottom row).

field and M and H are aligned. When the laser pulse hits the sample at $t = 0$ (b) the H_{EB} is destroyed, which shifts the hysteresis loop (solid green) towards zero. At H_A the state of the magnetization is opposite from (a) and the magnetization begins to reverse, shown with a black arrow on the hysteresis loop. This is the “kick” required to launch oscillations. At $t > 0$ and H_{EB} recovers shown in (c) with another transient loop shown as solid brown.

The right panel of Fig. 8.1 shows an applied field H_A where oscillations do not occur. The applied field here (d) is large enough that when the laser pulse hits the sample in (e), the shifted hysteresis loop remains a configuration where M does not need to reorient since the magnetic configuration in (e) at H_A is the same as in (d). During the recovery, shown in (f), the magnetization is still aligned with H_A and oscillations are not possible since H and M are aligned. Evidence for the shifts of the hysteresis loop as a function of probe delay time was given by Weber *et al.* [13].

8.2 Model of Pump-Induced Setting of Exchange Biasing

What is observed in our experimental results is strikingly different from what has previously been seen. Figure 8.2 shows the easy axis oscillation frequencies for IrMn/(12 and 25 nm) Co along with hysteresis loops taken along the easy axis. Two vertical lines on the main curve show where the hysteresis loop (inset) reaches saturation. According to the hysteresis loop, the oscillations are present beyond fields larger than magnetic saturation. This is evidence that the mechanism by which oscillations are excited in other experiments (shown in Fig. 8.1) is not valid here. Most of the fields that we measured oscillations are much larger than the switching field of the samples measured, meaning that M and H are wholly aligned with each other. Using the model introduced in Sec. 8.1 leads one to expect a quenching of oscillations at large fields.

We propose that the oscillations are being induced by the pump positively setting

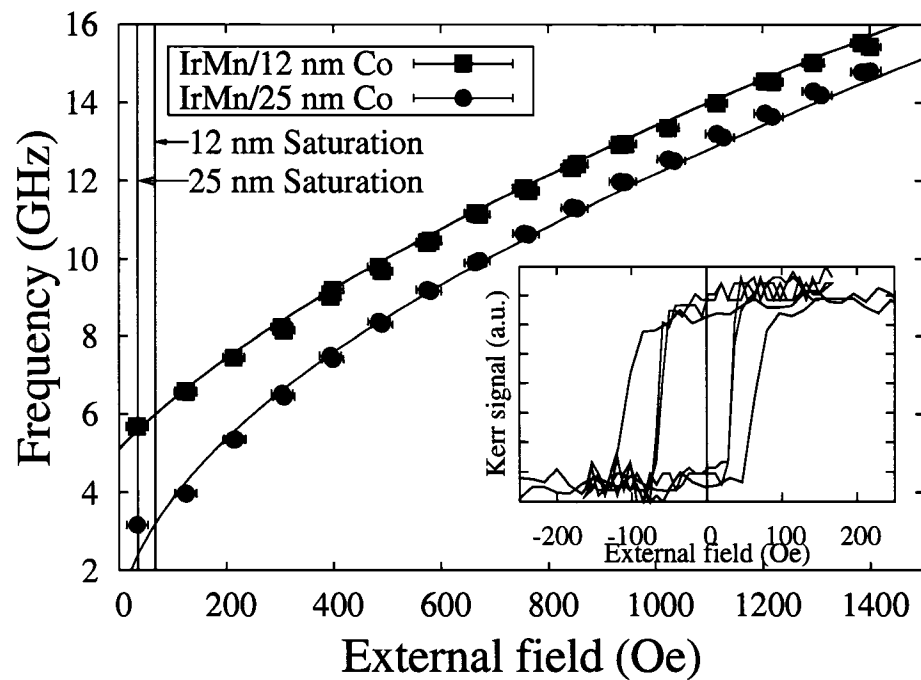


FIG. 8.2: Oscillation frequency data for IrMn/(12,25 nm) Co along the easy axis. The data are taken from Fig. 7.3 and Fig. 7.3 where H_{EB} is along H_A . Inset are the hysteresis loops for the 12 nm (blue) and 25 nm (red) curves showing that by an applied field of 100 Oe both the 12 and 25 nm Co systems have saturated.

the exchange bias interaction, and not just destroying it. This occurs in these samples because they are polycrystalline and the AF (and F) layer is made up of a distribution of grain sizes. When the exchange bias interaction (evidenced by a hysteresis loop shift) is set by heating and cooling the sample in an applied field, a significant portion of the AF grains become set toward the applied field, but not all the grains are set. This means that the setting of the exchange bias interaction is a thermally activated process.

8.2.1 Overcoming an Energy Barrier

The thermal fluctuation model by Fulcomer and Charap [28] and the model by Stiles and McMichael [27] were discussed in Sec. 2.4.4. It approximates the AF layer as a series of independent columnar AF grains. These grains couple to the FM layer via the exchange bias interaction. When uncoupled, the grains have a two-fold degeneracy because the two FM lattices used to form the AF sublattice can be constructed two ways, in an arbitrary configuration and a configuration where the spins are oriented 180° from initial arbitrary configuration. The degeneracy is released with the exchange interaction, providing a maximum and minimum energy separated by a barrier.

Because of the distribution of grain sizes in the AF layer, a distribution of energies of each grain is present. This distribution was discussed as the cause for the difference between a blocking temperature and Néel temperature in Sec. 2.2.1. The systems studied here will have a distribution of grains in the AF layer, some of which will be energetically easy to flip.

The laser power used in our experiments has been calculated to be in the regime where the energy barrier is accessible. A model is needed to describe the existence of oscillations along the easy axis. Our model, according to the work by Fulcomer and Charap, goes as follows. The laser hits the sample and energy is dumped first into the FM layer, then into the AF layer. A small portion of the grains within the spot size of the laser

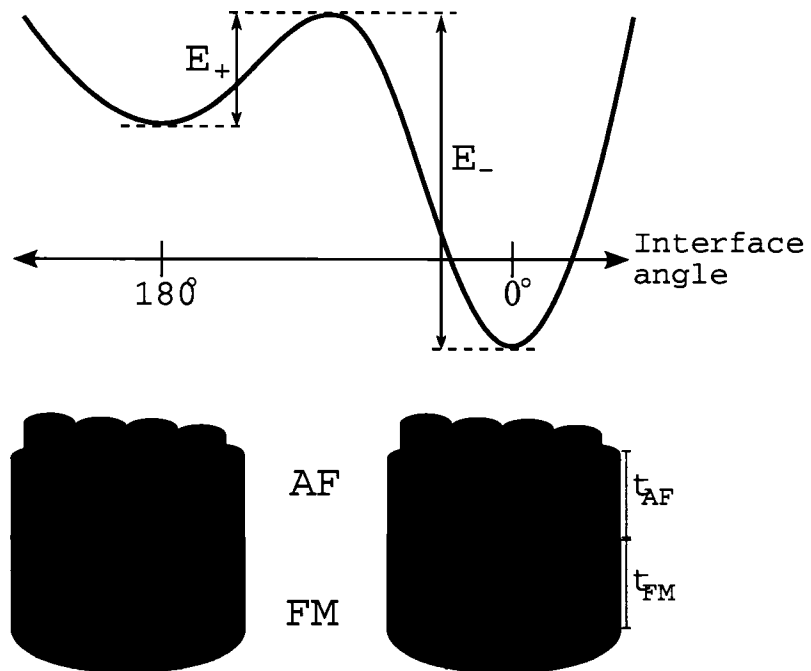


FIG. 8.3: Sketch of the thermally activated model for switching. The minimum energy state E_- is 0° , since most of the AF moments point with the FM in that orientation. The other energy minimum E_+ has fewer AF grains aligned with it. This model assumes that all grains are non-rotatable or “frozen-in”. This sketch is taken from Ref. [126].

are small and have energy barriers that are sufficiently low. These grains will flip 180° to the other degenerate state according to the energy map in Fig. 8.3, causing the FM layer via the exchange bias interaction to experience a perturbation that will launch precession along the easy axis.

One can explain the onset of oscillations shown in Fig. 8.2 in a similar manner. The oscillations past saturation are being caused by some of the AF grains that are flipping 180° due to the energy dumped into the system from the laser pulse. These grains are exerting small torques on the FM layer through the exchange bias interaction, which is causing a perturbation in the FM layer inducing oscillations.

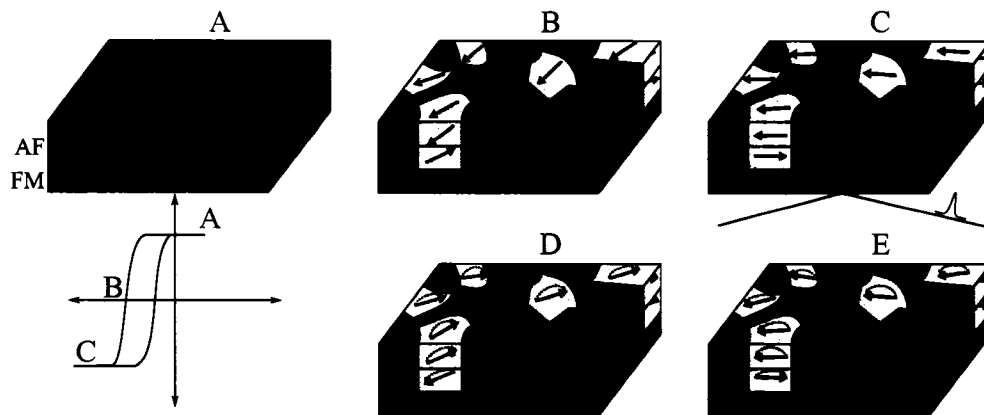


FIG. 8.4: Sketch of the AF grains during magnetization reversal at different points in the hysteresis loop. Shown are points at: (A) positive saturation, (B) the switching field and (C) negative saturation. When a laser pulse hits the surface in (C), the exchange bias is destroyed and the rotatable grains partially reverse to conform with its AF neighbors, shown in (D). As the interaction returns, shown in (E), the grains reverse back into a configuration similar to (C) and cause a torque on the magnetization allowing it to rotate.

A distribution of grains and grain types was used by Stiles and McMichael to explain the divergent behavior of the hysteresis loop shift, coercivity, and rotatable anisotropy in exchange-biased samples. They proposed that the loop shift is due to AF grains that are “frozen-in” (non-rotatable) and coercivity increases due to rotatable grains. The Stiles and McMichael model is depicted in Figure 8.4 (A)–(C) where the AF grain structure is shown for different applied fields in the hysteresis loop. Some grains rotate with the FM

as the magnetization is reversed. The rotatable grains are highlighted, and each follows the FM magnetization shown as a single domain particle on the bottom of each stack. When a laser pulse is incident on the configuration shown in Fig. 8.4 (C), a decoupling of the AF/FM interface occurs and the rotatable grains begin to rotate back since they are no longer held with the AF/FM exchange interaction, shown in Fig. 8.4 (D). As the exchange bias interaction recovers, these same grains will rotate back into a configuration shown in Fig. 8.4 (E), which will apply a torque on the magnetization allowing it to precess.

For either the Fulcomer and Charap or Stiles and McMichael picture the key is that some of the grains in the AF layer can be activated by the application of pump laser pulses. The activation of grains in the AF layer cause a disturbance in the FM layer which provides the “kick” required to launch oscillations.

8.3 Evidence for Pump-Induced Pinning

To test this model of pump-induced pinning we conducted two series of experiments. The first one tests how the static hysteresis loop changes as a function of pump power when both the pump and probe are directed onto the same spot on the sample. The second set of experiments show how the pump-beam can induce pinning and launch magnetic oscillations.

8.3.1 Static Laser Repinning

To understand the oscillations along the easy axis, we first checked how the pump beam affected the static hysteresis loop. A standard configuration for static MOKE was used. In this configuration, the lock-in amplifier referenced the 1 kHz repetition rate of the laser. This is different from what was done in Sec. 7.6 where the lock-in mechanism was on the optical chopper frequency that allowed for the detection of the pump-induced

change of the Kerr signal.

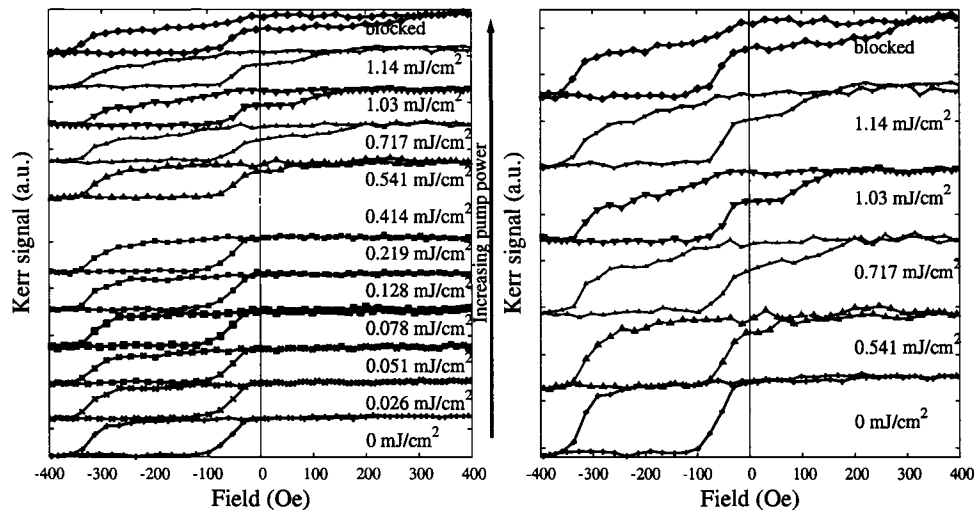


FIG. 8.5: Static MOKE curves taken as a function of the incident pump power for a IrMn/3 nm Co sample. The left panel shows all of the MOKE curves with the pump power increasing the further up the loop is shifted. The right panel is a close up of the 0 mJ/cm² and the larger powers, showing the emergence of a doubly shifted hysteresis loop. For the final loop, the pump was blocked after exposure and the MOKE scan was taken after 25 minutes, showing a double loop and a permanent repinning of a portion of the sample.

Figure 8.5 shows the shape of the static hysteresis loop as a function of pump power for a IrMn/3 nm Co sample. The reason that the 3 nm Co sample was used as opposed to a thicker Co sample is that the thin Co layer allows for the exchange bias shift to be large. The effects from the pump beam are easier to see with a large shift in the initial hysteresis loop. The left panel shows increasing pump power with the pump-blocked curve (0 mJ/cm²) at the bottom, and the right panel shows selected curves from the left panel close up. The selected curves are for larger powers showing the emergence of a second, positively shifted, hysteresis loop. As the power increases, the loop shift becomes more prominent. The double shift implies that regions of the sample within the width of the probe laser beam are being repinned in the opposite direction from the rest of the sample. As the power increases, more regions within the width of the probe beam are being oppositely pinned causing the second hysteresis loop.

8.3.2 Ultrafast Laser Repinning

In light of the experiments in Sec. 8.3.1 where it was possible to induce a permanent change in the exchange bias using the pump beam, a subsequent series of experiments were conducted to test if the exchange bias could be induced from an previously unpinned sample.

Two samples were tested, both made from the same buffer layers and IrMn as the AF as the samples in Chapter 7, but with two different Co thicknesses of 5 and 12 nm. Since the samples were grown in a pinned state each needed to be unpinned. Initially, we tried to heat the sample above the blocking temperature of 500 K to disorder the AF layer and cool it in a field-free environment. This was not successful because at the blocking temperature the FM layer is still ordered (from Table 2.1 the Curie temperature for Co is 1404 K) and at the AF/FM interface the AF layer experiences a magnetic moment from the FM layer that induces pinning. The solution, provided by Bill Egelhoff, was to heat it above the blocking temperature and cool the sample in a rotating magnetic field. The rotation of the magnetic field allows for the grains to cool in different orientations. Because the distribution of grain size in our samples and the different grain sizes cause different blocking temperatures, the sample cools such that the moments are randomly oriented and no shift occurs in the hysteresis loop. To rotate the magnetic field, we placed the sample at the end of a flathead screw that was placed into a drill. The sample was heated up to above the blocking temperature with a heat gun and cooled in a static magnetic field with the drill spinning the sample that provides the rotating magnetic field.

The procedure for testing for a pump-induced H_{EB} shift is straightforward. After the sample has been unpinned, static MOKE was taken on it using the ultrafast laser with the pump beam blocked. The probe beam power is small so it does not induce exchange biasing. After MOKE was taken, the field was turned off and the pump beam was overlapped on top of the probe. An external field is applied and a pump-probe scan

was taken. The reason pump-probe is done is to show that the pump and probe beams are overlapped well and that spin waves are being generated with the laser. The pump is then blocked and another hysteresis loop is taken.

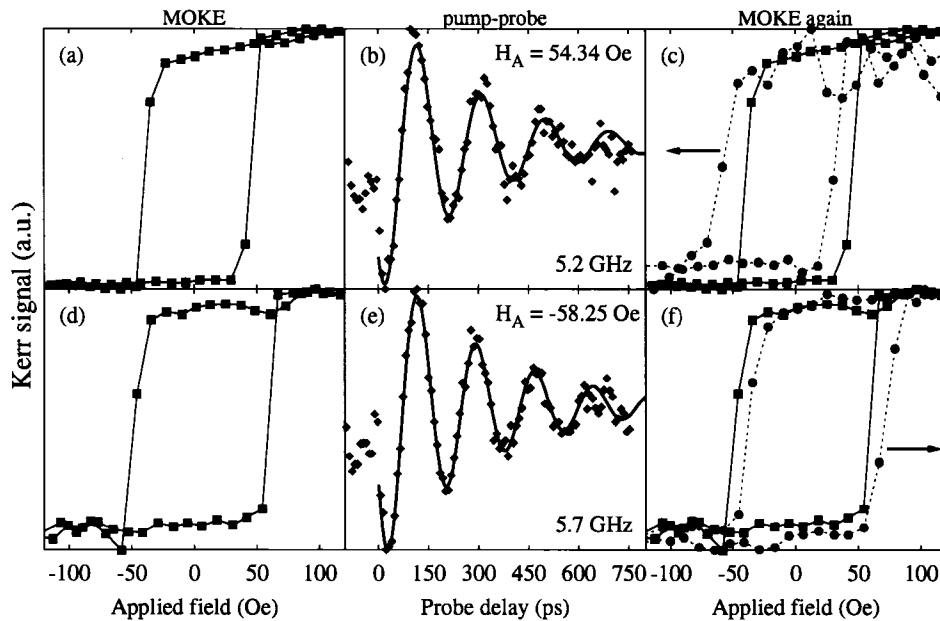


FIG. 8.6: MOKE, then pump-probe, then MOKE to show that the pump beam induces exchange biasing. The unpinned MOKE curves are shown in (a) and (d). Then pump-probe is induced by directing the pump and applying external fields of (b) 54.34 Oe and (e) -58.25 Oe. The fitted frequencies from Eq. (4.8) are also shown inset. The MOKE curves are taken again shown in (c) and (f) (along with the initial curves from (a) and (d) for reference) showing that the loop has shifted.

The results from this experiment along the easy axis are shown in Figure 8.6 for the IrMn/12 nm Co sample. The two rows represent two different attempts using positive (top) and negative (bottom) external fields during the pump-probe scan. The initial static MOKE scans (a) and (d) show the unpinned loop. The two loops are slightly different because the two scans were taken on different spots of the sample that are subject to local effects. After the static MOKE scans, pump-probe scans were taken in external fields of (b) 54.34 Oe and (e) -58.25 Oe. The frequencies for these oscillations are shown inset. The pump beam is blocked and another MOKE scan is taken, shown with the dotted lines in (c) and (f). In (c) and (f), the initial MOKE scans are also shown for comparison with

arrows to show the shift of the hysteresis loop from the initial curve.

From the subsequent MOKE curves in Fig. 8.6 (c) and (f), one can see the clear shift in the loop compared to the initial scan. The absolute values of the loop shifts observed are 13 Oe for the top and 17 Oe for the bottom, which is less than the as-grown exchange bias shift of 67 Oe. The direction of the shift is opposite to the direction of the applied field used during the pump-probe scans, which is similar to what is seen in exchange-biased structures. Traditionally, when pinning an exchange-biased structure using a heat gun or oven, the shift of the hysteresis loop is opposite to the direction of the applied field.

This result shows that an unpinned exchange-biased sample can be pinned using the pulsed laser and generate magnetic excitations at the same time. Calculations were made to check the maximum thermal heating assuming that all of the energy from the laser pulse is converted to lattice heat in a spot the size of the laser beam. They show that the temperature of the Co lattice increases by 141.9°C , which is not enough to reach the blocking temperature of 250°C for the AF layer. A more advanced model that includes two temperatures (electron and lattice) with reasonable numbers for the coupling between temperatures [14, 127] showed that the lattice temperature increase from the pump beam is 20°C . The electron temperature increase is 100°C , but this is smaller than the bulk blocking temperature for IrMn of 250°C [128]. The increases in electron and lattice temperatures with the two-temperature model increase linearly with the laser power, and a doubling of the laser power would not be enough to reach the blocking temperature.

The same experiment was conducted on the hard axis of the same exchange-biased sample. The results are shown in Figure 8.7. The initial MOKE curve is shown in (a), then an applied field of 59.42 Oe was used for pump probe, shown in (b). A subsequent static MOKE curve is taken (blue dots) and compared with the initial curve (red line) in (c). Then pump-probe was done again with a larger field of 111.8 Oe shown in (e). The result from this and a comparison of the MOKE curve after the first pump-probe scan is shown in (f). In (b) and (e), the frequency extracted for the 59.42 Oe applied field is larger than

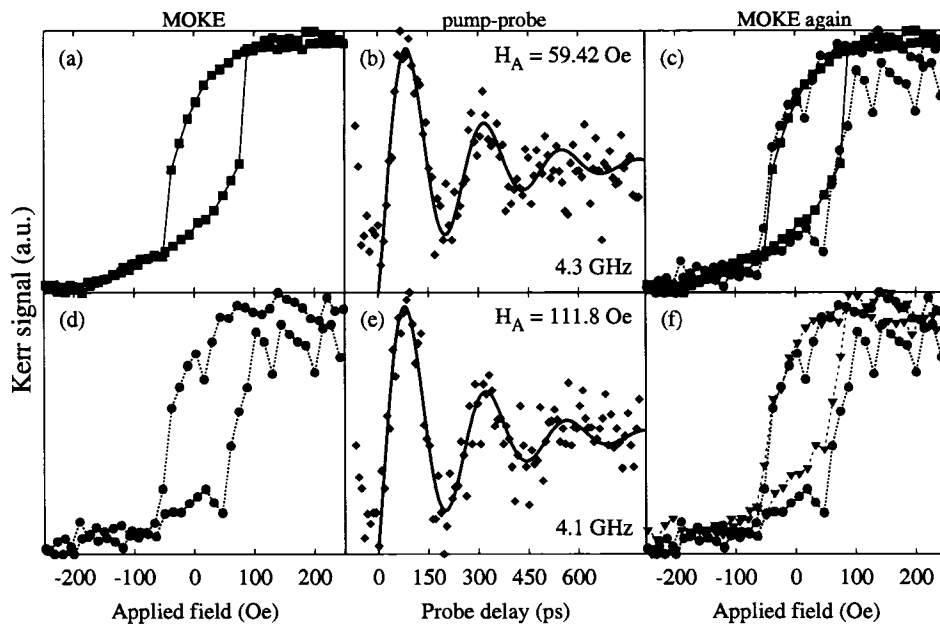


FIG. 8.7: MOKE, then pump-probe, then MOKE on a IrMn/12 nm Co sample along the hard axis. The unpinned MOKE curves are shown in (a) and (d). The pump-probe curves are taken in external fields of (b) 59.42 Oe and (d) 111.8 Oe in successive runs. The static MOKE curves are taken right after the pump-probe showing shifts to the left, opposite to the applied field direction.

the frequency extracted for the 111.8 Oe field. One may think that the frequency should increase monotonically with field so the scan at the larger field of 111.8 Oe in Fig. 8.7 should be larger than the frequency at 59.42 Oe, but along the hard axis there can be a cusp in the frequency-field profile where the frequency reaches a minimum at a non-zero applied field. This happens to some extent in Fig. 7.3 for the hard axis ($\phi_{EB} = 90$) and we have observed it in other systems measured.

The results from this experiment are inconclusive. The loop after the first pump-probe scan does not appear to be shifted much from the initial result. The second try at a larger field (bottom row) shows more of a shift compared with the static MOKE loop after the first hysteresis loop. The loop shifts are opposite to the applied field direction similar to the exchange bias interaction. The quality of the pump-probe curves is poor, based on the fits to the decaying oscillating exponential. This means that the spatial overlap between the pump and probe was not good, which is a factor in determining if the pump

will affect the same grains that the probe is measuring.

Because the exchange biasing was removed from the sample by spinning it in a field, it is curious that the easy axis shows easy axis characteristics and the hard axis shows hard axis characteristics. The removal of the exchange bias interaction should remove the hard and easy axes, and both samples should look similar to an unpinned Co sample. Comparing with the initial MOKE curves of Fig. 8.6 (a) and Fig. 8.7 (a), this is not true. The loop in the easy axis experiment is an easy axis, and the loop in the hard axis experiment is a mix of hard and easy axes. The sample is probably not reaching a large enough temperature to affect all of the grains in the system, just the small and medium sized grains. The largest grains (which will have a larger blocking temperature) may not be affected by the heat and remain in their initial state.

We also tried the same experiment on an IrMn/5 nm Co sample because the 5 nm sample would have shown a larger shift in the loop than a 12 nm Co sample due to its thinner Co layer. The pump probe curves for the 5 nm Co sample were not clean, meaning that the overlap between the pump and probe beams was not good. The before and after MOKE curves show a shift opposite to the direction of the applied field, indicating an exchange bias shift as seen in the 12 nm Co sample. Attempts to repin the hard axis for the 5 nm Co sample were not successful.

The model introduced in Sec. 8.2 may be used to describe the effects in Fig. 8.5 by noting that larger pump powers allow for more, larger AF grains to flip. These flipped AF grains will re-couple to the FM layer yielding a positively shifted hysteresis loop. Fig. 8.6 is explained in a similar fashion where the pump beam is inducing various AF grains to flip by providing an energy larger than Eq. (8.1), which then can recouple to the FM layer that is in a saturated or nearly saturated state. The loop shift is less than the as-grown samples because the amount of grains that are activated with the pump pulse is small compared with the amount of grains that can be activated using an oven or heat gun, meaning that the AF/FM coupling will not be as strong.

To determine the energy required to flip states, the model of Fulcomer and Charap [28] and Xi [126] state that the energy barrier for switching is

$$\Delta E_{\pm} = K_{AF}t_{AF} \left[1 + \left(\frac{J_{EB}}{2K_{AF}t_{AF}} \right)^2 \right] \pm J_{EB}, \quad (8.1)$$

where K_{AF} is the AF anisotropy, t_{AF} is the AF thickness, and J_{EB} is the interface exchange energy measured in Sec. 6.3.2. Using an $K_{AF} = 2 \times 10^6$ erg/cm³ from the literature [129] and an AF thickness of 10 nm, the energy to flip the grains is $E_- = 0.1943$ mJ/cm² and $E_+ = 0.1655$ mJ/cm². From Fig. 8.5 one can see that the onset of the second hysteresis loop is 0.541 mJ/cm², which is much larger than the energy barriers.

Considering that the laser beam has to travel through the whole Co layer before it reaches the AF layer, one can use Beer-Lambert law to calculate the energy at the AF/FM interface. Using reasonable values for the reflectivity ($R = 0.67$) and absorption coefficient $\alpha = 0.07$ nm⁻¹ of Co, the laser light at the AF/FM interface for a 3 nm thick Co sample is 40% of the initial intensity, giving a pulse energy of 0.220 mJ/cm² at the AF/FM interface for an initial pulse of 0.541 mJ/cm². Since the energy at the interface from the pump pulse is larger than the energy required to flip the grains, the energy provided by the pump is large enough to get over the energy barrier every pulse even when considering the effect of the energy loss of the pulse to the Co layer above it.

The K_{AF} value was calculated using a grain size of 12 nm, which is larger than previously reported grain sizes of 6–11 nm [63, 64, 65]. The grain size is a significant factor in the determination of K_{AF} , which is the leading term in Eq. (8.1) and the largest contributor to the energy barrier. Because of this and the lack of measurements of K_{AF} for smaller grain sizes, it is reasonable to suggest that this is a possible mechanism for excitation of oscillations and pinning in our experiments.

8.4 Comparison of Pump Powers to the Literature

This section compares our results with contemporary work in ultrafast magnetization dynamics. It is intended to show perspective of the pump power in this experiment with other scientific work in this field.

Authors	Material	Laser fluence (mJ/cm ²)	Ref.
Tsukamoto <i>et al.</i>	GdFeCo	50	[130]
Beaurepaire <i>et al.</i>	Ni	7	[14]
Hohlfeld <i>et al.</i>	Ni, Co	10–12	[131]
Hohlfeld <i>et al.</i>	GdFeCo	10–12	[132]
Ju <i>et al.</i>	NiO/Ni	0.14	[8, 9]
Weber <i>et al.</i>	FeMn/NiFe	0.00425	[133, 134]
Dalla Longa <i>et al.</i>	Mn/Co	1.0	[122]
Our work	IrMn/Co	0.61	

TABLE 8.1: Comparison of pump powers for various experiments in the literature. The pump probe power used in this dissertation is in the range of pump powers on other contemporary experiments. For the experiments on exchange-biased structures, the pump power used in this Dissertation is in the range of previously reported work.

It should be stressed that the powers used in these experiments to induce the permanent changes in the pinning are relatively low. Our pump beam was unfocused, with a radius of 1 mm, giving a maximum fluence of 0.61 mJ/cm² or, assuming Gaussian pulses, a peak power of 3.7 GW/cm². This is not much greater than the fluence used by Ju *et al.* [8, 9] (0.14 mJ/cm²) in their study of Ni/NiO, or by Weber [133] (0.5 GW/cm²) on NiFe/FeMn, and is an order of magnitude below the fluence levels used by Beaurepaire *et al.* [14] to induce changes in the magnetization of Ni (7 mJ/cm²) and Tsukamoto *et al.* [130] to produce thermographic writing in GdFeCo (50 mJ/cm²). A comparison of pump powers for other all-optical experiments is show in Table 8.1. The experiments reported by others in Table 8.1 on exchange-biased structures all used un-amplified laser oscillators, whereas the experiments presented in this chapter and thesis use an amplified laser system. The amplified system provides a larger peak power at the cost of a smaller repe-

tition rate. For un-amplified laser oscillators, the pump and probe beams must be focused onto the sample to provide enough fluence to induce oscillations. This is not necessary in our experiments due to the power in our amplified system.

Previous work by Ju *et al.* [8, 9] did not observe the same phenomenon of oscillations past saturation because their group used single crystal structures, and work by Weber *et al.* [13, 16] have grain sizes on the order of 4 nm, based on their layer thicknesses and work done by Nishioka *et al.* [60]. Although our grain structure was not measured explicitly, Ro *et al.* [63] have grown similar structures and observe a grain size of 6–11 nm. The smaller grain size of Weber along with the smaller pump power that they used (see Table 8.1) made it hard for him to see it, although his paper mentions that the power was kept low enough to avoid permanent changes in the interface, indicating that permanent changes were observed [16].

In summary, we have found that the pump beam can permanently affect the magnetization of the samples. Other experiments show that the pump-power affects the hysteresis loops and that the exchange biasing can be induced from a previously unpinned sample simply by applying a sufficiently strong pump pulse. The phenomenon of oscillations along the easy axis are explained using the theory of Fulcomer and Charap's energy barrier. This can be used to qualitatively explain the experiments seen in this Chapter.

CHAPTER 9

Conclusions and Outlook

9.1 Summary

We have investigated the exchange biasing and coercivity in two systems: IrMn/Co and FeMn/Co. In Chapter 6 we discovered that the exchange biasing in FeMn/Co is sensitive to the buffer layers grown beneath them. The Co thickness dependence of the exchange biasing shows that a leveling off of H_{EB} as the Co thickness is decreased for FeMn, but a continuous $1/t_{FM}$ increase with IrMn. By changing the buffer layer on FeMn from Ta/Cu to W/Cu, the H_{EB} increased continuously with $1/t_{FM}$ thickness. The angular dependence of the exchange biasing and coercivity on single-thickness FeMn/Co films with Nb buffer layers showed that it is well pinned through the FM layer.

To continue the studies of exchange biasing we conducted measurements on IrMn/Co using the ultrafast pump-probe technique. This generates oscillations of the magnetic moment about an applied field. The oscillations are single-frequency and are fit using a standard ferromagnetic resonance equation, which is a frequency-domain technique. The fits give reasonable values for the two free parameters in the equation: H_{EB} and H_C . The points measured using FMR are close to the points from the pump-probe measurements.

The Gilbert damping parameter extracted from the oscillations is enhanced compared with a pure Co film, as has been observed with similar exchange biased structures in the literature. The value for the parameter is on the order of what others have observed in the literature. The dynamic hysteresis loops of pump-probe experiment show that the response of the magnetization from the pump is fast (< 6 ps) and along the easy axis in intermediate times ($30 \text{ ps} < t < 100 \text{ ps}$) the loops show two peaks that roughly correspond to the switching field of the static hysteresis loop. Along the hard axis the dynamic hysteresis loops, when placed in their respective time delays on a 3D map, trace out a half oscillation that would be measured using the pump-probe technique. Modeling using the FMR equations and the equation used to fit the oscillations show similar behavior, although not exact.

The observed oscillations exhibit a peculiar property: they exist along the easy axis at large fields. Others have reported the disappearance of oscillations along the easy axis at large fields, but in these experiments they remain large and long lived. To explain this, we have introduced a qualitative theory that the oscillations are being launched by a permanent re-setting of the exchange bias interaction. The energy required to alter the interaction depends on the grain size with smaller grains being easier to flip. These small grains flip easier than large grains, which have a larger activation energy. We observe a doubly shifted static hysteresis loop that has a pump power dependence—more of the loop shifts as the pump power is increased. This is because the larger energy being dumped into the lattice allows for a larger percentage of grains to flip. We also show that we can permanently alter the magnetization using the pump-probe experiment. The pump can pin the sample and launch oscillations.

9.2 Future Work

Now that we have introduced a mechanism for the oscillations along the easy axis, it must be tested more thoroughly. Future work to test the theory must focus on either epitaxial IrMn/Co or on the buffer layers of IrMn/Co so that the grain size is altered without altering the other magnetic properties such as exchange biasing or coercivity. To publish the work, grain size studies will need to be conducted alongside the pump-probe measurements to correlate the two. Other epitaxial systems could be used, but the field of exchange biasing is complicated and it would be best to continue with the same material systems studied in this work.

Along with the grain size studies, it would also be useful to test the pump-induced pinning on other systems. The focus of this would be to test if this phenomenon is due to something special to the IrMn/Co system or if it is a more general effect of exchange-biased systems, small or large grained. We have started work on epitaxial systems FeN and FePt to investigate if the crystalline anisotropies can be modified by the pump pulse.

Since the MOKE measurement is a polarization-sensitive technique, it is crucial to measure the polarization well. The scheme in this work uses a polarizer-analyzer scheme which relies on the extinction ratio of the polarizer pair. A more advanced scheme uses a polarizing beam-splitter that splits the \hat{s} and \hat{p} components. These two components are then sent to individual photodiodes and subtracted from each other. To balance the two beams, a $\lambda/4$ wave plate is placed before the beam-splitter which is allowed to rotate and balance the \hat{s} and \hat{p} polarizations. This scheme has two benefits, 1) the fluctuations in laser intensity are canceled out and 2) a observed change in polarization is enhanced since it shows up in both the \hat{s} and \hat{p} components as a sum in one and a difference in the other.

APPENDIX A

Symbols

This appendix lists the reoccurring symbols used in this Dissertation. It is ordered alphabetically.

Symbol	Description
F	Internal free energy (Sec. 4.5, Sec. 4.5.1).
g	Spectroscopic splitting factor (Sec. 4.2).
H	Externally applied field (Sec. 4.2).
H_A	Externally applied field from an electromagnet (Sec. 4.5.1).
H_C	Coercive field (Sec. 2.3 and Fig. 2.5).
H_D	Demagnetization field (Sec. 2.1.1).
H_{EB}	Exchange bias field.
H_{eff}	Effective field (Sec. 4.3, Sec. 4.5).
J_e	Direct exchange integral (Sec. 2.1).
J_{EB}	Interface exchange energy (Sec. 6.3.2).
M	Magnetization vector (Sec. 4.2).
M_L	Longitudinal magnetization (Fig. 3.2).

m_l	M_L scaled by M_S (Sec. 3.2).
M_S	Saturation magnetization (Sec. 2.1.1).
M_T	Transverse magnetization (Fig. 3.2).
m_t	M_T scaled by M_S (Sec. 3.2).
\hat{p} or p	in the optical plane polarization (Fig. 3.2).
Q	Voigt magneto-optical parameter (Sec. 3.1).
\hat{s} or s	out of optical plane polarization (Fig. 3.2).
t_{FM}	Ferromagnet layer thickness.
α	Gilbert damping parameter (Sec. 4.3).
α_{crit}	Postulated critical angle from Stiles and McMichael models (Sec. 2.4.4).
γ	Gyromagnetic ratio (Sec. 4.2).
η	Phenomenological damping parameter (Sec. 4.3).
Θ	Curie Temperature (Sec. 2.1).
θ_i	Incoming polarizer angle relative to the optical plane (Sec. 3.2).
θ_r	Reflected polarizer angle relative to the optical plane (Sec. 3.2).
τ	Oscillation decay constant (Sec. 4.4).
ϕ_{EB}	Angle between H_A and H_{EB} (Sec. 4.5.1 and Fig. 4.5).

BIBLIOGRAPHY

- [1] T. Gerrits, H. A. M. van der Berg, J. Hohlfield, L. Bar, and T. Rasing, *Nature* **418**, 509 (2002).
- [2] J. Nogués and I. K. Schuller, *J. Magn. Magn. Mater.* **192**, 203 (1999).
- [3] J. Nogués, D. Lederman, T. J. Moran, and I. K. Schuller, *Phys. Rev. Lett.* **76**, 4624 (1996).
- [4] V. Skumryev, S. Stoyanov, Y. Zhang, G. Hadjipanayis, D. Givord, and J. Nogués, *Nature* **423**, 850 (2003).
- [5] P. Grünberg, R. Schreiber, Y. Pang, M. B. Brodsky, and H. Sowers, *Phys. Rev. Lett.* **57**, 2442 (1986).
- [6] M. N. Baibich, J. M. Broto, A. Fert, F. Nguyen Van Dau, F. Petroff, P. Eitenne, G. Creuzet, A. Friedrich, and J. Chazelas, *Phys. Rev. Lett.* **61**, 2472 (1988).
- [7] I. K. Schuller and G. Güntherodt (2002), URL <http://ischuller.ucsd.edu/EBManifesto.pdf>.
- [8] G. Ju, A. V. Nurmikko, R. F. C. Farrow, R. F. Marks, M. J. Carey, and B. A. Gurney, *Phys. Rev. Lett.* **82**, 3705 (1999).
- [9] G. Ju, L. Chen, A. V. Nurmikko, R. F. C. Farrow, R. F. Marks, M. J. Carey, and B. A. Gurney, *Phys. Rev. B* **62**, 1171 (2000).

- [10] M. van Kampen, C. Jozsa, J. T. Kohlhepp, P. LeClair, L. Lagae, W. J. M. de Jonge, and B. Koopmans, *Phys. Rev. Lett.* **88**, 227201 (2002).
- [11] B. Hillebrands and J. Fassbender, *Nature* **418**, 493 (2002).
- [12] J. Hohlfeld, E. Matthias, R. Knorren, and K. H. Benneman, *Phys. Rev. Lett.* **78**, 4861 (1997).
- [13] M. C. Weber, H. Nembach, and J. Fassbender, *J. Appl. Phys.* **95**, 6613 (2004).
- [14] E. Beaurepaire, J.-C. Merle, A. Daunois, and J.-Y. Bigot, *Phys. Rev. Lett.* **76**, 4250 (1996).
- [15] M. R. Freeman, M. J. Brady, and J. Smyth, *Appl. Phys. Lett.* **60**, 2555 (1992).
- [16] M. C. Weber, H. Nembach, S. Blomeier, B. Hillebrands, R. Kaltofen, J. Schumann, M. J. Carey, and J. Fassbender, *Eur. Phys. J. B* **45**, 243 (2005).
- [17] A. E. Berkowitz and K. Takano, *J. Magn. Magn. Mater.* **200**, 552 (1999).
- [18] R. L. Stamps, *J. Phys. D* **33**, R247 (2000).
- [19] W. Heisenberg, *Z. Physik* **49**, 619 (1928).
- [20] B. D. Cullity, *Introduction to Magnetic Materials* (Addison-Wesley, 1972).
- [21] S. Chikazumi, *Physics of Ferromagnetism* (Oxford, 1997).
- [22] J. A. Osborn, *Phys. Rev.* **67**, 351 (1945).
- [23] M. Viret, D. Vignoles, D. Cole, J. M. D. Coey, W. Allen, D. S. Daniel, and J. F. Gregg, *Phys. Rev. B* **53**, 8464 (1996).
- [24] R. Allenspach, M. Stampanoni, and A. Bischof, *Phys. Rev. Lett.* **65**, 3344 (1990).
- [25] A. H. Morrish, *The Physical Principles of Magnetism* (John Wiley & Sons, 1965).

- [26] A. P. Malozemoff, *Phys. Rev. B* **35**, 3679 (1987).
- [27] M. D. Stiles and R. D. McMichael, *Phys. Rev. B* **59**, 3722 (1999).
- [28] E. Fulcomer and S. H. Charap, *J. Appl. Phys.* **43**, 4190 (1972).
- [29] G. Choe and S. Gupta, *Appl. Phys. Lett.* **70**, 1766 (1997).
- [30] M. S. Lund, W. A. A. Macedo, K. Liu, J. Nogués, I. K. Schuller, and C. Leighton, *Phys. Rev. B* **66**, 054422 (2002).
- [31] N. C. Koon, *Phys. Rev. Lett.* **78**, 4865 (1997).
- [32] H. Xi and R. M. White, *Appl. Phys. Lett.* **87**, 410 (2000).
- [33] J. Nogués, D. Lederman, T. J. Moran, I. K. Schuller, and K. V. Rao, *Appl. Phys. Lett.* **68**, 3186 (1996).
- [34] S. Soeyaa, M. Fuyama, S. Tadokoro, and T. Imagawa, *J. Appl. Phys.* **79**, 1604 (1996).
- [35] D.-H. Han, J.-G. Zhu, and J. H. Judy, *J. Appl. Phys.* **81**, 4996 (1997).
- [36] D.-H. Han, J.-G. Zhu, J. H. Judy, and J. M. Sivertsen, *J. Appl. Phys.* **81**, 340 (1997).
- [37] C.-M. Park, K.-I. Min, and K. H. Shin, *J. Appl. Phys.* **79**, 6228 (1996).
- [38] M. D. Stiles and R. D. McMichael, *Phys. Rev. B* **60**, 12950 (1999).
- [39] J. van Lierop, K.-W. Lin, Z.-Y. Guo, and B. W. Southern, *J. Appl. Phys.* **99**, 08C101 (2006).
- [40] H. Xi and R. M. White, *J. Appl. Phys.* **94**, 5850 (2003).
- [41] A. Paetzold and K. Röhl, *J. Appl. Phys.* **91**, 7748 (2002).

- [42] M. Ali, C. H. Marrows, M. Al-Jawad, B. J. Hickey, A. Misra, U. Nowak, and K. D. Usadel, *Phys. Rev. B* **68**, 214420 (2003).
- [43] L. Wee, R. L. Stamps, and R. E. Camley, *J. Appl. Phys.* **89**, 6913 (2001).
- [44] M. Kiwi, *J. Magn. Magn. Mater.* **234**, 584 (2001).
- [45] W. H. Meiklejohn and C. P. Bean, *Phys. Rev.* **102**, 1413 (1956).
- [46] W. H. Meiklejohn and C. P. Bean, *Phys. Rev.* **105**, 904 (1957).
- [47] W. H. Meiklejohn, *J. Appl. Phys.* **33**, 1328 (1962).
- [48] J. S. Kouvel, *J. Phys. Chem. Sol.* **21**, 57 (1961).
- [49] J. S. Kouvel, *J. Phys. Chem. Sol.* **24**, 795 (1961).
- [50] K. A. Seu, H. Huang, J. F. Lesoine, H. D. Showman, W. F. Egelhoff, Jr., L. Gan, and A. C. Reilly, *J. Appl. Phys.* **93**, 6611 (2003).
- [51] T. C. Schulthess and W. H. Butler, *Phys. Rev. Lett.* **81**, 4516 (1998).
- [52] M. D. Stiles and R. D. McMichael, *Phys. Rev. B* **63**, 064405 (2001).
- [53] J. Geshev, L. G. Pereira, J. E. Schmidt, L. C. C. M. Nagamine, E. B. Saitovitch, and F. Pelegrini, *Phys. Rev. B* **67**, 132401 (2003).
- [54] M. Gruyters and D. Riegel, *Phys. Rev. B* **63**, 052401 (2000).
- [55] O. de Haas, R. Schäfer, L. Schultz, C. M. Schneider, Y. M. Chang, and M.-T. Lin, *Phys. Rev. B* **67**, 054405 (2003).
- [56] S. M. Zhou, K. Liu, and C. L. Chien, *Phys. Rev. B* **58**, R14717 (1998).
- [57] F. Y. Yang and C. L. Chien, *Phys. Rev. Lett.* **85**, 2597 (2000).

- [58] G. M. Stocks, W. A. Shelton, T. C. Schulthess, B. Újfalussy, W. H. Butler, and A. Canning, *J. Appl. Phys.* **91**, 7355 (2002).
- [59] W. J. Antel Jr., F. Perjeru, and G. R. Harp, *Phys. Rev. Lett.* **83**, 1439 (1999).
- [60] K. Nishioka, C. Hou, H. Fujiwara, and R. D. Metzger, *J. Appl. Phys.* **80**, 4528 (1996).
- [61] F. Offi, W. Kuch, L. I. Chelaru, K. Fukumoto, M. Kotsugi, and J. Kirschner, *Phys. Rev. B* **67**, 094419 (2003).
- [62] K. Selte, A. Kjekshus, A. F. Andresen, and W. B. Pearson, *Acta Chem. Scand.* **22**, 3039 (1968).
- [63] J.-C. Ro, Y.-S. Choi, and S.-J. S. H.-J. Lee, *IEEE Trans. Magn.* **35**, 3925 (1999).
- [64] H. N. Fuke, K. Saito, M. Yoshikawa, H. Iwasaki, and M. Sahashi, *Appl. Phys. Lett.* **75**, 3680 (1999).
- [65] J. van Driel, F. R. de Boer, K.-M. H. Lenssen, and R. Coehoorn, *J. Appl. Phys.* **88**, 975 (2000).
- [66] T. Stobiecki, J. Kanak, J. Wrona, M. Czapkiewicz, C. G. Kim, C. O. Kim, M. Tsunoda, and M. Takahashi, *phys. stat. sol. (a)* **201**, 1621 (2004).
- [67] M. Pakala, Y. Huai, G. Anderson, and L. Miloslavsky, *J. Appl. Phys.* **87**, 6653 (2000).
- [68] H. S. Jung, H. Fujiwara, and S. Matsunuma, *J. Magn. Magn. Mater.* **286**, 229 (2005).
- [69] H. S. Jung, O. Traistaru, and H. Fujiwara, *J. Appl. Phys.* **95**, 6849 (2004).

- [70] J. Wang, W. N. Wang, X. Chen, H. W. Zhao, J. G. Zhao, and W. S. Zhan, *Appl. Phys. Lett.* **77**, 2731 (2000).
- [71] J. Wang, W. N. Wang, X. Chen, H. W. Zhao, J. G. Zhao, and W. S. Zhan, *J. Appl. Phys.* **89**, 3897 (2001).
- [72] W. Kuch, F. Offi, L. I. Chelaru, M. Kotsugi, K. Fukumoto, and J. Kirschner, *Phys. Rev. B* **65**, 140408 (2002).
- [73] G. M. Luo, H. W. Jiang, C. X. Liu, Z. H. Mai, W. Y. Lai, J. Wang, and Y. F. Ding, *J. Appl. Phys.* **91**, 150 (2002).
- [74] H. Ohldag, A. Scholl, F. Nolting, S. Anders, F. U. Hillebrecht, and J. Stöhr, *Phys. Rev. Lett.* **86**, 2878 (2001).
- [75] B. H. Miller and E. D. Dahlberg, *Appl. Phys. Lett.* **69**, 3932 (1996).
- [76] M. Hehn, S. Padovani, K. Ounadjela, and J. P. Bucher, *Phys. Rev. B* **54**, 3428 (1996).
- [77] J.-W. Lee, J. Kim, S.-K. Kim, J.-R. Jeong, and S.-C. Shin, *Phys. Rev. B* **65**, 144437 (2002).
- [78] C. Mény, P. Panissod, and R. Loloee, *Phys. Rev. B* **45**, 12269 (1992).
- [79] J. Unguris, D. Tulchinsky, M. H. Kelley, J. A. Borchers, J. A. Dura, C. F. Majkrzak, S. Y. Hsu, R. Loloee, W. P. Pratt, Jr., and J. Bass, *J. Appl. Phys.* **87**, 6639 (2000).
- [80] T. P. A. Hase, B. D. Fulthorpe, S. B. Wilkins, B. K. Tanner, C. H. Marrows, and B. J. Hickey, *Appl. Phys. Lett.* **79**, 985 (2001).
- [81] H. Ohldag, A. Scholl, F. Nolting, E. Arenholz, S. Maat, A. T. Young, M. Carey, and J. Stöhr, *Phys. Rev. Lett.* **91**, 017203 (2003).

- [82] C.-G. Lee, J.-G. Jung, R. D. McMichael, R. A. Fry, A. Chen, W. F. Egelhoff Jr., and V. S. Gornakov, *J. Appl. Phys.* **91**, 8566 (2002).
- [83] M. Mansuripur, *The Physical Principles of Magneto-optical Recording* (Cambridge University Press, 1995).
- [84] J. M. Florczak and E. D. Dahlberg, *J. Appl. Phys.* **67**, 7520 (1990).
- [85] P. N. Argyres, *Phys. Rev.* **97**, 334 (1955).
- [86] H. S. Bennett and E. A. Stern, *Phys. Rev.* **137**, A448 (1965).
- [87] J. L. Erskine and E. A. Stern, *Phys. Rev. B* **12**, 5016 (1975).
- [88] P. S. Pershan, *J. Appl. Phys.* **38**, 1482 (1967).
- [89] R. Carey and B. W. J. Thomas, *J. Phys. D* **7**, 2362 (1974).
- [90] B. W. Roberts and C. P. Bean, *Phys. Rev.* **96**, 1494 (1954).
- [91] J. Jorzick, S. O. Demokritov, C. Mathieu, B. Hillebrands, B. Bartenlian, C. Chappert, F. Rousseaux, and A. N. Slavin, *Phys. Rev. B* **60**, 15194 (1999).
- [92] S. V. Vonsovskii, *Ferromagnetic resonance; the phenomenon of resonant absorption of a high-frequency magnetic field in ferromagnetic substances* (Oxford, 1966).
- [93] A. Aharoni, *Introduction to the Theory of Ferromagnetism* (Oxford, 1996).
- [94] W. F. Brown Jr., *Micromagnetics* (John Wiley & Sons, 1963).
- [95] L. Landau and E. Lifshitz, *Phys. Z. Sowjet.* **8**, 153 (1935).
- [96] T. L. Gilbert and J. M. Kelly, *Proc. 1st 3M Conf.* p. 253 (1955).
- [97] T. L. Gilbert, *Phys. Rev.* **100**, 1243 (1955).

- [98] D. O. Smith, *J. Appl. Phys.* **29**, 264 (1958).
- [99] T. J. Silva, C. S. Lee, T. M. Crawford, and C. T. Rogers, *J. Appl. Phys.* **85**, 7849 (1999).
- [100] J. E. Mahan, *Physical Vapor Deposition of Thin Films* (John Wiley and Sons, 2000).
- [101] *MESA Series Magnetic Measurement System*, Shb Instruments Inc. (2003).
- [102] *Model SR530 Lock-in amplifier Manual*, Stanford Research Systems (2005).
- [103] J. M. Khosroffian and B. A. Garetz, *Appl. Opt.* **22**, 3406 (1983).
- [104] M. Ali, C. H. Marrows, and B. J. Hickey, *Phys. Rev. B* **67**, 172405 (2003).
- [105] J. Keller, P. Miltényi, B. Beschoten, G. Güntherodt, U. Nowak, and K. D. Usadel, *Phys. Rev. B* **66**, 014431 (2002).
- [106] T. Hauet, J. A. Borchers, P. Mangin, Y. Henry, and S. Mangin, *Phys. Rev. Lett.* **96**, 067207 (2006).
- [107] S. Maat, K. Takano, S. S. P. Parkin, and E. E. Fullerton, *Phys. Rev. Lett.* **87**, 087202 (2001).
- [108] H. N. Fuke, K. Saito, Y. Kamiguchi, H. Iwasaki, and M. Sahashi, *J. Appl. Phys.* **81**, 4004 (1997).
- [109] V. I. Nikitenko, V. S. Gornakov, A. J. Shapiro, R. D. Shull, K. Liu, S. M. Zhou, and C. L. Chien, *Phys. Rev. Lett.* **84**, 765 (2000).
- [110] H. Xi and R. M. White, *Phys. Rev. B* **61**, 1318 (2000).
- [111] T. Williams, C. Kelley, R. Lang, D. Kotz, J. Campbell, G. Elber, and A. Woo, The gnuplot team (2006), URL <http://www.gnuplot.info>.

- [112] C. Hou, H. Fujiwara, and F. Ueda, *J. Magn. Magn. Mater.* **198**, 450 (1999).
- [113] J. Pelzl, R. Meckenstock, D. Spoddig, F. Schreiber, J. Pflaum, and Z. Frait, *J. Phys.: Condens. Matter* **15**, S451 (2003).
- [114] F. Schreiber, J. Pflaum, Z. Frait, T. Mühge, and J. Pelzl, *Solid State Commun.* **93**, 965 (1995).
- [115] J. A. Katine, F. J. Albert, R. A. Buhrman, E. B. Myers, and D. C. Ralph, *Phys. Rev. Lett.* **84**, 3149 (2000).
- [116] C. H. Back, R. Allenspach, W. Weber, S. S. P. Parkin, D. Weller, E. L. Garwin, and H. C. Siegmann, *Science* **285**, 864 (1999).
- [117] E. B. Myers, D. C. Ralph, J. A. Katine, R. N. Louie, and R. A. Buhrman, *Science* **285**, 867 (1999).
- [118] Y. Tserkovnyak, A. Brataas, and G. E. W. Bauer, *Phys. Rev. Lett.* **88**, 117601 (2002).
- [119] S. M. Rezende, A. Azevedo, M. A. Lucena, and F. M. de Aguiar, *Phys. Rev. B* **63**, 214418 (2001).
- [120] R. D. McMichael, M. D. Stiles, P. J. Chen, and W. F. Egelhoff, Jr., *J. Appl. Phys.* **83**, 7037 (1998).
- [121] B. Heinrich, J. F. Cochran, and R. Hasegawa, *J. Appl. Phys.* **57**, 3690 (1985).
- [122] F. Dalla Longa, J. T. Kohlhepp, W. J. M. de Jonge, and B. Koopmans, *J. Appl. Phys.* **99**, 08F304 (2006).
- [123] J. McCord, R. Schäfer, R. Mattheis, and K.-U. Barholz, *J. Appl. Phys.* **93**, 5491 (2003).

- [124] C. Leighton, M. R. Fitzsimmons, P. Yashar, A. Hoffmann, J. N. J. Dura, C. F. Majkrzak, and I. K. Schuller, *Phys. Rev. Lett.* **86**, 4394 (2001).
- [125] D. M. Engebretson, W. A. A. Macedo, I. K. Schuller, P. A. Crowell, and C. Leighton, *Phys. Rev. B* **71**, 184412 (2005).
- [126] H. Xi, *J. Magn. Magn. Mater.* **288**, 66 (2005).
- [127] J. Hohlfeld, S.-S. Wellershoff, J. Gdde, U. Conrad, V. Jhnke, and E. Matthias, *Chem. Phys.* **251**, 237 (2000).
- [128] A. J. Devasahayam and M. H. Kryder, *J. Appl. Phys.* **85**, 5519 (1999).
- [129] M. J. Carey, N. Smith, B. A. Gurney, J. R. Childress, and T. Lin, *J. Appl. Phys.* **89**, 6579 (2001).
- [130] A. Tsukamoto, K. Nakagawa, A. Itoh, A. Kimel, A. Tsvetkov, H. Awano, N. Ohta, A. Kirilyuk, and T. Rasing, *IEEE Trans. Magn.* **40**, 2543 (2004).
- [131] J. Hohlfeld, J. Gdde, U. Conrad, O. Dhr, G. Korn, and E. Matthias, *Appl. Phys. B* **68**, 505 (1999).
- [132] J. Hohlfeld, T. Gerrits, M. Bilderbeek, T. Rasing, H. Awano, and N. Ohta, *Phys. Rev. B* **65**, 012413 (2001).
- [133] M. C. Weber, H. Nembach, B. Hillebrands, and J. Fassbender, *J. Appl. Phys.* **97**, 10A701 (2005).
- [134] M. C. Weber, H. Nembach, B. Hillebrands, and J. Fassbender, *IEEE Trans. Magn.* **41**, 1089 (2005).

VITA

Keoki Adam Seu

Keoki Adam Seu was born on March 29, 1978, in Honolulu, Hawai'i. He grew up in Pūpūkea, on the north shore of O'ahu, Hawai'i. After graduating from Mililani High School in 1996, he enrolled at DePauw University in Greencastle, Indiana. He graduated from DePauw in 2000 with a BA, majoring in Chemistry and Physics with a minor in Mathematics. In the Fall of 2000 he enrolled in the graduate program in Physics at the College of William and Mary in Virginia. After receiving his MS in 2001, he joined the group of Dr. Anne Reilly to study exchange biasing and magnetization dynamics. This thesis was defended on September 25, 2006 at the College of William and Mary in Virginia.